INVESTIGATIONS OF NONLOCAL TRANSPORT AND CURRENT NOISE IN MESOSCOPIC NORMAL METAL-SUPERCONDUCTOR HYBRID STRUCTURES

BY

MARTIN P. STEHNO

DISSERTATION

Submitted in partial fulfillment of the requirements
for the degree of Doctor of Philosophy in Physics
in the Graduate College of the
University of Illinois at Urbana-Champaign, 2012

Urbana, Illinois

Doctoral Committee:

Associate Professor Nadya Mason, Chair
Professor Dale J. Van Harlingen, Director of Research
Professor George Gollin
Associate Professor Smitha Vishveshwara

Abstract

Spin-based solid-state quantum computing requires the creation of spatially separated, spin-entangled quantum states. The correlated electronic states in a conventional superconductor can serve as an abundant source of entangled spin-singlet electrons provided Cooper pairs can be split without losing wavefunction coherence. In Cooper pair-splitter devices the electrodes (or quantum dots) are coupled to a superconductor with a separation of less than or equal to the superconducting coherence length. At such distances coherent nonlocal subgap transport takes place. It involves Cooper pair splitting among other theoretically predicted transport processes. In this dissertation we investigate signatures of coherence in nonlocal transport. We focus on current correlation measurements in normal metal-superconductor-normal metal (NSN) devices with transparent interfaces for which higher-order processes such as correlated Andreev reflections at both interfaces are predicted to contribute. We verify the distance dependence of nonlocal transport in a superconducting wire to which several normal metal electrodes are attached and obtain a good agreement between the decay length of the nonlocal voltage signal and the theoretical value for the coherence length in the superconductor. To reveal the coherent nature of nonlocal transport we perform a series of experiments involving shot noise and nonlocal current correlation measurements in mesoscopic NSN devices. We extend the model of incoherent shot noise in diffusive normal metal-superconductor (NS) contacts and identify the magnitude of the local self-consistent gap in our devices. We find that the onset of nonequilibrium transport in the superconductor coincides with a steep increase in the nonlocal resistance. We determine the barrier strength at the NS interface by comparing the dynamic resistance to numerical calculations of the contact resistance based on the Keldysh-Usadel equations. The main finding of our work are symmetric, 'W-shaped' nonlocal subgap current correlations obtained by sweeping the bias voltage at one contact for fixed current bias at the other contact. This surprising behavior was predicted for NSN devices with similar values of interface transparencies and is caused by higher-order processes. The observation of higher-order processes proves the coherent nature of nonlocal subgap transport.

Meinen Eltern, Gerhard und Vera

Acknowledgments

I am greatly indebted to my adviser, Dale Van Harlingen, and thank him for his continuous support. He allowed me great freedom in developing my project and gave me lots of opportunities to learn and develop my skills. It is always a pleasure to discuss physics with him and learn from his straightforward and intuitive way to approach complex scientific problems. I also like to thank the chair of my defense committee, Professor Nadya Mason, for helpful discussions and encouraging words when they were most needed, and Professors George Gollin and Smitha Vishveshwara for accepting to partake in my final examination, and for offering suggestions and comments that helped me to improve my dissertation.

Much of my knowledge about sample fabrication and low temperature physics I owe to present and former members of the Van Harlingen research group: William Neils, Kevin Osborn, Trevis Crane, Sergey Frolov, Francoise Kidwingira, Madalina Colci-O'Hara, and Christopher Nugroho. My very special thanks go to Daniel Bahr for developing the electronics that I ultimately used in my experiment and for being such cheerful person and a good friend. Many ideas for my research came from stimulating conversations with Vladimir Orlyanchik and Ion Moraru. They were much appreciated.

The important part of my Urbana experience were the wonderful people I had the pleasure to meet here. I will never forget the long discussions about "life, love, and Nobel Prizes in Physics" on the back porch of the "dog pound" with my housemates Sergey and Olya, Tereza, and Stefanos. The long times away from home and family were eased by the friendships with some very special people, Alek and Angela, Arek and Giovanna, Gosia, Benjamin and Agnieszka, Ulises and Aga, and Dunja. Bethany, Sebastian, and Chandrasekaran gave me the final push to reach the finish line. Your unconditional support (at any hour of the day) gave me the strength to complete this dissertation. Finally, I like to thank my parents and siblings for always encouraging my scientific curiosity and supporting me in the best possible way.

I gratefully acknowledge funding support by the National Science Foundation grant DMR 06-05813 and by the Department of Physics.

Table of Contents

Chapter 1

Introduction

The most intriguing feature of quantum mechanics is the possibility of two (or more) spatially separated quantum objects to share an entangled quantum mechanical state. The probabilities which describe the behavior of the objects are intertwined and manipulations on one part of the system affect the other parts equally. Creation and control over entangled quantum objects open possibilities for novel forms of computation and secure exchange of information. New fields of science have emerged which aim at exploiting this basic quantum mechanical feature: quantum computation, quantum cryptography, and quantum information theory.

A conceptually straightforward way to create entangled electrons is to spatially separate the components of a spin-singlet electron pair which is preformed in nature. The electronic system of conventional superconductors undergoes a phase transition at low temperatures and forms bound states of two electrons with anti-parallel spin-alignment, known as a "Cooper pair". The wavefunction associated with the bound pair extends over a length scale of tens to hundreds of nanometers. Modern nanofabrication techniques allow to produce routinely devices of such dimensions. Therefore, it would appear feasible to create a quantum entanglement device based on a "Cooper-pair splitter."

Early experiments confirmed the presence of nonlocal subgap transport in superconductors and established the decay length of nonlocal voltage signals to be similar to the correlation length of the Cooper-pair wavefunction. Some aspects of wavefunction coherence were also studied. Coherent nonlocal transport is a necessary prerequisite for Cooper-pair splitting (CPS). However, CPS is not the only coherent nonlocal transport process; direct electron transmission (DET, or "Elastic Co-tunneling") and higher-order processes involving synchronized local Andreev reflection events at the contact points of the nonlocal transport device may also contribute. The relative strength of the individual contributions depend on geometry, interface barriers, and (non-equilibrium) quasiparticle distributions in the device. Further, a practical implementation of entanglement devices requires a means to control nonlocal transport. Recently progress toward a tunable Cooper-pair splitter device was reported in experiments performed by two groups [68, 69, 70] in different

architectures based on two quantum dots in contact with a mesoscopic superconductor.

Cooper-pair splitting introduces positive current correlations in the entanglement device but theoretical work suggests that positive correlations may also be observed in devices with highly transparent interfaces. The correlations originate from higher-order process which do not involve the creation of entangled electrons states in the device. Some evidence was found for CPS-like positive correlations in tunneling devices but higher-order correlation effects have not been observed experimentally. We studied normal metal-superconductor hybrid devices. As the relative contributions of CPS, DET, and higher-order effects vary with the quasiparticle distribution in the individual contacts of the device we can identify signatures of these processes in a measurement of the bias dependence of current noise correlations. Our results agree qualitatively with the theoretical predictions for devices with intermediate interface transparency.

The dissertation is organized as follows:

Chapter 2 introduces some basic theoretical concepts relevant to the experimental work in this study. It is split in two parts. The first part is an introduction to basic concepts of superconductivity and the relevant physics for coupling normal metal electrodes to superconductors. Andreev reflection, charge imbalance, and proximity effects in the normal metal-superconductor system are discussed. Further, the Keldysh-Usadel formalism is developed which will be used for resistance calculations later. The second part consists of a short introduction to shot noise in mesoscopic physics. The concepts of universal shot noise, shot noise suppression in mesoscopic devices, and shot noise doubling due to Andreev reflections are outlined. Shot noise in the presence of barriers at the NS interface will also be discussed.

Chapter 3 describes the phenomenology of nonlocal transport in normal metal-superconductor hybrid structures based on crossed Andreev reflection and elastic co-tunneling processes. Previous experimental work on nonlocal transport and current correlations is presented. The effect of higher-order coherent processes on nonlocal transport is discussed. The chapter closes with theoretical predictions for current correlations in normal metal-superconductor hybrid structures similar to our devices.

Chapter 4 starts with a discussion of design considerations for mesoscopic shot noise devices. The concept of reservoir heating is introduced and models for calculating the effective temperature in reservoirs are developed. The section concludes with a description of sample fabrication techniques. Next, the measurement concept is described. The SQUID resistance bridge circuit and a measurement setup for current cross-correlations with a two bridges are discussed. The chapter concludes with implementation details.

Chapter 5 is a presentation of our experimental results. We study the distance dependence of nonlocal transport in a long superconducting wire and reproduce the findings of earlier experiments. The main body of results concerns transport and current noise experiments on four selected devices. Numerical modeling is performed to assist in the interpretation of our data.

Chapter 6 comprises a brief summary of our findings and discusses ideas for future experiments.

Chapter 2

Theoretical concepts

2.1 Cooper pairs and BCS theory

In 1956 Leon Cooper showed that two electrons, which are introduced above a filled Fermi sea, can form a lower energy bound state in the presence of a weak attractive interaction [1] (the *Cooper instability* problem). The ground-state wavefunction of such a pair of electrons depends on the density of electronic pair states with net momentum K in the energy shell near the Fermi surface. Thus it has a strong maximum around $K = 0$ and Cooper concluded that in a condensate of electron pairs, elementary excitations were to be the splitting of a pair rather than an increase in kinetic energy.

BCS ground-state wavefunction

A full many-body description of the pairing process was worked out by John Bardeen, Leon Cooper, and J. Robert Schrieffer [2, 3]. Instead of writing down an exact ground-state wavefunction for all pairs of electrons, Bardeen, Cooper and Schriffer (BCS) argued that a mean-field approach, in which the occupancy of a state $\mathbf{k}$ only depends on the average occupancy of other states, will give a good approximation for a system consisting of a large number of particles. They proposed the ground-state wavefunction

$$|BCS\rangle = \prod_{\mathbf{k}} \left(u_{\mathbf{k}} + v_{\mathbf{k}} \hat{c}^{\dagger}_{\mathbf{k}\uparrow} \hat{c}^{\dagger}_{-\mathbf{k}\downarrow} \right) |0\rangle \ . \tag{2.1}$$

Equation 2.1 is expressed in occupation number representation and uses second quantization operators. For instance, the operator $\hat{c}^{\dagger}_{\mathbf{k}\uparrow}$ creates a spin-up electron state with wavevector $\mathbf{k}$. On the opposite, the operator $\hat{c}_{-\mathbf{k}\downarrow}$ removes a spin-down electron state with wave-vector $-\mathbf{k}$. The creation and annihilation operators describe fermions, hence they must fulfill the anticommutation relationships

$$\{\hat{c}^{\dagger}_{\mathbf{k}\sigma}, \hat{c}^{\dagger}_{\mathbf{k}'\sigma'}\} = 0 \ , \quad \{\hat{c}_{\mathbf{k}\sigma}, \hat{c}_{\mathbf{k}'\sigma'}\} = 0 \ , \quad \{\hat{c}^{\dagger}_{\mathbf{k}\sigma}, \hat{c}_{\mathbf{k}'\sigma'}\} = \delta_{\mathbf{k},\mathbf{k}'} \delta_{\sigma,\sigma'} \ . \tag{2.2}$$

The amplitudes $u_{\mathbf{k}}$ and $v_{\mathbf{k}}$ are known as *coherence factors* and describe the occupation of a pair state: The pair state with momentum index $\mathbf{k}$ is occupied with probability $v_{\mathbf{k}}^2$ and unoccupied with probability $u_{\mathbf{k}}^2$. The normalization condition $u_{\mathbf{k}}^2 + v_{\mathbf{k}}^2 = 1$ applies, which ensures that the BCS wavefunction is also normalized.

A consequence of the mean-field ansatz is that the many-body wavefunction does not describe a state with fixed number of electrons. $\hat{N}$ is not a good quantum number. However, in large systems the expectation value

$$\langle \hat{N} \rangle = \sum_{\mathbf{k}} 2v_{\mathbf{k}}^2 \tag{2.3}$$

is strongly peaked at the number of electrons N in the system, however broad enough to allow for a definite phase for the pairs. In this case it is appropriate to define a singlet pair function for the BCS state

$$\Psi(\mathbf{r_2}, \mathbf{r_1}) = \langle BCS | \hat{\psi}_\downarrow(\mathbf{r_2}) \hat{\psi}_\uparrow(\mathbf{r_1}) | BCS \rangle = \sum_{\mathbf{k}} \frac{u_{\mathbf{k}} v_{\mathbf{k}} \exp(i\mathbf{k} \cdot (\mathbf{r_1} - \mathbf{r_2}))}{\sqrt{V}} \ . \tag{2.4}$$

It corresponds to a spherically symmetric s-wave bounds state of higher order. Before we discuss the form of the pair function further, we need to determine the coherence factors in eqn. 2.4. They are found by minimizing the energy of the BCS pairing Hamiltonian

$$\mathcal{H}_{BCS} = \sum_{\mathbf{k}\sigma} \epsilon_{\mathbf{k}} n_{\mathbf{k}\sigma} + \sum_{\mathbf{kl}} \mathbf{V_{kl}} \hat{c}^\dagger_{\mathbf{k}\uparrow} \hat{c}^\dagger_{-\mathbf{k}\downarrow} \hat{c}_{\mathbf{l}\downarrow} \hat{c}_{-\mathbf{l}\uparrow} \ .$$

It is convenient to define $\xi_{\mathbf{k}} \equiv \epsilon_{\mathbf{k}} - \epsilon_F$, i.e. we measure the kinetic energy from the Fermi level, and $\Delta_{\mathbf{k}} \equiv -\sum_{\mathbf{l}} V_{\mathbf{kl}} u_{\mathbf{l}} v_{\mathbf{l}}$. Rewriting the Hamiltonian in terms of the coherence factors, we have

$$\langle BCS | \mathcal{H}_{BCS} - \mu \hat{N} | BCS \rangle = 2 \sum_{\mathbf{k}} (\xi_{\mathbf{k}} v_{\mathbf{k}}^2 - \Delta_{\mathbf{k}} u_{\mathbf{k}} v_{\mathbf{k}}) \ , \tag{2.5}$$

which can be minimized by taking the derivative with respect to $v_{\mathbf{k}}$ and using the normalization condition $u_{\mathbf{k}}^2 + v_{\mathbf{k}}^2 = 1$. We obtain the BCS coherence factors

$$v_{\mathbf{k}}^2 = \frac{1}{2}\left(1 - \frac{\xi_{\mathbf{k}}}{(\xi_{\mathbf{k}}^2 + \Delta_{\mathbf{k}}^2)^{1/2}}\right), \quad u_{\mathbf{k}}^2 = \frac{1}{2}\left(1 + \frac{\xi_{\mathbf{k}}}{(\xi_{\mathbf{k}}^2 + \Delta_{\mathbf{k}}^2)^{1/2}}\right), \quad \text{and} \quad 2u_{\mathbf{k}} v_{\mathbf{k}} = \frac{\Delta_{\mathbf{k}}}{(\xi_{\mathbf{k}}^2 + \Delta_{\mathbf{k}}^2)^{1/2}} \ . \tag{2.6}$$

The occupation probability for pair states $v_{\mathbf{k}}^2$ is graphed in Fig. 2.1. Below the gap energy $\xi_{\mathbf{k}} < -\Delta$ pair states are almost entirely occupied, whereas above the gap $\xi_{\mathbf{k}} > \Delta$ only a few pair states are filled.

The product of coherence factors in the expression for the pair wavefunction (eqn. 2.4) has significant contributions only in a small shell of width $\delta k \approx \frac{\Delta}{\hbar v_F}$ around the Fermi surface, where v_F is the Fermi velocity

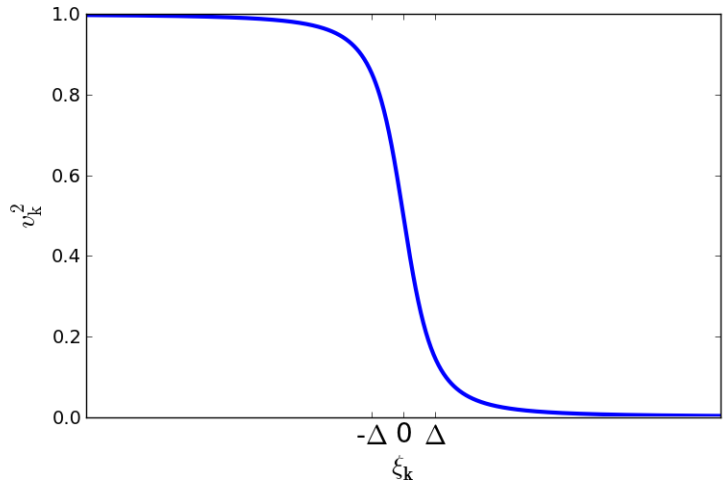

Figure 2.1: The occupation probability $v_{\mathbf{k}}^2$ for the BCS ground state.

of the electrons. The radius of the pair function state is approximately $1/\delta k = \frac{\hbar v_F}{\Delta}$, which approximates well the BCS *coherence length* in the disorder free metal ("clean-limit"),

$$\xi_0 = \frac{\hbar v_F}{\pi \Delta} \ . \tag{2.7}$$

Typical values for the BCS coherence length in pure metals can be as long as several microns [4]. In disordered materials the mean free path of the electrons ℓ is much shorter than ξ_0. In this case (the "dirty limit") the coherence length can be derived from microscopic calculations and is given by

$$\xi = \left(\frac{\hbar D}{\Delta}\right)^{1/2} \approx (\ell \xi_0)^{1/2} \ . \tag{2.8}$$

It can be several orders of magnitude shorter than the coherence length in pure materials. As will be shown in Chapter 5 we find excellent agreement between the theoretical value for the coherence (equ. 2.1) and the decay length of nonlocal voltage signals probed with normal metal contacts along a superconducting aluminum wire (see also Beckmann et al. [6] and Cadden-Zimansky et al. [5]) which is the starting point of our study.

Excitation spectrum

A quasiparticle excitation with momentum $\mathbf{k} \uparrow$ can be created by adding a single electron with $\mathbf{k} \uparrow$ or removing an electron with $-\mathbf{k} \downarrow$ from the ground state. To find the correct form for the quasiparticle

operators $\hat{\gamma}^\dagger_{\mathbf{k}\uparrow}$ and $\hat{\gamma}_{-\mathbf{k}\downarrow}$, we take a look at the action of the different creation and annihilation operators,

$$\hat{c}_{-\mathbf{k}\downarrow}|BCS\rangle = -v_{\mathbf{k}}|\mathbf{k}\uparrow\rangle|BCS;\mathbf{k}' \neq \mathbf{k}\rangle, \qquad \hat{c}^\dagger_{\mathbf{k}\uparrow}|BCS\rangle = u_{\mathbf{k}}|\mathbf{k}\uparrow\rangle|BCS;\mathbf{k}' \neq \mathbf{k}\rangle, \text{ and}$$
$$\hat{c}_{\mathbf{k}\uparrow}|BCS\rangle = v_{\mathbf{k}}|-\mathbf{k}\downarrow\rangle|BCS;\mathbf{k}' \neq \mathbf{k}\rangle, \qquad \hat{c}^\dagger_{-\mathbf{k}\downarrow}|BCS\rangle = u_{\mathbf{k}}|-\mathbf{k}\downarrow\rangle|BCS;\mathbf{k}' \neq \mathbf{k}\rangle.$$

The quasiparticle annihilation operators must obey

$$\hat{\gamma}_{\mathbf{k}\uparrow}|BCS\rangle = 0, \text{ and } \hat{\gamma}_{-\mathbf{k}\downarrow}|BCS\rangle = 0,$$

as no quasiparticle states exist in the ground state. Further the linear combinations of $\hat{c}$ operators that describe quasiparticle states must also obey Fermi anticommutation rules from eqn. 2.2. With this in mind we can write down the correct form of the new operators,

$$\hat{\gamma}^\dagger_{\mathbf{k}\uparrow} \equiv u_{\mathbf{k}}\hat{c}^\dagger_{\mathbf{k}\uparrow} - v_{\mathbf{k}}\hat{c}_{-\mathbf{k}\downarrow}, \text{ and} \tag{2.9}$$
$$\hat{\gamma}_{-\mathbf{k}\downarrow} \equiv u_{\mathbf{k}}\hat{c}_{-\mathbf{k}\downarrow} + v_{\mathbf{k}}\hat{c}^\dagger_{\mathbf{k}\uparrow}. \tag{2.10}$$

The operators describe elementary quasiparticle excitations of the condensate wavefunction. They are part of a set of transformations that diagonalize the pairing Hamiltonian as shown by Bogoliubov and Valatin [7]. Therefore, quasiparticle excitations are also called *Bogoliubons*. Creating a quasiparticle state with wavevector $\mathbf{k}$ changes the expectation value of occupation number by $1 - 2v^2_{\mathbf{k}}$. The total energy changes by

$$E_{\mathbf{k}} = (1 - 2v^2_{\mathbf{k}})\xi_{\mathbf{k}} + 2u_{\mathbf{k}}v_{\mathbf{k}}\Delta = (\xi^2_{\mathbf{k}} + \Delta^2)^{1/2}. \tag{2.11}$$

We assume here that for a small number of excitations we can take $\Delta_{\mathbf{k}} = \Delta$ constant. The minimum energy Δ which is required to produce a quasiparticle excitation is referred to as *superconducting gap energy.*

Gap equation and critical temperature

Thermally excited quasiparticle states are Fermi-distributed. In the non-interacting mean field approach products of quasiparticle operators acquire expectation values

$$\langle\hat{\gamma}^\dagger_{\mathbf{k}\sigma}\hat{\gamma}_{\mathbf{k}\sigma}\rangle = f_{\mathbf{k}\sigma}, \text{ and } \langle\hat{\gamma}_{\mathbf{k}\sigma}\hat{\gamma}^\dagger_{\mathbf{k}\sigma}\rangle = 1 - f_{\mathbf{k}\sigma}, \tag{2.12}$$

where $f_{\mathbf{k}\sigma} = \left(\exp(\frac{\epsilon_{\mathbf{k}}}{k_{\mathrm{B}}T}) - 1\right)^{-1}$ is the usual Fermi occupation factor. When recasting the pairing Hamiltonian into quasiparticle operators and replacing products of operators with their thermal expectation value

(terms with unequal numbers of quasiparticle operators do not acquire an expectation value and can be disregarded), the gap equation becomes

$$\Delta_{\mathbf{k}} = -\sum_{\mathbf{p}} V_{\mathbf{kp}} u_{\mathbf{k}} v_{\mathbf{p}} (1 - 2f_{\mathbf{p}}) = -\sum_{\mathbf{p}} \frac{\Delta_{\mathbf{p}}}{2E_{\mathbf{k}}} \tanh\left(\frac{E_{\mathbf{p}}}{2k_{\mathrm{B}}T}\right).$$

In the BCS approximation $\Delta_{\mathbf{k}} = \Delta_{\mathbf{p}} = \Delta$ and $V_{\mathbf{kp}} = -V$ for $|\xi_{\mathbf{k}}|,\ |\xi_{\mathbf{p}}| \leq \hbar\omega_D$, and zero otherwise. The frequency cutoff ω_D is defined by the Debye frequency of phonons which are mediating the interaction. For a large number of $\mathbf{k}$ states we can rewrite the sum as an integral with $N(0)$ the density of states at the Fermi surface

$$\frac{1}{N(0)V} = \int_0^{\hbar\omega_D} \frac{\tanh\left[\frac{1}{2k_{\mathrm{B}}T}(\xi^2 + \Delta(T)^2)^{1/2}\right]}{(\xi^2 + \Delta(T)^2)^{1/2}} \mathrm{d}\xi. \tag{2.13}$$

This equation can be solved numerically for the superconducting gap as a function of temperature, $\Delta(T)$. The critical temperature T_c is calculated by setting $\Delta = 0$ in equation 2.13 and performing the integral. We find

$$k_{\mathrm{B}}T_c = 1.13\hbar\omega_D \exp\left(-\frac{1}{N(0)V}\right),$$

which yields the famous BCS relation $2\Delta(0) \approx 3.5 k_{\mathrm{B}}T_c$.

2.1.1 Quasiparticles out of equilibrium

In thermal equilibrium quasiparticle states are occupied with a probability given by the Fermi distribution $f_0(E_{\mathbf{k}}, T) = \left[\exp(\frac{E_{\mathbf{k}}}{k_{\mathrm{B}}T}) - 1\right]^{-1}$. This is no longer the case in the nonequilibrium scenarios which we will discuss below. First, let us look at a single quasiparticle excitation. The nature of such an excitation changes form *electron-like* with an effective charge $q_k = 1 - 2v_{\mathbf{k}}^2 = \frac{\xi_{\mathbf{k}}}{E_{\mathbf{k}}} \approx 1$ for a wavevectors $\mathbf{k}$ outside of the Fermi surface to *hole-like* with $q_k = \frac{\xi_{\mathbf{k}}}{E_{\mathbf{k}}} \approx -1$ for wavevectors $\mathbf{k}$ inside the Fermi surface. The fractional charge originates from the linear combinations of electron and hole operators that form the excited states. The assignment of an electron or hole character therefore only makes sense far away from the Fermi energy, i.e. for $|\xi_{\mathbf{k}}| \gtrsim 2\Delta$. It should be noted, that the energy gap depends on the quasiparticle distribution and, in general, must be determined through the BCS gap equation

$$\frac{2}{V} = \sum_{\mathbf{k}} \frac{1 - 2f_{\mathbf{k}}}{(\xi_{\mathbf{k}}^2 + \Delta^2)^{1/2}}.$$

Even and odd excitation modes

Deviations from the equilibrium distribution of quasiparticle occupations, $\delta f_{\mathbf{k}} \equiv f_{\mathbf{k}} - f_0(E_{\mathbf{k}}, T)$, can be characterized by their symmetry with respect to inversion at the local Fermi surface (see Fig. 2.2). An *even* mode (which is also called 'longitudial', 'temperature', or 'energy' mode in the literature) is symmetric with respect to the Fermi surface. It result from a charge-neutral perturbation, such as a phonon or photon. An *odd* mode (or 'transverse', 'charged', or 'branch imbalance' mode) is created by a charged perturbation, e.g. the injection of current or the conversion of normal current to supercurrent at near an interface. The term 'branch imbalance' results from the occupation difference in the electron $n(E_{\mathbf{k}})$ and hole branch $p(E_{\mathbf{k}})$ of the dispersion relation. This causes a charge imbalance

$$Q^* \equiv \sum_{\mathbf{k}} q_{\mathbf{k}} \delta f_{\mathbf{k}} = \sum_{\mathbf{k}} \frac{\xi_{\mathbf{k}}}{E_{\mathbf{k}}} \delta f_{\mathbf{k}}. \tag{2.14}$$

The difference function in occupation numbers is given by $\delta f_{\mathbf{k}} = n(E_{\mathbf{k}}) - p(E_{\mathbf{k}})$. The number of electrons in the condensed ground state must also change to maintain charge neutrality. This results in opposite shifts of the quasiparticle (or "normal") chemical potential, μ_n, and the pair chemical potential, μ_p (cp. Fig. 2.2). The amount of effective quasiparticle charge is determined by the characteristic time scale τ_{Q^*} for re-equilibriation and the rate of injection, $Q^* = \dot{Q}^*_{\mathrm{inj}} \tau_{Q^*}$. The non-equilibrium population will diffuse away from the injection point and relax to equilibrium. In one dimensional geometry, Q^* will decay as $\exp(-x/\Lambda_{Q^*})$ with the diffusion length given by

$$\Lambda_{Q^*} = (D\tau_{Q*})^{-1/2} = \left(\frac{1}{3} v_F \ell \tau_{Q^*}\right)^{-1/2}. \tag{2.15}$$

The difference in quasiparticle chemical potential μ_n can be measured with respect to the chemical potential of the pairs μ_p. Experiments were pioneered by Clarke [8] who measured charge imbalance in superconducting tin films. Theoretically the quasiparticle relaxation process was described by Schmid and Schön [15] and Pethick and Smith [16]. Length, temperature and current dependence of charge imbalance relaxation were studied by several authors [9, 10, 11, 12, 13, 14]. Most recently, the distance and magnetic field dependence of charge imbalance at ultra-low temperatures was studied by Kleine et al. [20]. Typical charge relaxation times, τ_{Q*}, found in experiments are of the order of few nanoseconds with corresponding charge imbalance lengths, Λ_{Q^*}, of a few microns.

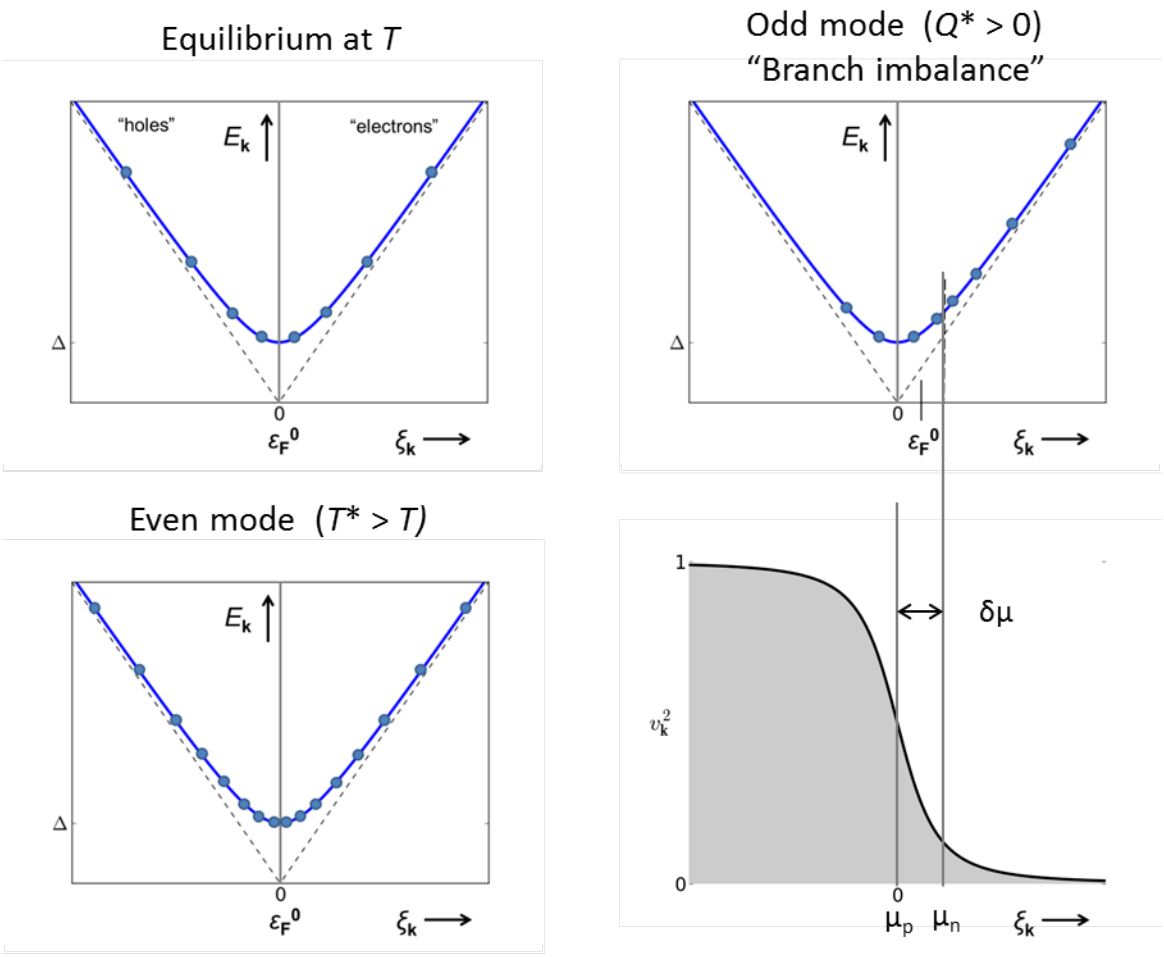

Figure 2.2: Even and odd quasiparticle excitations. For an odd mode the chemical potentials μ_p and μ_n shift relative to the equilibrium value ϵ_F^0.

2.1.2 Subgap transport at the NS interface

Bogoliubov - de Gennes equations

Non-equilibrium superconductivity on a small length scale can be described by a self-consistent real space method developed by Bogoliubov and de Gennes [17, 18]. It treats the interaction between two electrons as contact interaction, $U_{int}(\mathbf{r}, t; \mathbf{r}', t') = U(\mathbf{r})\delta(\mathbf{r} - \mathbf{r}')\delta(t - t')$, in analogy with BCS theory. The potential $U(\mathbf{r})$ should be interpreted as the average effective potential over a distance scale, $\lambda_c = \frac{v_F}{\omega_D} \approx \frac{\epsilon_F}{\hbar\omega_D}\frac{\lambda_f}{4\pi}$. This is the effective distance over which electron-phonon interactions are felt by the electrons. In the presence of spatial variations of the pairing interaction $U(\mathbf{r})$ and the pair potential $\Delta(\mathbf{r})$, a description in terms of momentum eigenvalues $\mathbf{k}$ is no longer appropriate. Instead, we need to construct position-dependent wavefunctions for the problem. The correct form is found from a generalization of the Bogoliubov transformation by

introducing position-dependent functions for the coherence factors

$$\psi(\mathbf{r}\uparrow) = \sum_n \left[\gamma_{n\uparrow} u_n(\mathbf{r}) - \gamma^\dagger_{n\downarrow} v^*_n(\mathbf{r})\right], \tag{2.16}$$

$$\psi(\mathbf{r}\downarrow) = \sum_n \left[\gamma_{n\downarrow} u_n(\mathbf{r}) + \gamma^\dagger_{n\uparrow} v^*_n(\mathbf{r})\right]. \tag{2.17}$$

The eigenfunctions u_n, and v_n must be calculated self-consistently to diagonalize the mean-field Hamiltonian

$$\mathcal{H}_{\text{eff}} = \int \mathrm{d}\mathbf{r} \left\{ \sum_\sigma \psi^\dagger(\mathbf{r}\sigma) H_0 \psi(\mathbf{r}\sigma) + \Delta(\mathbf{r})\psi^\dagger(\mathbf{r}\uparrow)\psi^\dagger(\mathbf{r}\downarrow) + \Delta^*(\mathbf{r})\psi(\mathbf{r}\uparrow)\psi(\mathbf{r}\downarrow) \right\},$$

where $H_0 = \left[\frac{1}{2m}\left(\frac{\hbar}{i}\nabla - \frac{e\mathbf{A}}{c}\right)^2 - U_0(\mathbf{r}) - \mu\right]$ is the one electron Hamiltonian and the pair potential is defined as

$$\Delta(\mathbf{r}) = U\langle\psi(\mathbf{r}\uparrow)\psi(\mathbf{r}\downarrow)\rangle = U\sum_n v^*_n(\mathbf{r})u_n(\mathbf{r})(1-2f_n). \tag{2.18}$$

The amplitudes $u_n(\mathbf{r})$ and $-v_n(\mathbf{r})$ are the electron and hole components of a quasiparticle wavefunction. In the absence of the pairing interaction, $\Delta(\mathbf{r}) = 0$, the components decouple and the Schrödinger equations read

$$H_0 u = Eu, \quad \text{and} \quad H_0^* v = -Ev,$$

thus $u(\mathbf{r})$ and $v(\mathbf{r})$ become ordinary electron and hole eigenfunctions in the normal state.

Andreev reflection

An important application of the Bogoliubov-de Gennes equations is in modeling the charge transport across a normal metal-superconductor interface. When current is passed from a normal metal into a superconductor a fraction is converted into supercurrent in the interface region. The residual charge enters the superconductor as nonequilibrium charge Q^* and relaxes over a much longer distance scale Λ_{Q^*}.

From our previous discussion one might come to the conclusion that an electron or hole excitation with energy $|E| < \Delta$ in the normal metal cannot enter the superconductor as there are no quasiparticle states of this energy available. Therefore, the normal metal-superconductor interface should be insulating at subgap energies even in the absence of a barrier. This is quite misleading. Current can be transmitted across the interface by the *Andreev reflection* process [19] which involves the formation of a Cooper pair in the superconductor.

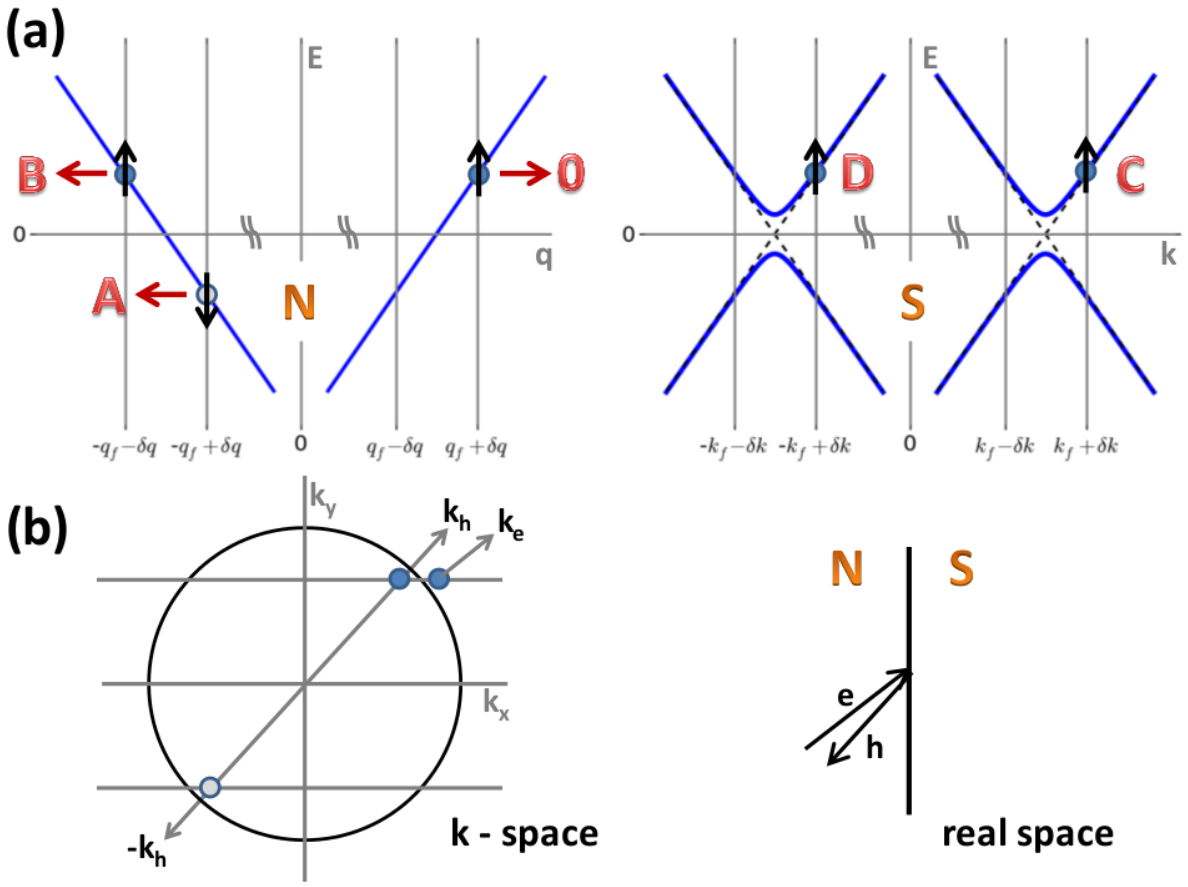

Figure 2.3: BTK model and Andreev reflection: **(a)** An electron (0) incident on an interface with a superconductor undergoes one of four processes that conserve energy: Andreev reflection occurs and a hole excitation with reversed group velocity is traveling back into the normal metal (A). The electron is reflected back by regular reflection (B). The electron creates an electron-like (C) or a hole-like quasiparticle excitation (D, 'branch-crossing'). **(b**, left) Electron- and hole-like excitations in k-space: The open circle at $-\mathbf{k_h}$ corresponds to the missing electron (or hole state) at $\mathbf{k_h}$. **(b**, right) In Andreev reflection the group velocity for the retro-reflected hole is almost exactly reversed.

We can obtain an understanding about the process of Andreev reflection by looking at an interface between a normal metal and the intermediate state of a type-I superconductor. In the interface region between normal metal and superconductor the electron and hole components of the quasiparticle wavefunction vary smoothly assuming the interface is sufficiently transparent. Far away from the interface on the normal metal side the wavefunctions resemble those of an electron or a hole excitation. Deep in the superconducting region they are in a superposition characteristic of the superconducting state. Two important observations are to be made. Firstly, despite the absence of a pairing interaction, the condensate wavefunction has a finite expectation value $\langle\psi(\mathbf{r}\uparrow)\psi(\mathbf{r}\downarrow)\rangle$ in the normal metal region adjacent to the interface. By this *proximity effect* the normal metal region acquires some of the properties of a superconductor, which we will discuss in the next section.

Secondly, the self-consistent gap $\Delta(\mathbf{r})$ gradually opens up as we move away from the interface toward the inner region of the superconductor, typically over length scales comparable to the coherence length of the superconductor. Therefore, a quasiparticle encounters a rising dispersion curve $E(k)$ as it travels in the direction of increasing gap. Consequently, its k-value must decrease as the quasiparticle energy is conserved in the process. The group velocity $\mathbf{v} = \partial E(\mathbf{k})/\partial(\hbar\mathbf{k})$ slows down until it reaches zero when $|E| = \Delta$. At this point the effective charge of the quasiparticle excitation approaches zero, $q_k = u_n^2 - v_n^2 \to 0$. Thus we have an equal probability of adding an electron-like quasiparticle or removing an electron-like quasiparticle and adding a Cooper pair, see Fig. 2.3(b, left). When a Cooper pair is formed, the quasiparticle hole must have the energy $E_h = -E$ as the total energy (including the Cooper pair energy) must be conserved, $E_e + E_h = 2\mu$. The group velocity of the hole is almost exactly reversed. It is *retro-reflected* and retraces the path of the incoming electron, cp. Fig. 2.3(b, right).

BTK model

An extension to this simple picture was made by Blonder, Tinkham, and Klapwijk [21]. They added a δ-shaped potential barrier of strength Z at the interface to account for interface scattering and assumed a step-shaped pair potential. Within this model they calculated the scattering probabilities for all possible processes (see Fig. 2.3) that conserve energy and group velocity for transmission. For subgap energies, $|E| < \Delta$, all electrons must undergo ordinary reflection (**B**), or Andreev reflection (**A**). Ordinary reflection dominates at high barriers strengths, $Z \gg 1$, whereas all electrons will be Andreev reflected at a perfectly transparent interface (see Fig. 2.4). Based on the energy dependent transmission and reflection amplitudes, BTK calculate the current-voltage characteristic for contacts of arbitrary barrier strength assuming equilibrium Fermi distributions in normal metal and superconductor reservoirs.

Disorder

In the presence of disorder in the normal metal the assumptions of the BTK model are no longer valid. Transport is neither ballistic nor are transport properties defined by the barrier condition alone. Cooper pairs diffuse from the superconductor into the normal metal. These pair-correlated electrons modify the density of states in the normal metal ("proximity effect"). Similarly, the order parameter in the superconductor is suppressed by the presence of quasiparticles from the normal metal in the vicinity of the interface ("inverse proximity effect"). Both effects modify the transport properties in a normal metal-superconductor structure. In the framework of the Bogoliubov-de Gennes equations disorder must be introduced in the potential term explicitly, which makes calculations for diffusive systems a tedious task. In this case the non-equilibrium

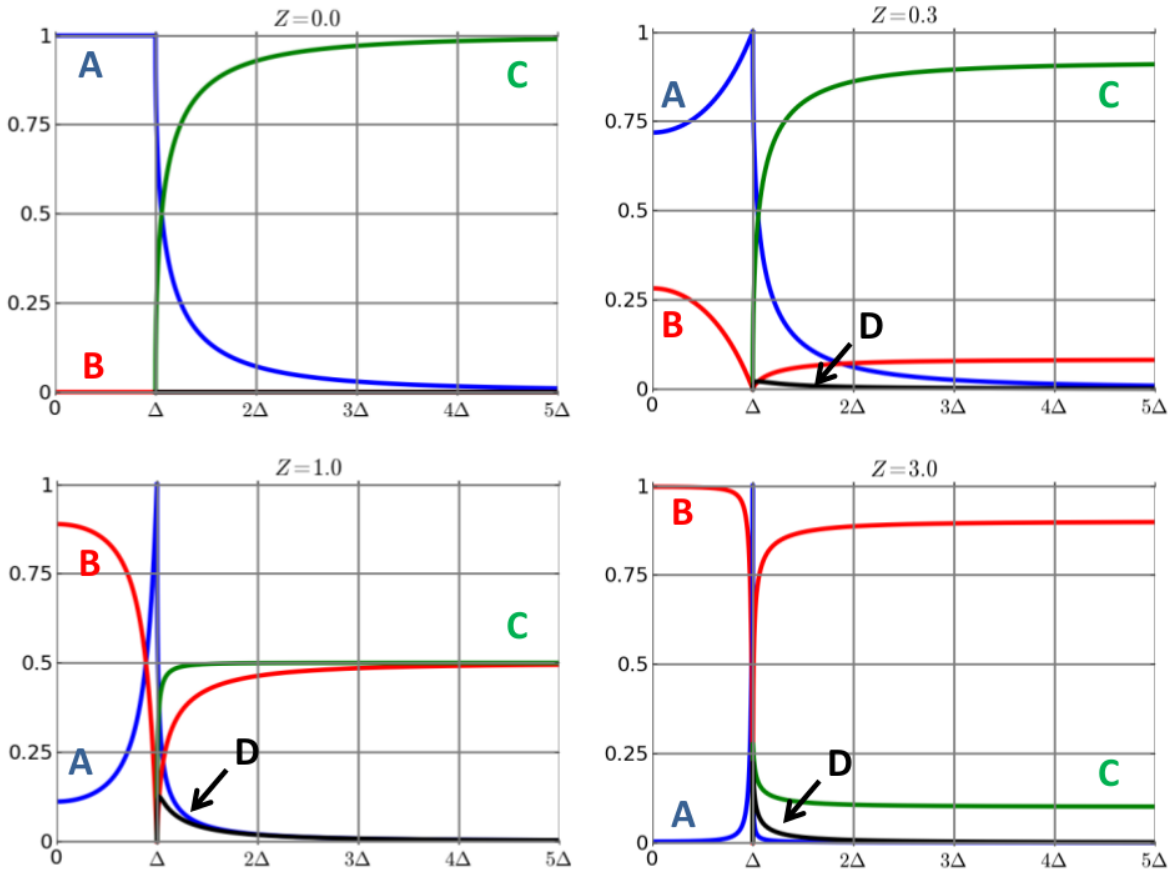

Figure 2.4: Transmission and reflection coefficients in the BTK model for barrier strength Z: (A) Andreev reflection, (B) ordinary reflection, (C) electron-like quasiparticle, (D) hole-like quasiparticle. (after: [21])

Green's function method is better suited for calculations. The added theoretical complexity is compensated by increased functionality in modeling complex problems, e.g. - for the case at hand - disorder scattering is added by introducing a self-energy term to the equation of motion of the quasi-classical Green's function and averaging over all possible scattering directions. In practice, one ends up with a system of coupled diffusion equations that must be solved to obtain the Green's functions from which spectral properties and occupation of non-equilibrium states are determined.

The purpose of the following section is to develop some of the basics of the Keldysh-Usadel formalism for the description of diffusive normal-metal superconductor contacts. The discussion follows the review papers by Belzig et al. [24], and Chandrasekhar [25], as well as the papers by Virtanen and Heikkilä [26] and Schmid and Schön [15]. Although the theoretical development of the equations is similar, individual authors use wildly different notations. The thesis of Machiel Geert Flokstra [27] was a big help in sorting through, and

comparing expressions in different notations. I decided to follow his notation convention below. With this theoretical background information, I will demonstrate a simple calculation of the *re-entrant resistance effect* which is observed in our experiments. Finally, I will outline how I implemented numerical calculations of the resistance of diffusive wires that contact a superconductor at a point contact with a barrier of arbitraty strength. The formalism for this problem was worked out by Tanaka et al. [28] based on previous work by Volkov et al. [29].

2.2 Non-equilibrium Green's function methods

2.2.1 Green's function description of superconductivity: The Gor'kov equation

The Green's function formalism describes particle transport by the evolution of expectation values of generalized density matrices [22]. The Green's functions have the form

$$G_{\alpha\beta}(x,x') = -i\langle T\psi_\alpha(x)\psi^\dagger_\beta(x')\rangle, \tag{2.19}$$

where the generalized coordinates, $x = (\mathbf{r}, t)$ are used and Greek indices, $\alpha, \beta = (\uparrow, \downarrow)$, describe the spin-states. The electron quasiparticle operators $\psi, \psi^\dagger$ are in the Heisenberg representation and fulfill anticommutation relationships

$$\left\{\psi_\alpha(x), \psi^\dagger_\beta(x')\right\} = \delta(x-x')\delta_{\alpha\beta}, \quad \{\psi_\alpha(x), \psi_\beta(x')\} = 0, \text{ and } \left\{\psi^\dagger_\alpha(x), \psi^\dagger_\beta(x')\right\} = 0.$$

The time-ordering operator T is introduced to indicate that operators are evaluated in the proper time sequence, adding a minus sign for each permutation of operators. The Green's function can be interpreted as the probability amplitude of a particle moving from x' with spin direction β to a point x and arriving there with its spin aligned in direction α. For $t > t'$ the particle is an electron and for $t < t'$ it describes a hole. Pair correlations are described by the so-called *anomalous* Green's function which is defined as

$$F_{\alpha\beta}(x,x') = -i\langle T\psi_\alpha(x)\psi_\beta(x')\rangle. \tag{2.20}$$

The anomalous Green's function can be related to the order parameter of the superconductor

$$\Delta_{\alpha\beta}(x) = -\lambda \lim_{x'\to x} F_{\alpha\beta}(x',x), \tag{2.21}$$

where the parameter λ describes the strength of the attractive interaction. We can arrange the Green's functions with respect to the spin-indices into 2×2 matrices which are marked with a hat-symbol (e.g. $\hat{G}$). To further compactify the notation we can combine the particle and hole operators in Nambu pseudo-spinors $\Psi^\dagger = (\psi_\uparrow^\dagger, \psi_\downarrow)$. The matrix Green's function in the combined Nambu⊗spin space is written

$$\check{G}(x,x') = \begin{pmatrix} \hat{G}(x,x') & \hat{F}(x,x') \\ \hat{G}^\dagger(x,x') & \hat{F}^\dagger(x,x') \end{pmatrix}, \quad \text{and} \quad \check{\Delta}(x) = \begin{pmatrix} 0 & \hat{\Delta}(x) \\ \hat{\Delta}^\dagger(x) & 0 \end{pmatrix}. \tag{2.22}$$

We are interested in stationary systems, therefore we can Fourier transform with respect to time and define the energy dependent Green's function

$$\check{G}(\mathbf{r},\mathbf{r}';E) = \int \mathrm{d}(t-t') \exp\left(\frac{-iE(t-t')}{\hbar}\right) \check{G}(\mathbf{r},\mathbf{r}';t,t').$$

Starting from the BCS Hamiltonian, Gor'kov wrote down the equations of motion for the Green's function [23],

$$\left\{H(\mathbf{r})\sigma_0 \otimes \tau_0 - E\sigma_0 \otimes \tau_3 - \check{\Delta}(\mathbf{r})\right\} \check{G}(\mathbf{r},\mathbf{r}';E) = \hbar\delta(\mathbf{r}-\mathbf{r}')\sigma_0 \otimes \tau_0, \tag{2.23}$$

where the matrices σ_i and τ_i are the standard Pauli matrices for spin and Nambu space respectively. The Hamiltonian of a single particle is $H(\mathbf{r}) = -\frac{\hbar^2}{2m}(\nabla_\mathbf{r} + \frac{q}{i\hbar}\mathbf{A})^2 + q\varphi$, where we included the vector potential $\mathbf{A}$ and the electrical potential φ.

2.2.2 The Usadel equation

Quasi-classical approximation

The Gor'kov equation (eqn. 2.23) provides a microscopic model of a superconducting system at the scale of the Fermi wavelength λ_F. However, it is rather impractical to work with the equation as most properties of interest vary on the size scale of Cooper pairs, i.e. the coherence length $\xi_S \gg \lambda_F$ is the relevant length scale of the problem. Thus we will make a quasi-classical approximation and integrate over the fast oscillating part of the Green's function $\check{G}$ associated with the relative coordinates $|\mathbf{r}-\mathbf{r}'|$ of the wavefunctions. The Fourier transform is sharply peaked at the Fermi surface around the relative momentum $\mathbf{p} \approx p_F\hat{\mathbf{p}} = p_F\frac{\mathbf{p}}{|\mathbf{p}|}$,

$$\check{g}(\mathbf{R} \equiv \left(\frac{\mathbf{r}+\mathbf{r}'}{2}\right), \hat{\mathbf{p}}, E) = \frac{i}{\pi}\int \mathrm{d}\xi_p \int \mathrm{d}(\mathbf{r}-\mathbf{r}')\check{G}(\mathbf{r},\mathbf{r}',E)\exp\left(-\frac{i}{\hbar}\mathbf{p}\cdot(\mathbf{r}-\mathbf{r}')\right), \tag{2.24}$$

where $\xi_p = v_F(p - p_F)$ is the part of the kinetic energy associated with the relative momentum, $v_F = p_F/m$ is the Fermi velocity and $\mathbf{v_F} = v_F\hat{\mathbf{p}}$.

The Gor'kov equation (eqn. 2.23) is expressed as a convolution of distribution functions. After taking the Fourier transform we can expand it as a Taylor series in the relative momentum $\mathbf{p}$ and the center-of-mass coordinate $\mathbf{R}$. By subtracting the Gor'kov equation from its conjugated form and keeping only linear terms we arrive at the Eilenberger equations of motion [24]

$$-i\hbar\mathbf{v_F}\partial_{\mathbf{R}} - \left[E\sigma_0 \otimes \tau_3 + \check{\Delta}, \check{g}(\mathbf{R}, \hat{p}, E)\right] = \left[\check{\Sigma}, \check{g}\right], \tag{2.25}$$

where electromagnetic terms have been omitted for simplicity.

Scattering processes and self-energy terms

On the right-hand side of the Eilenberger equations (eqn. 2.25), we inserted a new term that was not included in the form of the Gor'kov equation (eqn. 2.23) that was discussed earlier. Following Abrikosov and Gor'kov [23] self-energy terms $\check{\Sigma}$ can be used for adding scattering processes to the model. The real part of the self-energy term characterizes the change in energy due to the interaction ("mass renormalization") whereas the imaginary part is linked to the lifetime of the scattering state. Two important conditions must be met. Firstly, scattering processes must happen frequently so that we can interpret the self-energy term as statistical average over many scattering events. Secondly, the interaction energy is small compared to the molecular potential. In this case, the Born approximation can be used. The terms for elastic impurity scattering and magnetic impurity scattering become

$$\check{\Sigma}(\mathbf{R}, E) = \frac{i\hbar}{2\tau_{el}}\langle\check{g}(\mathbf{R}, \hat{\mathbf{k}}, E)\rangle_\Omega + \frac{i\hbar}{2\tau_{sf}}\sigma_3 \otimes \tau_0\check{g}(\mathbf{R}, \hat{\mathbf{k}}, E)\rangle_\Omega\sigma_3 \otimes \tau_0, \tag{2.26}$$

where the brackets denote averaging over all momentum directions. We introduced the elastic scattering time, τ_{el}, and the spin-flip time, τ_{sf}.

Angular averaging

In the dirty limit many scattering events happen before phase coherence (and thus the information about the initial momentum direction) is lost. The Green's functions become nearly isotropic. We can make an

ansatz for the dirty-limit Green's function

$$\check{g}(\mathbf{R}, \hat{\mathbf{p}}, E) = \check{g}_0(\mathbf{R}, E) + \hat{\mathbf{p}} \cdot \check{\mathbf{g}}_1,$$

with an isotropic part $\check{g}_0$ and a small momentum dependent correction $\check{\mathbf{g}}_1$ and insert this into eqn. 2.25. After averaging over all momentum directions and using the normalization condition $\check{g}^2 = \mathbb{I}$, we obtain the dirty-limit Usadel equation

$$i\hbar D \partial_{\mathbf{R}}(\check{g}_0 \partial_{\mathbf{R}} \check{g}_0) - \left[\check{\Delta} + E\sigma_0 \otimes \tau_3, \check{g}_0\right] = \left[\check{\Sigma}_{sf}, \check{g}_0\right]. \tag{2.27}$$

Here we use the diffusion constant $D = \frac{1}{3} v_f \ell$ and the elastic mean free path $\ell = v_F \tau_{el}$. The spin-flip term becomes

$$\check{\Sigma}_{sf} = \frac{i\hbar}{2\tau_{sf}} \sigma_3 \otimes \tau_0 \check{g}_0 \sigma_3 \otimes \tau_0. \tag{2.28}$$

In the absence of coherent spin-dependent interactions and unconventional pairing in the system, the symmetries

$$G_{\uparrow\uparrow} = G_{\downarrow\downarrow} = G, \qquad F_{\uparrow\downarrow} = -F_{\downarrow\uparrow} = F$$
$$G_{\uparrow\downarrow} = G_{\downarrow\uparrow} = 0, \qquad F_{\uparrow\uparrow} = F_{\downarrow\downarrow} = 0,$$

apply, and we can use a simplified, spin-independent Usadel equation

$$i\hbar D \partial_{\mathbf{R}}(\hat{g}_0 \partial_{\mathbf{R}} \hat{g}_0) - \left[\hat{\Delta} + E\tau_3, \hat{g}_0\right] = \left[\hat{\Sigma}_{sf}, \hat{g}_0\right], \tag{2.29}$$

with

$$\hat{g}_0 = \begin{pmatrix} G & iF \\ iF^\dagger & G^\dagger \end{pmatrix}, \ \hat{\Delta} = \begin{pmatrix} 0 & i\Delta \\ i\Delta^\dagger & 0 \end{pmatrix}, \text{ and } \hat{\Sigma}_{sf} = \frac{i\hbar}{2\tau_{sf}} \tau_3 \hat{g}_0 \tau_3. \tag{2.30}$$

2.2.3 Keldysh formalism

The Keldysh technique was developed to calculate out-of-equilibrium properties in many-body systems. Whereas the retarded Green's function, $\check{G}^R$, describes the propagation of quasiparticles forward in time and fully characterizes the equilibrium properties of a system (equivalently, the advanced Green's function, $\hat{G}^A$, can be used which propagates excitation states backward in time), the Keldysh Green's function $\hat{G}^K$ is defined as a combination of both, $\hat{G}^R$ and $\hat{G}^A$, and quantifies the occupation of quasiparticle states when

the system is driven out of equilibrium. The Green's functions are conveniently arranged in a matrix in "Keldysh" space,

$$\check{G} = \begin{pmatrix} \hat{G}^R & \hat{G}^K \\ 0 & \hat{G}^A \end{pmatrix},$$

which fulfills the normalization condition $\check{G}^2 = \mathbb{I}$. The spin-independent Usadel equation then has the form

$$\hbar D \nabla(\check{G}\nabla\check{G}) = -\left[\check{H}, \check{G}\right], \tag{2.31}$$

with

$$\check{H} = \begin{pmatrix} E & -\Delta \\ \Delta^* & -E \end{pmatrix} \tau_0.$$

Retarded and advanced Green's functions are related by $\hat{G}^A = -\tau_3(\hat{G}^R)^\dagger\tau_3$, thus we need to calculate only $\hat{G}^R$. As a consequence of the normalization condition, Schmid and Schön [15] found a parameterization of the Keldysh Green's function in terms of a generalized distribution matrix $\hat{f}$,

$$\hat{G}^K = \hat{G}^R\hat{f} - \hat{f}\hat{G}^A. \tag{2.32}$$

The matrix determines the occupation numbers in Nambu space and can be separated in two components

$$\hat{f} = f_L(x,E)\tau_0 + f_T(x,E)\tau_3, \tag{2.33}$$

where f_L is the even or "longitudinal" part (energy mode) and f_T the odd or "transversal" part (charge mode) of the distribution function. As previously encountered, the even/odd symmetry refers to inversion symmetry around the Fermi energy. The full distribution function is recovered by

$$f(x,E) = \frac{1}{2}\left(1 - f_L(x,E) - f_T(x,E)\right).$$

For calculations it is convenient to parametrize the Green's function by two complex angles, $\theta(x,E)$ and $\chi(x,E)$, thereby automatically satisfying the normalization condition. The parametrization reads

$$\hat{G}^R(x,E) = \begin{pmatrix} \cosh(\theta) & \sinh(\theta)\exp(i\chi) \\ -\sinh(\theta)\exp(-i\chi) & -\cosh(\theta) \end{pmatrix}. \tag{2.34}$$

The spin-independent Usadel equation (eqn. 2.31), can be broken down into 3 matrix equations. The equations which contain only $\hat{G}^R$ or $\hat{G}^A$ yield the *spectral equations* for the energy dependent solutions of $\theta(x, E)$ and $\chi(x, E)$. The mixed equation including the Keldysh Green's function, $\hat{G}^K$, provides us with a set of coupled diffusion equations for the non-equilibrium distribution functions f_L and f_T. The so-called *kinetic equations* describe the divergences of the spectral charge and energy current. A full set of equations including the generalized diffusion constants and other kinetic coefficients was worked out by Virtanen and Heikkilä and can be found in ref. [26], equations (7a) through (9e). The pair potential, if not assumed constant, must be solved self-consistently using equation (10). In this case, solutions to the spectral and kinetic equations, as well as the pair potential must be obtained iteratively until convergence is reached.

2.2.4 Proximity-effect and re-entrant resistance in a diffusive wire

A peculiar consequence of the proximity effect in diffusive wires is the phenomenon of re-entrant resistance: at low temperatures and low bias the dynamic resistance of the normal metal–superconductor contact approaches its normal state value. It is misleading to interpret this as an absence of the proximity effect or the presence of a barrier at the interface. In fact, re-entrant resistance is a result of the balance of enhanced conductance due to pair-correlated transport and the suppression of quasiparticle conductance because a pseudo-gap opens in the density of states at low energies as I will demonstrate below.

Length and energy dependence

At low temperatures the wavefunction coherence of Andreev-reflected pairs can extend quite far into the diffusive normal metal (cp. Fig. 2.5). At first it seems surprising that disorder scattering does not diminish pair correlations and proximity effect. The reason for this perceived contradiction is that the hole quasiparticle is (almost perfectly) retro-reflected and thus its wavefunction scatters at the same disorder potential as the incident electron. Electron and hole trajectories diverge only slowly as we move away from the interface.

Wavefunction coherence is lost when the total accumulated phase difference $\delta\varphi$ is of the order of π. Therefore, the coherence length for Andreev pairs at large energy is small. For an energy difference $\Delta E = E_e - E_h = 2E$, coherence will extend over a distance $L_E = \sqrt{D\tau} = \left(D\pi\frac{\hbar}{2E}\right)^{1/2} \approx \left(\frac{\hbar D}{E}\right)^{1/2}$. In the opposite limit of small energies, $E \approx 0$, the proximity effect is destroyed by inelastic scattering events. The dephasing length scale is $L_\varphi = \sqrt{D\tau_\varphi}$, where τ_φ is the time between inelastic scattering events. At higher temperatures the thermal distribution of quasiparticle states introduces another cut-off length for the proximity effect,

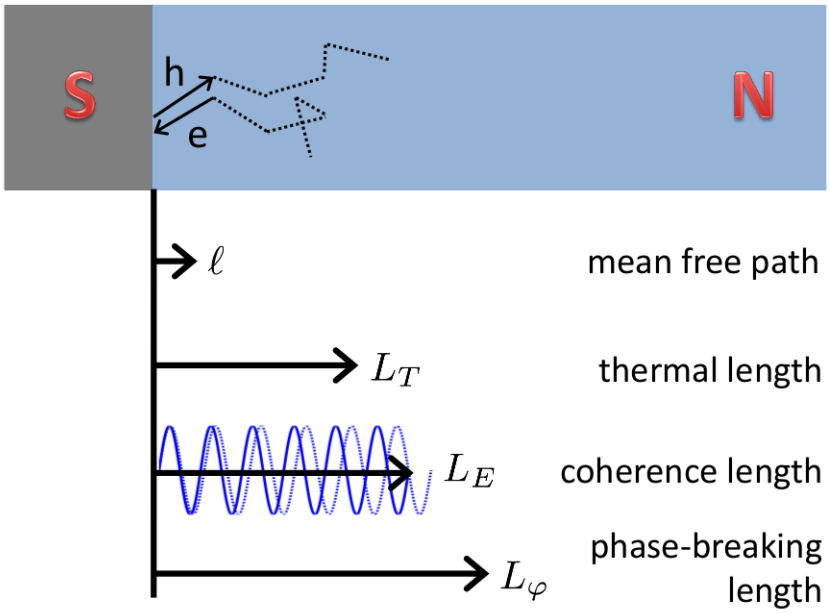

Figure 2.5: Relevant length scales for the proximity effect: Quasiparticles scatter elastically at the disorder potential with a mean free path ℓ between collisions. The wavefunction coherence is lost when the accumulated phase difference between the wavefunctions, $\delta\varphi$, approaches π. At low temperatures this limits the proximity effect to an effective length scale L_E between the thermal length, L_T, and the dephasing length due to inelastic processes, L_φ. The relative arrow lengths are chosen to reflect realistic sample parameters in the experiments. (After: [30])

the thermal length $L_T = \left(\frac{\hbar D}{2\pi k_B T}\right)^{1/2}$. In this case, the loss of coherence is not related to scattering events of individual pairs. We conclude that the effective coherence length of Andreev pairs varies between the thermal length L_T and the dephasing length L_φ in the low energy limit.

We will solve the Usadel equation in one-dimensional geometry (see Fig. 2.6) to quantify the energy dependence of the proximity effect and to calculate the resistance of a proximity wire. In the normal metal wire the pair potential is zero and (disregarding inelastic scattering) the spectral equations obtain a simple form

$$\hbar D\partial_x^2\theta = -2iE\sinh(\theta) + \frac{\hbar D}{2}(\partial_x\chi)^2\sinh(2\theta), \tag{2.35}$$

$$\partial_x j_E = 0, \quad \text{and} \quad j_E = 2\sinh(\theta)^2\partial_x\chi, \tag{2.36}$$

where j_E is the spectral supercurrent. We assume no interface barriers and set the phase angle at the superconductor side of the wire to its value in the superconducting reservoir $\theta(0, E) = \theta_S(E)$, which is

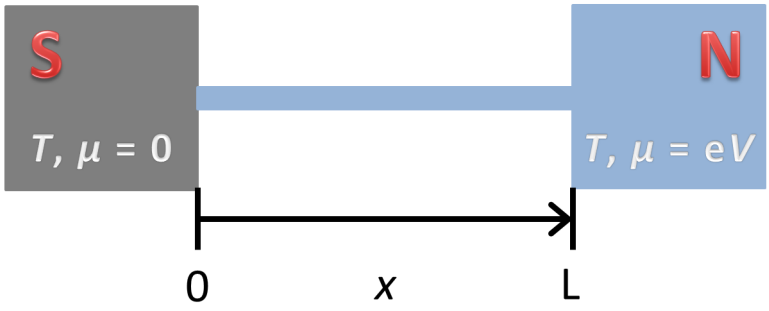

Figure 2.6: Geometry for re-entrant resistance calculation: A diffusive wire is connected to a superconducting reservoir at $x = 0$ and a normal reservoir at $x = L$.

determined from the quasiparticle density of states in the reservoir by

$$\cosh\theta_S(E) = \frac{E}{\sqrt{E^2 - |\Delta|^2}},$$

such that

$$\theta_S(E) = \begin{cases} -i\frac{\pi}{2} + \frac{1}{2}\ln\frac{|\Delta|+E}{|\Delta|-E} & \text{if } E < |\Delta|, \\ \frac{1}{2}\ln\frac{E+|\Delta|}{E-|\Delta|} & \text{if } E > |\Delta|. \end{cases}$$

At the normal metal reservoir, we set $\theta(L, E) = 0$. This implies that $\partial_x\chi = 0$ (see below). For the pairing potential in the superconductor we choose the value of bulk aluminum, $\Delta = 180$ μeV. The characteristic energy scale of the diffusive wire is the Thouless energy, which is related to the localization length L_φ by $E_C = \frac{\hbar D}{L_\varphi^2}$. In the absence of inelastic scattering the length of the wire sets the effective dephasing length for transport and we have $E_C \sim 10$ μeV for a typical sample. In the zero temperature limit, I solve the spectral equation numerically with a boundary value solver based on the `COLNEW` algorithm [31] to find the solution for $\theta(x, E)$. In figure 2.7 the (normalized) spectral density of states (DOS), Re $G_N = \mathrm{Re}[\cosh\theta(x, E)]$, is plotted as a function of distance from the superconductor x/L and compared to the (normalized) pair density of states (PDOS), $|\mathrm{Re}\ F_N| = |\mathrm{Im}[\sinh\theta(x, E)]|$. At low energies a pseudo-gap opens in the DOS close to the superconductor. In the same region the PDOS is large, indicating a strong proximity effect. At higher energies the coherence length decreases and the region of large PDOS does not extend far into the wire as expected from our previous discussion. Clearly, conductivity is enhanced due to pair correlated transport but, on the other hand, normal transport is suppressed due to a small DOS in the proximity region. To understand how this affects the resistance of the wire, we need to solve the kinetic Usadel equations.

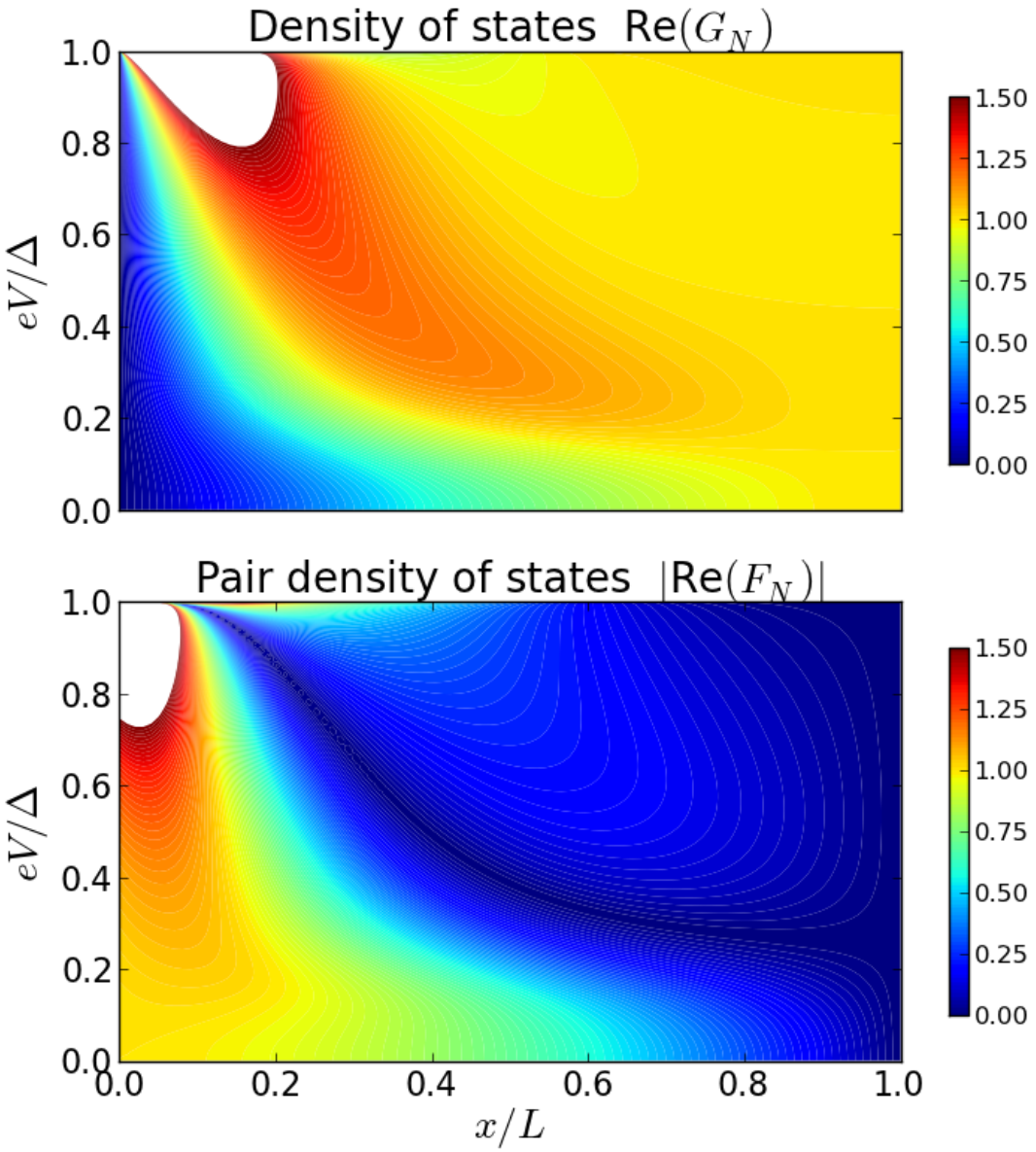

Figure 2.7: Contour plot of the spectral density of states and pair density of states in the proximity wire with $\Delta = 18\ E_C$ at zero temperature.

As a consequence of the boundary condition $\theta(0, E) = 0$, the spectral supercurrent is zero at $x = L$. Current conservation implies that it, therefore, vanishes everywhere in the wire, $j_E(x, E) = 0$. Thus we also

have $\partial_x \chi = 0$. The kinetic equations decouple and we find for the spectral charge current density, j_c,

$$\begin{aligned} \hbar D \nabla j_c &= 0, \\ j_c &= \mathcal{D}_T \nabla f_T, \qquad (2.37) \\ \mathcal{D}_T &= \cosh^2 \left[\mathrm{Re}\ \theta(x,E) \right], \qquad (2.38) \end{aligned}$$

where $\mathcal{D}_T$ is the spectral charge diffusion coefficient which modifies the local spectral conductance of the wire. The spectral charge current $J(E)$ is constant along the wire. We calculate it by integrating equation 2.37,

$$f_T(x,E) = J(E) \int_0^x \frac{\mathrm{d}x'}{\mathcal{D}_T(x',E)} + c(E),$$

and applying the boundary conditions for f_T with a voltage V applied to the normal metal reservoir,

$$\begin{aligned} f_T(0,E) &= 0, \qquad (2.39) \\ f_T(L,E) &\equiv f_{TL}(E,V) = \frac{1}{2} \left[\tanh\left(\frac{E+eV}{2k_\mathrm{B}T} \right) - \tanh\left(\frac{E-eV}{2k_\mathrm{B}T} \right) \right]. \qquad (2.40) \end{aligned}$$

For the total current we find

$$\begin{aligned} I(V) &= \frac{L}{R_N} \int_0^\infty J(E) = \frac{1}{R_N} \int_0^\infty \mathrm{d}E\ \mathcal{D}(E) f_{TL}(E,V), \qquad (2.41) \\ \mathcal{D}(E) &= \frac{1}{\frac{1}{L}\int_0^L \frac{\mathrm{d}x}{\mathcal{D}_T(x,E)}}. \qquad (2.42) \end{aligned}$$

The spectral conductance $\mathcal{D}(E)$ shows two characteristic peaks (see Fig. 2.8). The first peak appears at $E \approx 5E_C$ and is related to the wavefunction coherence. The second peak at the gap energy is due to the divergence of the density of states in the superconductor. Most remarkably, in the limit of small energies, $E \to 0$, the spectral conductance $\mathcal{D}(E) \to 1$. The resistance of the wire approaches the normal state resistance, R_N (see Fig. 2.9). Although a proximity effect is present and the magnitude of the pair density varies along the wire, at $E = 0$ the spectral diffusion coefficient $\mathcal{D}_T$ coincides with its normal state value everywhere. The solution for $\theta(x,0)$ is purely imaginary and $\mathcal{D}_T = \cosh^2[\mathrm{Re}\ \theta(x,0)] = 1$. This exact cancellation of the effect of a diminished density of states and the conductivity enhancement from pair transport is the origin of the *re-entrant resistance* effect in diffusive proximity wires.

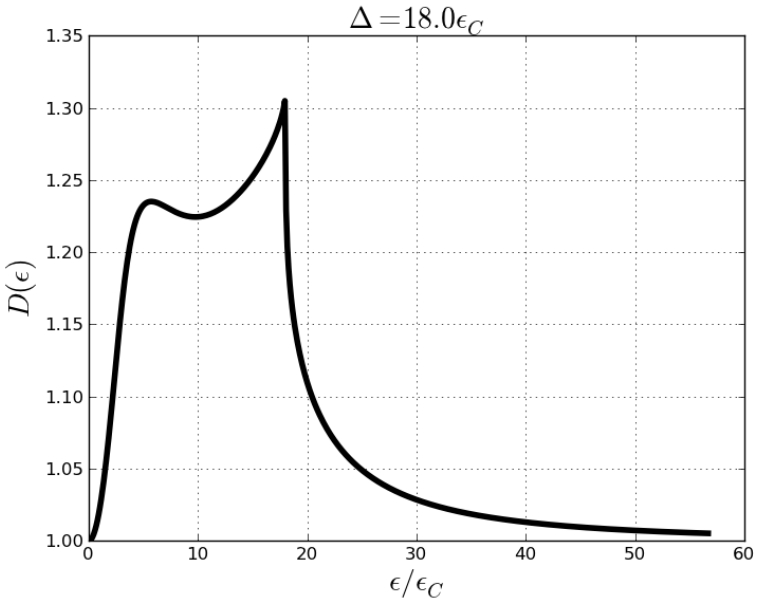

Figure 2.8: The spectral conductance $\mathcal{D}(E)$ as a function of energy E. It has two peaks: the first peak at $E \approx E_C$ is related to wavefunction coherence whereas the second peak is due to the large density of states in the superconductor at the gap energy.

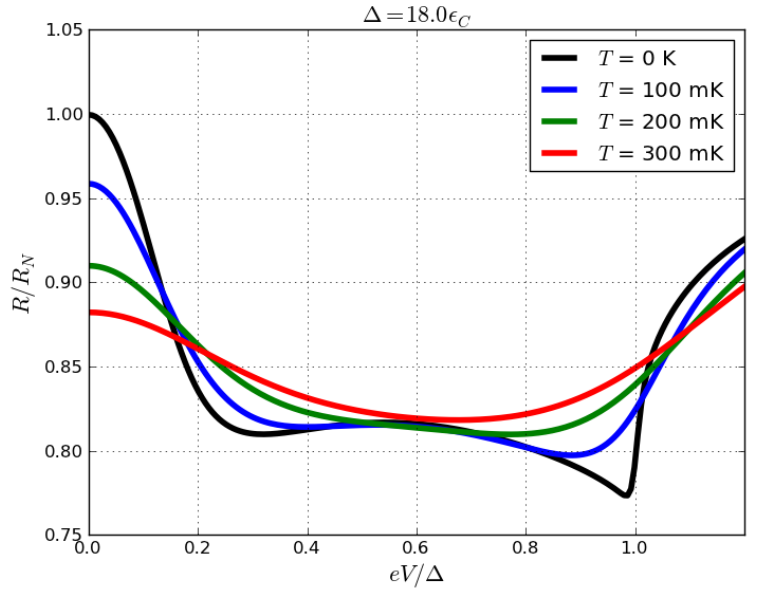

Figure 2.9: The resistance of a proximity-coupled wire at different temperatures T. For the pair potential of the superconductor I chose the bulk gap of aluminum, $\Delta = 180$ μeV. The Thouless energy of the wire was set to a typical value of $\epsilon_C = 10$ μeV. At zero temperature and zero bias voltage the wire resistance goes back to its normal state value, R_N. At higher temperatures the thermal length limits the extend of the proximity region. The spectral conductance peaks are washed out by the thermal distributions in the reservoirs and are no longer apparent in the resistance curves.

2.2.5 Resistance calculation with interface barriers

So far we neglected interface barriers in the discussion. However, in experiments typically a disorder region or barrier forms between normal metal and superconductor. The formalism to describe point-contacts of arbitrary barrier strength and different ratios of wire resistance, R_d, and barrier resistance, R_b, was worked out by Tanaka et al. [28]. They implemented the boundary condition for an arbitrary connector between diffusive metals that was provided by Nazarov in the framework of the "generalized" circuit theory [32].

In circuit theory the interface is modeled by two isotropization zones connected by two ballistic zones to the scattering zone in the center of the contact. The ballistic zones and scattering zones are much shorter than the coherence length. Here, the scattering zone is modeled as a delta potential at $x = 0$, $U(x) = H\delta(x)$. The point contact is described by a set of transparencies $T_m = \frac{4\cos^2\phi}{4\cos^2\phi + Z^2}$ with a dimensionless constant $Z = \frac{2H}{\hbar v_F}$. The injection angle ϕ is measured from the interface normal. The Fermi velocity is given by v_F. If we disregard the angular dependence, we will assign the same transmission coefficient to all channels, $T_m = \frac{1}{1+Z^2}$.

Nazarov's generalized boundary condition for the spin-independent Usadel equation (eqn. 2.31) is

$$\frac{L}{R_d}\left(\check{G}_N \frac{\partial \check{G}_N}{\partial x}\right)\Big|_{x=0_+} = \frac{\langle B\rangle}{R_b}, \tag{2.43}$$

$$B = \frac{2T_m\left[\check{G}_N(0_+), \check{G}_S(0_-)\right]}{4 + T_m\left(\left\{\check{G}_N(0_+), \check{G}_S(0_-)\right\} - 2\right)}, \tag{2.44}$$

where the indices $x = \{N, S\}$ of the matrix Green's functions $\check{G}_x$ denote normal metal and superconductor, respectively. The averages are carried out over all particle injection angles

$$\langle B(\phi)\rangle = \frac{\int_{-\pi/2}^{\pi/2} \mathrm{d}\phi\ B(\phi)\cos\phi}{T_{avg}}.$$

where $T_{avg} = \int_{-\pi/2}^{\pi/2} \mathrm{d}\phi\ T_m(\phi)\cos\phi$ is the average transmission. The boundary resistance R_b can be related to the Sharvin resistance $R_S = \frac{4\pi^2\hbar}{e^2 k_F^2 S}$, where k_F is the Fermi wave vector and S the effective cross section area. We have $R_b = \frac{2R_S}{T_{avg}}$. The effective cross section S is not necessarily equal to the cross section of the normal conductor, therefore we can treat R_b as an independent parameter of the theory.

Tanaka et al. [28] use a different parametrization of the Green's function, $\hat{G}^R = \tau_3\cos\theta + \tau_2\sin\theta$. However, the derivation of the equation for the total current proceeds exactly as in section 2.2.4. To create a more realistic model I added an inelastic scattering term and a spin-flip term to the spectral equation. The

complete set of equations is given in the Appendix A. It suffices to numerically solve the spectral equation and obtain θ and $\partial_x\theta$. I used the same boundary value solver based on `COLNEW` [31] as in the previous section. The contribution of the boundary resistance to the spectral conductance can be calculated from the values of θ and $\partial_x\theta$ at the NS boundary,

$$I(V) = \frac{L}{R_d}\int_0^\infty \mathrm{d}E\ \mathcal{D}_T(0)\left(\frac{\partial f_T}{\partial x}\right)\Big|_{x=0+} = \int_0^\infty \mathrm{d}E \frac{f_{TL}(E,V)}{\frac{R_b}{\langle I_{b0}\rangle} + \frac{R_d}{L}\int_0^L \frac{\mathrm{d}x}{\mathcal{D}_T(x,E)}}, \tag{2.45}$$

where $I_{b0} = I_{b0}\left[\theta(0), \partial_x\theta(0_+)\right]$ is related to the matrix current for transmission across the boundary (eqn. 2.44). It depends on the transmission coefficients and the density of states on both sides of the boundary. From equation 2.45 the resistance of a proximity wire that is attached to a superconductor at a point-contact with arbitrary interface barrier can be calculated. This allows for realistic modeling of NS contacts in experiments. However, we assumed ideal reservoirs at both ends of the wire and thus we are neglecting nonequilibrium effects in the superconductor.

Gap suppression effects and the resulting charge imbalance can be modeled by solving the Usadel equations in the superconductor self-consistently. In the absence of interface barriers the self-consistent calculations can be performed using the `USADEL1` code by Pauli Virtanen and Tero T. Heikkilä [26, 33]. The code is a solver for the quasi-classical equations on a 1-dimensional network. Besides self-consistent calculations, I also used this code to model constrictions in the normal metal wire and for consistency checks on my own codes. The code allows to vary the pairing interaction parameter $\lambda(x)$ in the superconducting wire. In an overlap region of a superconductor and a normal metal the effective strength of the pairing interaction decreases and λ is approximated by [34]

$$\lambda = \lambda_0 \frac{d_S}{d_S + d_N}, \tag{2.46}$$

where d_S and d_N are, respectively, the thicknesses of the superconducting and normal metal films, and λ_0 is the pairing strength in the unperturbed superconductor. The calculations show an increase in the resistance due to charge imbalance in the superconductor when the bias exceeds the value of the suppressed gap. Similar features are observed in the experiments and will be discussed later.

2.3 Shot noise in mesoscopic wires and normal metal-superconductor devices

2.3.1 Current fluctuations

In an electrical device current fluctuates with time t around an average value $\langle I\rangle$, $\Delta I = I(t) - \langle I\rangle$. Current noise is defined as the spectral density of current fluctuations, i.e. the mean square fluctuations of ΔI per unit bandwidth. In a bandwidth $\Delta\omega$ around the center frequency ω, the fluctuation amplitude is given by

$$\Delta I_{\omega,\Delta\omega}(t) = \frac{1}{2\pi}\int_{\omega-\Delta\omega/2}^{\omega+\Delta\omega/2}\left[\Delta I(\omega)\exp(-i\omega t) + \Delta I^*(\omega)\exp(i\omega t)\right]\mathrm{d}\omega \ ,$$

where $\Delta I(\omega)$ is the spectral component of the current fluctuation at frequency ω. For a small interval $\Delta\omega = 2\pi\Delta f \ll \omega$ the power spectral density is then defined as

$$S_I(\omega) \equiv \frac{\langle(\Delta I_{\omega,\Delta\omega})^2\rangle}{\Delta f}. \tag{2.47}$$

To evaluate the frequency dependence of 2.47, we need to look at the ensemble average of the correlation function between current fluctuations at different times t_0 and $t_0 + t$: $\langle\Delta I(t_0)\Delta I(t_0+t)\rangle_\alpha$. In an ergodic system we can replace $\langle\ldots\rangle_\alpha$ by the time average $\langle\ldots\rangle_{t_0}$. The Wiener-Khintchine theorem [35] then states that

$$S_I(\omega) = 2\int_{-\infty}^{\infty}\langle\Delta I(t_0)\Delta I(t_0+t)\rangle\exp(i\omega t)\mathrm{d}t. \tag{2.48}$$

In most physical system a typical time scale τ exists over which current correlations decay. It is often shorter than the sampling time $1/\omega$ in the experimental observation. In this limit the average over the correlations in the sampling interval is a frequency-independent constant. A constant, "white" noise spectrum is observed at low frequencies. Shot noise and thermal noise have a white noise spectrum. If the system comprises of a number of two-level systems with a broad distribution of switching frequencies, the resulting spectrum will have a $1/f$-frequency dependence.

2.3.2 Shot noise and universal value

Shot noise is a consequence of the discreteness of electric charge. The effect was first observed by Walter Schottky in vacuum diodes. Due to the statistical nature of the electron emission the number of charge quanta N emitted per time period T fluctuates and is described by Poissonian statistics, i.e. the mean square deviation equals the mean $\left\langle(\Delta N)^2\right\rangle = \langle N\rangle$. Thus the electrical current will fluctuate around its

mean value $\langle I\rangle = e_0\langle N\rangle/T$ with a mean square deviation of

$$\left\langle (\Delta I)^2 \right\rangle = \frac{e^2\left\langle (\Delta N)^2 \right\rangle}{T^2} = \frac{e\langle I\rangle}{T} \ .$$

Using the definition of noise spectral density and the Wiener-Khintchine theorem we find the relation between current noise and average transmitted current

$$S_I = 2e\langle I\rangle \ . \tag{2.49}$$

This scaling proportionality is characteristic of shot noise and therefore named the *universal value*.

2.3.3 Shot noise in mesoscopic devices

Fermions at a barrier: partition noise

Before discussing shot noise in mesoscopic devices let us first take a look at a simple toy model [36]: a beam of fermions at a tunnel barrier (Fig. 2.10). At zero temperature all states in the incoming Fermion beam are occupied $\langle n_{in}\rangle = 1$ and therefore the mean-square fluctuations are zero. A tunnel barrier with barrier transmission $T = 1-R$ splits the beam in to a transmitted beam with average occupation number $\langle n_T\rangle = T$ and a reflected beam with $\langle n_R\rangle = R$. We assume that there are no interactions between the fermions in the beams. The scattering of a fermion at the barrier is independent of scattering events of other fermions, hence $\langle n_T n_R\rangle = 0$. Mean-square fluctuations in the occupation numbers of outgoing particle beams must, of course, be identical and opposite to the occupation number correlation between the two beams. They are given by $\langle(\Delta n_T)^2\rangle = \langle(\Delta n_R)^2\rangle = -\langle\Delta n_T \Delta n_R\rangle = TR$, where $\Delta n_x = n_x - \langle n_x\rangle$. Fluctuations of this kind are called *partition noise* as the barrier splits the incoming beam in to two outgoing beams.

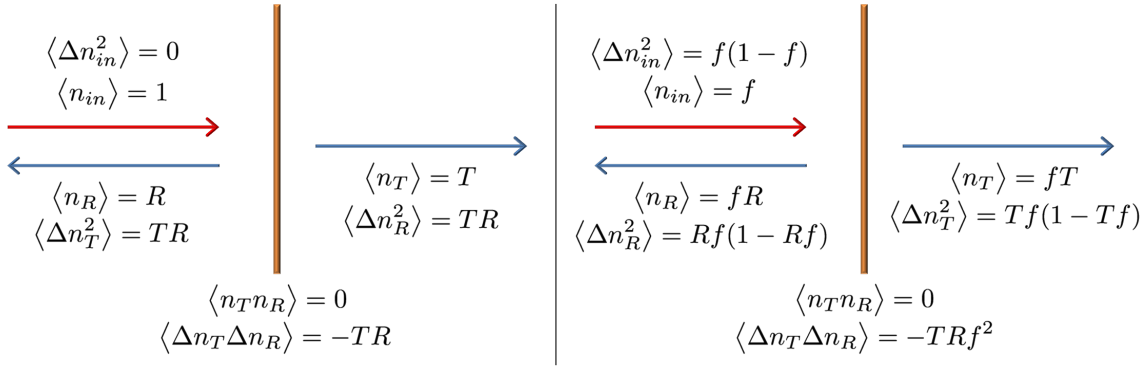

Figure 2.10: Tunneling barrier as a beam-splitter: (left panel) zero-temperature (right panel) finite temperature.

At finite temperature the occupation number for incoming fermions is given by the Fermi distribution function f, $\langle n_{in}\rangle = f$. As a consequence the occupation numbers of transmitted and reflected beam are also scaled with the Fermi distribution function and the mean-squared fluctuations in the occupation numbers are now given by

$$\langle(\Delta n_T)^2\rangle = Tf(1-Tf) \ , \tag{2.50}$$

$$\langle(\Delta n_R)^2\rangle = Rf(1-Rf) \ , \tag{2.51}$$

$$\langle\Delta n_T \Delta n_R\rangle = -TRf^2 \ . \tag{2.52}$$

For a perfect conductor with many indistinguishable carriers we can relate the occupation numbers and mean-square fluctuations above to current and current noise. For a carrier stream with velocity $v(E)$ and charge carrier energy E the current is $\mathrm{d}I = ev(E)\mathrm{d}\rho(E)$, here $\mathrm{d}\rho(E)$ is the number of charge carriers per unit length in the energy range. We can rewrite the charge carrier density terms of the occupation number and density of states $\nu(E) = 1/(2\pi\hbar v(E))$,

$$\mathrm{d}\rho(E) = n(E)\nu(E)\mathrm{d}E = \frac{e}{2\pi\hbar}n(E)\mathrm{d}E \ . \tag{2.53}$$

Time-dependent changes of occupation numbers must be examined carefully. For occupation numbers which vary slowly in time, equality 2.53 still holds [36] and fluctuations in current and occupation number are related. We calculate the transmitted current and noise spectral density

$$\langle I\rangle = \frac{e}{2\pi\hbar}\int \mathrm{d}E \ Tf \ , \tag{2.54}$$

$$S_I = 2\frac{e^2}{2\pi\hbar}\int \mathrm{d}E \ Tf(1-Tf) \ , \tag{2.55}$$

by Fourier transforming the noise power $S_I = e^2\int \mathrm{d}E S_{nn}(E)$ and using the identity $S_{nn}(E) = \frac{1}{\pi\hbar}\langle\Delta n\Delta n\rangle$ which is true for particles arriving at rate $\mathrm{d}E/(2\pi\hbar)$ and contributing with mean-square fluctuation of the occupation number to the noise. In the limit of a tunnel junction $T \ll 1$ and $f \ll 1$, we obtain the universal value for shot noise, $S_I = 2e\langle I\rangle$.

Mesoscopic two-point conductor

With the results of last section in mind, it is straightforward to generalize to an arbitrary two-point conductor. In the Landauer-Büttiker formalism transport in a mesoscopic conductor is modeled as a scattering problem

for wavefunctions that are solutions of the single-particle Schrödinger equation. All the information about the conductor is encoded in a scattering matrix which describes the transformation between the wavefunctions of incoming and outgoing scattering states, see Fig. 2.11. The conductor is connected to two reservoirs with temperatures T_L, T_R and chemical potentials μ_L, μ_R, which define the energy distributions of incoming electron states. Amplitudes for the incoming wavefunctions are represented by $\hat{a}_L$, $\hat{a}_R$ and for the reflected wavefunctions by $\hat{b}_L$, $\hat{b}_R$.

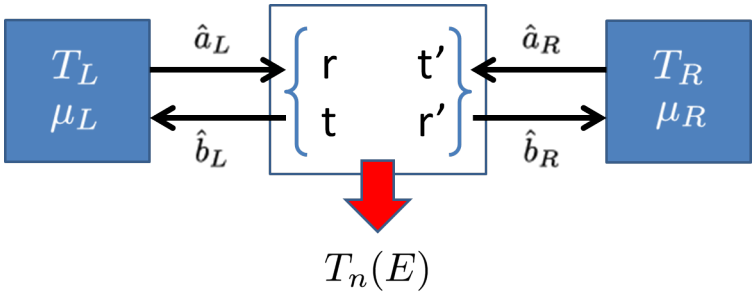

Figure 2.11: Scattering formalism for transport in a mesoscopic conductor: The conductor is fully described by a scattering matrix connecting the amplitudes of the incoming scattering states $\hat{a}_x$ and outgoing states $\hat{b}_x$. The energy distribution of incoming states is defined by the attached reservoirs of temperature T_x and chemical potential μ_x.

From the off-diagonal blocks of the scattering matrix we can construct the transmission matrix $T = t^\dagger(E)t(E)$. This matrix describes the transmission probability and phase for charge carrier transport through the conductor [22]. In the eigenbasis of T the current through the conductor can be written as a sum over transmission channels n with the transmission coefficient given by the eigenvalue $T_n(E = E_n)$ of T. We have

$$\langle I_L \rangle = \frac{e}{2\pi\hbar} \sum_n \int \mathrm{d}E \; T_n(E)[f_L(E) - f_R(E)] \; . \tag{2.56}$$

The formula for noise spectral density of the current fluctuations has a similar structure to equations 2.3.3. Here we separate the equilibrium noise contributions (first two terms) from the shot noise part (last term) and write

$$S_I = \frac{e^2}{\pi\hbar} \sum_n \int \mathrm{d}E \big\{ T_n(E)[f_L(1 - f_L) + f_R(1 - f_R)] + T_n(E)[1 - T_n(E)](f_L - f_R)^2 \big\} \; .$$

The shot noise contribution is second-order in distribution functions and positive for fermions. For high energies, Bose distribution and Fermi distribution are both approximated by the Maxwell-Boltzmann distribution. Similarly, it can be seen that the shot noise term becomes much smaller than the equilibrium contributions to the noise and can be neglected. The energy integral can be carried out explicitly, if the

transmission coefficients $T_n(E)$ are approximately constant at the energy scale of the applied voltage bias, V, and temperature, T. Thus we can replace them with the value at Fermi energy $T_n \equiv T_n(E_F)$ and obtain

$$S = \frac{e^2}{\pi\hbar}\Big[2k_BT\sum_n T_n + eV\coth\big(\frac{eV}{2k_BT}\big)\sum_n T_n(1-T_n)\Big]\ . \tag{2.57}$$

Equation 2.57 describes a smooth crossover between Johnson noise, $S = 4k_BTG$, of a conductor with conductance $G = \frac{e}{2\pi\hbar}\sum_n T_n$, and shot noise in the high bias regime, $V \ll k_BT/e$. Only in the tunneling limit, $T_n \ll 1$, we obtain the universal value for shot noise. In fact, from equation 2.57 we see that fully open channels, $T_n = 1$, and closed channels, $T_n = 0$, do not contribute to noise at all. The suppression of shot noise (or *sub-Poissonian* shot noise) is an important result of the transmission characteristic in mesoscopic devices and was studied experimentally and theoretically in many different systems. As we will discuss later, wavefunction coherence along the whole device is not required.

The amount of shot noise suppression is quantified by the *Fano factor* which is defined as the ratio of actual shot noise to the ideal Poissonian value,

$$F \equiv \frac{S}{S_{\text{Poisson}}}\ . \tag{2.58}$$

Another quantity that is often reported is the differential Fano factor. It is a particularly useful measure when the effective charge carrier of transport changes with bias, i.e. at the crossover between Andreev transport ($q = 2e$) and ordinary quasiparticle transmission ($q = e$) at the gap energy of NS contacts. The differential Fano factor is defined as

$$F_d \equiv \frac{1}{2e}\frac{\mathrm{d}S}{\mathrm{d}I} \tag{2.59}$$

2.3.4 Diffusive metallic wires

In a diffusive metallic wire the mean-free path for elastic scattering due to disorder, ℓ, is much smaller than the wire length, L, but greater than the localization length $L_\xi = N_\perp\ell$ of the wire. The wire is assumed to have quasi-1 dimensional geometry with a small but finite width, w, and $N_\perp = \frac{P_F w}{\pi\hbar}$ transverse channels. From a comparison with the Drude conductance one could come to the conclusion that all transmission channels should have a small transmission coefficient $T \sim \frac{w}{L}$. This is incorrect. In a metallic conductor we also find open channels ($T \sim 1$) and closed channels ($T \ll 1$) [39]. The transmission eigenvalues are related to the channel dependent localization lengths, ζ_n, by $T_n = \cosh^{-2}(L/\zeta_n)$ [37]. Random matrix theory further tells that the ζ_n are uniformly distributed in the interval $[0, \ell^{-1}]$. As a consequence the distribution

of transmission coefficients is bi-modal (see Fig. 2.12) and follows

$$P(T) = \frac{l}{2L}\frac{1}{T\sqrt{1-T}},\ T_\ell < T < 1\ , \tag{2.60}$$

$$P(T) = 0,\ T < T_\ell = 4\exp(\frac{-2L}{\ell})\ . \tag{2.61}$$

For this eigenvalue distribution the conductance scales correctly, $\sum_n P(T_n)T_n = \frac{\ell}{L}$, and the transmission factor term in the shot noise formula becomes $\sum_n P(T_n)T_n(1-T_n) = \frac{\ell}{3L}$. Thus shot noise is suppressed with a Fano factor $F = \frac{1}{3}$ [38]. The result is a fundamental property of transport in diffusive wires and was derived for different models of diffusive transport. In the framework of classical theory Nagaev [40] calculated shot noise suppression using the Boltzmann equations and Langevin sources. Microscopic calculations were performed by several authors [41, 43]. In the microscopic framework Nazarov showed that the transmission statistics (eqn. 2.61) remains valid for arbitrary geometry [42] and for the Boltzmann-Langevin approach Sukhorukov and Loss proved that shot noise is universal for arbitrary multiterminal diffusive conductors [44].

Experiments on diffusive conductors were carried out by Liefrink et al. [45] in wires of a (Al,Ga)As heterostructure with a two-dimensional electron gas (2DEG) and by Steinbach et al. [46] in long silver wires. Both showed shot noise suppression. Later a precise measurement of the 1/3-suppression was obtained by Henny et al. [47] on gold wires which were attached to large reservoirs to suppress electron heating effects. Figure 2.13 shows shot noise data of a diffusive copper wire. The measurement was carried out in SQUID

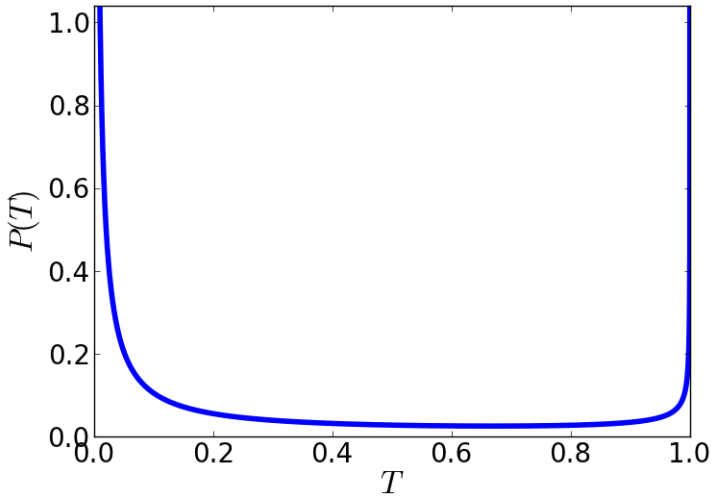

Figure 2.12: Bimodal distribution of transmission eigenvalues of a diffusive metallic wire with $L/\ell = 50$.

resistance bridge configuration (see chapter 4) at a temperature $T = 150$ mK. It shows excellent agreement with the theoretically predicted suppression factor 1/3.

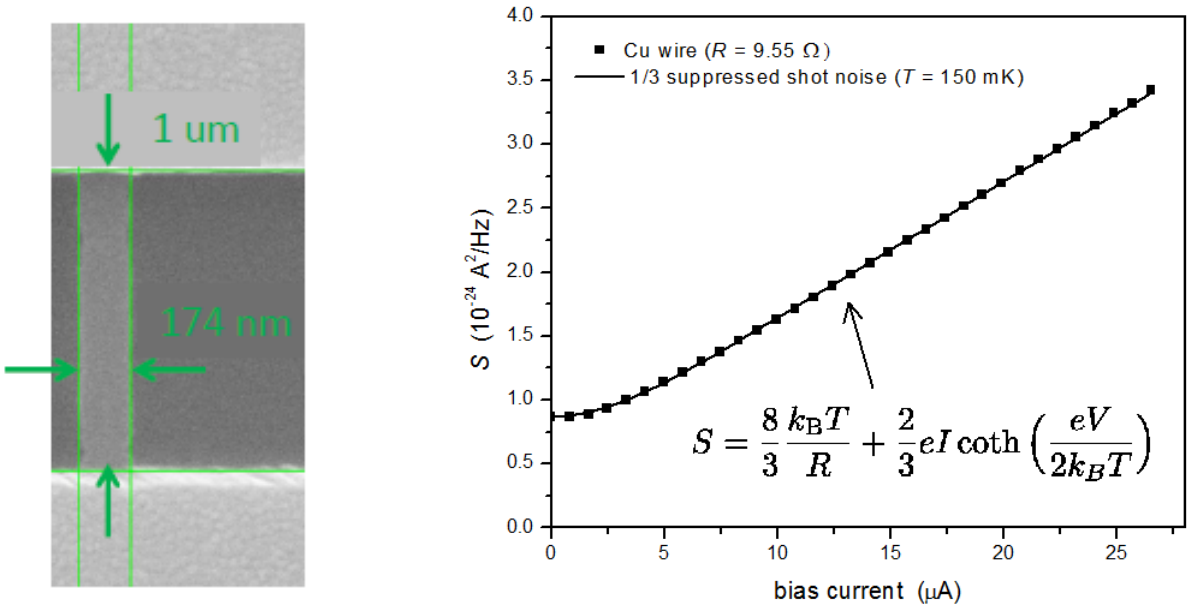

Figure 2.13: Shot noise in a diffusive copper wire: (left panel) SEM micrograph of at 25 nm thick copper wire which is attached to two 200 nm thick copper reservoirs with lateral dimensions of 1 mm × 1 mm. The sample was fabricated by e-beam lithography and shadow-angle evaporation. Sample dimensions are indicated in the micrograph. The device resistance is 9.55 Ω. (right panel) The shot noise was measured with the SQUID resistance bridge method in our dilution refrigerator at a temperature $T = 150$ mK.

2.3.5 Andreev reflection

The scattering formalism can also be applied to Andreev reflection at a normal metal-superconductor boundary. In this case, we choose the scattering states to be solutions of the Bogoliubov-de Gennes equations. Following de Jong and Beenakker [48] we write the wavefunction in the normal metal lead

$$\psi_\alpha(\epsilon) = \varphi^+_\alpha(\epsilon) + \sum_\beta r_{\beta\alpha}(\epsilon)\varphi^-_\beta(\epsilon) \ ,$$

where the Greek indices denote mode number and quasiparticle species (electron or hole). The normalized wavefunctions φ^+, φ^- carry unit flux. The matrix $\mathbf{r}$ describes the reflection process at the NS boundary. It

is unitary, i.e. it conserves quasiparticle number, and has block form:

$$\mathbf{r} = \begin{pmatrix} \mathbf{r}_{ee} & \mathbf{r}_{eh} \\ \mathbf{r}_{he} & \mathbf{r}_{ee} \end{pmatrix} . \tag{2.62}$$

The off-diagonal blocks convert incoming electrons into outgoing holes (and *vice versa*). The matrix $\mathbf{R} = \mathbf{r}_{he}\mathbf{r}_{he}^{\dagger}$ describes Andreev transmission at the NS interface, which transfers a charge $q_{\rm eff} = 2e$ across the boundary. In the limit $\epsilon \to 0$ the eigenvalues of $\mathbf{R}$, $\mathcal{R}_n$, can be expressed in terms of the transmission coefficients of the normal metal region [38],

$$\mathcal{R}_n = \frac{T_n^2}{(2-T_n)^2} .$$

Here the assumption is made that the pair potential is a step function at the NS boundary and higher order terms in $(\Delta/E_F)^2$ are neglected. In the zero temperature limit we can evaluate the conductance and shot noise of the NS junction from the conductance formula and eqn. 2.57. A rigorous derivation (cp. discussion in [49]) shows that we must replace the transmission eigenvalues of ordinary quasiparticle transmission with the Andreev reflection eigenvalues $T_n \to \mathcal{R}_n = \frac{T_n^2}{(2-T_n)^2}$ and the charge by the effective charge that is transported across the NS interface, $e \to 2e$. We find

$$G_{\rm NS} = 2\frac{e}{2\pi\hbar}\sum_n \mathcal{R}_n = \frac{e}{h}\sum_n \frac{2T_n^2}{(2-T_n)^2} , \tag{2.63}$$

$$S = 2e|I|\sum_n 4\mathcal{R}_n(1-\mathcal{R}_n) = 2e|I|\sum_n \frac{16T_n^2(1-T_N)}{(2-T_n)^4} . \tag{2.64}$$

This result can be used to describe the noise of tunnel barrier with uniform tunnel transparency for all channels, $T_n = \Gamma$, at the NS interface,

$$P_{\rm NS} = \frac{8(1-\Gamma)}{(2-\Gamma)^2}2e|I| \xrightarrow{\Gamma \ll 1} 4e|I| .$$

In the limit of a tunnel junction with high barrier we obtain twice the Poissonian value for shot noise (*super-Poissonian* noise) because the amount of transferred charge in the stochastic transmission process has doubled. In the opposite limit of a transparent interface the transmission eigenvalues are determined by the normal metal contact and follow the distribution in eqn. 2.61. We also find shot noise doubling,

$$S = 2e|I|\sum_n P(T_n)\frac{16T_n^2(1-T_N)}{(2-T_n)^4} = \frac{4}{3}e|I| , \tag{2.65}$$

compared to the diffusive wire which is attached to a normal reservoir. Still the noise is sub-Poissonian. The energy dependence and quantum interference effects are not described by this approach. A simple extension allows to describe the presence of a barrier in addition to the disordered conductor and was modeled by de Jong and Beenakker [48]. As a function of the length of the disordered region the shot noise crosses over from a value dictated by the barrier transparency Γ ($0 \leq F \leq 2$) to the universal value of a diffusive conductor ($F = 2/3$) at lengths exceeding $\Gamma L/\ell \gtrsim 1.5$.

A first observation of shot noise doubling in diffusive NS contacts was made by Jehl et al. [53]. The shot noise was measured in a very short Cu bridge between a Cu and a Nb reservoir. The effective sample length was comparable to the elastic scattering length in the material and much smaller than the length scales of inelastic processes. The current noise was recorded with the SQUID resistance bridge method (see chapter 4) and a crossover between shot noise of slope $\frac{4}{3}$ for $eV < \Delta$ and the normal state value of $\frac{2}{3}$ above the gap was observed. Kozhevnikov et al. [54] measured the differential shot noise power in a diffusive gold wire attached to a Nb reservoir in a bias modulated scheme at microwave frequencies. The authors also report a 2/3-shot noise suppression. When an additional high-frequency excitation at frequency ν is applied during the measurement, sidebands at bias voltages $|V| = \frac{h\nu}{2e}$ form. This is a result of photon-assisted transport and an independent verification that the effective charge carrier of transport doubles, $q_{\text{eff}} = 2e$.

2.3.6 Energy dependence, coherence, and barriers in NS contacts with long diffusive wires

In our discussion of the scattering formalism we assumed fully coherent propagation of quasiparticles throughout the whole device. Further, we restricted the energy regime to a region where we can disregard the explicit energy dependence of the scattering amplitudes. This limits the range of validity of the results to short contacts and small energies.

Incoherent regime

Additional methods were developed for the study of NS contacts with long diffusive regions. The incoherent regime (i.e. wavefunction coherence does not extend along the whole diffusive region) was worked out by Nagaev [40] using classical Boltzmann transport equations and Langevin sources. Interestingly, he finds the same suppression factor of 2/3 as in the coherent regime. The method was later extendend to describe the crossover from the subgap regime to energies $eV > \Delta$ by Nagaev and Büttiker [50]. They derive the boundary condition for the symmetric part of the electron distribution function at the NS interface and assume no

energy transfer across the interface below the gap energy Δ. Next, they solve the diffusion equation to find the electron distribution function inside the normal metal wire which is used to define the local effective temperature, $T_N(\mathbf{r}) = \int \mathrm{d}\epsilon f(\epsilon, \mathbf{r})\,[1 - f(\epsilon, \mathbf{r})]$. The effective temperature enters the source term for the local fluctuation density and the total noise is obtained by integration along the wire [52], $S_I = \frac{4}{R}\int \frac{\mathrm{d}x}{L} T_N(x)$. The shot noise in the incoherent regime becomes

$$\begin{aligned} S_I &= \frac{4k_\mathrm{B}T}{R}\left\{\frac{2}{3} + \frac{1}{3}\frac{eV}{k_\mathrm{B}T}\coth\left(\frac{eV}{k_\mathrm{B}T}\right) + \frac{1}{6}\left[\tanh\left(\frac{\Delta + eV}{2k_\mathrm{B}T}\right) + \tanh\left(\frac{\Delta - eV}{2k_\mathrm{B}T}\right)\right.\right. \\ &- \left.\left. 2\tanh\left(\frac{\Delta}{2k_\mathrm{B}T}\right)\right] + \frac{1}{6}\left[\coth\left(\frac{eV}{2k_\mathrm{B}T}\right) - 2\coth\left(\frac{eV}{k_\mathrm{B}T}\right)\right]\ln\left[\frac{\exp(\frac{\Delta}{k_\mathrm{B}T}) + \exp(\frac{eV}{k_\mathrm{B}T})}{\exp(\frac{\Delta}{k_\mathrm{B}T}) - \exp(\frac{eV}{k_\mathrm{B}T})}\right]\right\}. \end{aligned} \tag{2.66}$$

Equation 2.66 was found in excellent agreement with the data of Jehl at al. [56].

Coherence and proximity effect in long wires

A microscopic extension to the method of Langevin sources for NS contacts was proposed by Houzet and Mineev [51]. They suggested an expression for the local spectral noise density in terms of the nonequilibrium electron distributions of the Keldysh-Usadel formalism and showed that for $eV,\ k_\mathrm{B}T \ll \Delta$ the shot noise is given by

$$S_I = \frac{8k_\mathrm{B}T}{3}\frac{\partial I}{\partial V} + \frac{4eI}{3}\coth\left(\frac{eV}{k_\mathrm{B}T}\right). \tag{2.67}$$

The formalism takes into account the proximity effect in the diffusive region. Surprisingly, this does not change the functional dependence of shot noise. It is sufficient to replace the normal state conductance by the dynamic conductance of the diffusive region. At low bias, the coherence effects lead to an enhancement in the shot noise, though it is found that the maximum enhancement does not occur at the same bias as the minimum in dynamic resistance of the device [51].

Full-counting statistics and interface barriers

An alternative route to calculating shot noise in the regime where the proximity effect is important is to use the full-counting statics method [58]. It introduces a counting field χ that couples to the current operator. The derivatives of the current with respect to χ generate all moments of the current distribution. In the Keldysh-Usadel formalism the counting field is introduced as a gauge transformation of the Green's function of one of the reservoirs. This approach was used by Belzig and Nazarov [57] in the framework of matrix circuit theory. They calculate an enhancement of the shot noise at energies of the order of the Thouless energy E_C of the wire which is due to the proximity effect. The maximum enhancement of $\approx 10\%$ occurs

around 4 E_C. At higher temperatures the Boltzmann-Langevin result is recovered.

Houzet and Pistolesi [59] extended the approach to NS contacts with an interface barrier. They treat the case of arbitrary interface transparencies $\{\Gamma_n\}$ and different ratios of boundary conductance, G_B, and wire conductance, G_D. By expanding the quasi-classical Green's function to first order in χ they obtain a set of differential equations which can be used to calculate the noise from a solution of the Usadel equations. In the incoherent regime an analytical expression for the Fano factor is found (all channels are assumed to have the same transparency Γ)

$$F = \frac{2}{3}\left[1 + \left(2 - 3\frac{\left\langle \frac{\Gamma^3}{(2-\Gamma)^4}\right\rangle}{\left\langle \frac{\Gamma}{(2-\Gamma)^2}\right\rangle}\right)\frac{G_D^3}{(G_D + 2G_B\left\langle \frac{\Gamma}{(2-\Gamma)^2}\right\rangle)^3}\right] . \tag{2.68}$$

In the coherent case the differential equations have to be solved numerically. Figure 2.14 shows the interesting case when boundary and wire resistance are the same. The conductance and Fano factor are displayed as a function of energy for different interface transparencies. For large $\Gamma \geq 0.8$ the Fano factor is roughly independent of energy and $\lesssim 2/3$. For smaller transparencies, however, there is a strong energy dependence with a steep increase around $\approx 5E_C$ corresponding to a crossover into the incoherent regime.

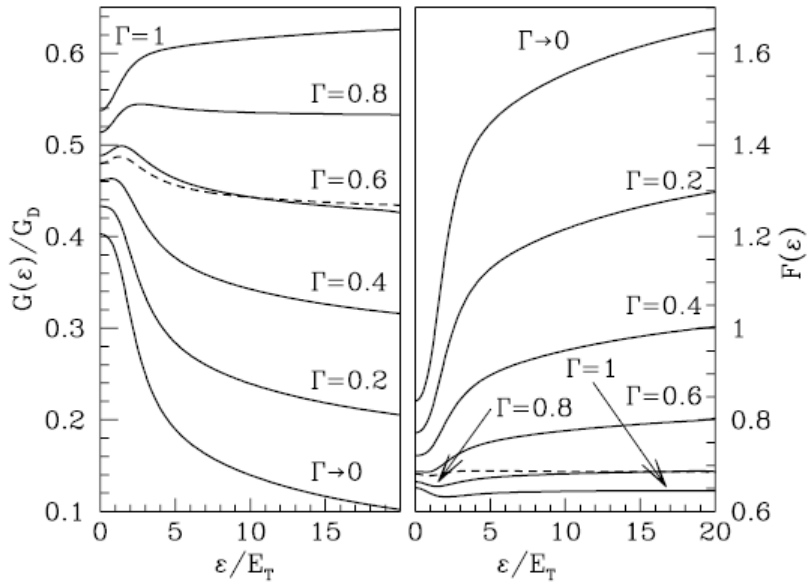

Figure 2.14: Conductance and Fano factor for $G_D = G_B$ and different interface transparencies Γ (from ref. [59]).

After this short review of theoretical concepts we will discuss the phenomenology of nonlocal transport in superconductors in the next chapter. Some of the first experimental evidence will be examined and some

promising recent results will be presented. Finally, theoretical predictions on nonlocal current correlations will be outlined that motivated this work.

Chapter 3

Nonlocal transport processes and current correlations

3.1 Introduction

The idea of probing the superconducting condensate using spatially separated contacts goes back to a *Gedankenexperiment* by Jeff Byers and Michael Flatté [65]. They envisioned investigating the anisotropy of the condensate wavefunction of a high-temperature superconductor with two closely-spaced STM tips and were the first to describe nonlocal transport between the two contacts. It was realized that electrons can tunnel from one STM tip to another or undergo a novel, nonlocal Andreev reflection process when the tip separation is similar to the coherence length in the superconductor.

The work of Guy Deutscher and Denis Feinberg [66, 67] pointed out that the use of anti-parallel spin-polarized ferromagnetic probes increases the probability for nonlocal Andreev transport and thus may result in a finite positive nonlocal conductance signal. They also coined the term *Crossed Andreev reflection* (CAR) for the nonlocal Andreev process and noted the coherent nature of the effect. Subsequently, many authors suggested to utilize the mechanism to create a solid-state entanglement device, or "Cooper-pair splitter." Mesoscopic beam splitters [72], coupled superconductor-quantum dot systems [73], and superconductor-carbon nanotube/Luttinger liquid systems [74, 75] were advocated as platforms for Cooper-pair splitters. Conceptually, quantum operations can be performed by using double-barrier quantum dot structures as energy-selective filters and by having ferromagnetic (or fully spin-polarized half-metallic) gates as polarization filters for spin. Progress toward the experimental implementation of tunable Cooper-pair splitter devices was made using superconductor-InAs quantum dot systems [68, 69] and a superconductor-carbon nanotube quantum dot [70] architecture.

Tests for wavefunction coherence and entanglement are based on current noise cross-correlation measurements [76, 74, 77, 78, 79] which have already been demonstrated experimentally, e.g. in the solid state equivalent of the Hanbury Brown and Twiss experiment in two-dimensional electron gases (2-DEGs) [80]. A first correlation experiment of nonlocal transport in normal metal-superconductor hybrid-tunneling devices

was carried out by Wei and Chandrasekhar [81]. It suggested that positive or negative current correlations were induced for different biasing conditions. This was an important first demonstration that Cooper-pair splitting may be a feasible way of creating entangled electron pairs.

This chapter is intended to introduce the basic phenomenology of nonlocal transport in superconductors. We will start with a discussion of the theoretical concepts of crossed Andreev reflection (CAR) and elastic co-tunneling (EC), followed by an overview of the early experimental evidence for the existence of nonlocal transport in hybrid devices with ferromagnetic and normal metal contacts. The observation of finite nonlocal conductance in NSN-type devices was not expected in simple phenomenological models where CAR and EC contributions are supposed to cancel exactly as we will show below. Evidence for coherent nonlocal transport was also found in NSN tunnel devices by manipulating the coherent states with an applied magnetic field and in the already mentioned Cooper-pair splitter experiments.

For the implementation of entanglement devices it is of great importance to understand the mechanism which leads to finite nonlocal transport in devices without spin-polarized electrodes. Theoretical studies offer several explanations. Non-perturbative theories and numerical calculations go beyond the first-order approximation which was used in the early theoretical work based on CAR- and EC-processes alone. They concur with experimental findings in their prediction of finite, negative (or 'EC-like') cross-conductance. Similarly, when higher-order coherent terms are considered in nonlocal transport calculations, a finite negative cross-conductance is recovered. I will present a small overview of theoretical work on this problem at the end of this chapter. Alternative scenarios were developed to describe some of the earlier experimental observations. Asymmetric coupling of EC and CAR modes to external electromagnetic radiation was shown to break the symmetry between the two processes and may explain the results by Russo et al. [87]. The nonlocal resistance data of NSN tunneling devices by Kleine et al. [88] was interpreted in terms of dynamic Coulomb blockade by Levy-Yeyati et al. [89]. However, an increasing amount of experimental evidence points toward the importance of higher-order transport processes in NSN-type devices.

Naturally, the role of coherent higher-order processes is best studied in devices with transparent interfaces. Theoretical predictions find a enhancement of current correlations in this case. For perfectly transmissive interfaces a strong positive correlation signal is expected. A first attempt to resolve such correlations was made by Kaviraj et al. [63] as will be reviewed below.

Positive current correlations are created either by CAR in the limit $T \ll 1$ or by CAR-like higher-order processes in the regime $T \simeq 1$. In most situations standard fabrication methods will produce samples

with interface transmissions in the intermediate regime. In this crossover regime theory predicts negative correlations and a characteristic symmetric bias dependence. In our experimental setup we are able to bias both contacts of our NSN devices independently. Therefore, we are in a position to map out the bias dependence of current correlations for arbitrary biasing conditions at the contacts and may look for signatures of nonlocal higher-order transport. We shall conclude this chapter with an overview of the theoretical predictions for current correlations in the various limits of interface transparency. Our experimental results will be presented in Chapter 5.

3.2 Crossed Andreev reflection and Elastic Co-tunneling

3.2.1 Phenomenology

When current is passed from a normal metal into a superconductor a fraction of it is converted into supercurrent in the interface region. Any residual charge enters the superconductor as nonequilibrium charge Q^* but at low bias voltages and low temperatures this contribution is negligible. The current conversion process is called *Andreev reflection* and was described in detail in Chapter 2. In the interface region the electron wavefunction penetrates as an evanescent wave into the superconductor. The penetration depth is similar to the coherence length, ξ_S. Under the influence of the pairing interaction in the superconductor the electron may form a Cooper pair with another electron of opposite spin. Thus a hole state of opposite spin must be retro-reflected into the normal metal electrode such that charge, energy and momentum are conserved (see Fig.3.1(a)). When several normal metal electrodes are attached to the superconductor within a distance $d \lesssim \xi_S$, a finite probability exists for the hole quasiparticle to be reflected into a different electrode instead of the one from which the electron originated (Fig. 3.1(c)). This nonlocal or "Crossed" Andreev reflection (CAR) was first discussed by Deutscher and Feinberg [66]. Naturally, the electron may also tunnel between two electrodes through the energetically forbidden region in the superconductor (Fig. 3.1(d)). This process is called Elastic Co-tunneling (EC) after an identical effect known in quantum dot systems.

Distance dependence

Crossed Andreev reflection and elastic co-tunneling correspond to the lowest order non-vanishing matrix elements in a perturbation expansion of nonlocal transport. The relevant diagrams are shown in Fig. 3.2(c+d). For now let us disregard the proximity effect in the normal metal wire and focus on the phenomenological aspects of CAR and EC. We want to calculate the nonlocal conductance associated with CAR and EC transport. The expressions are proportional to the conductances for transport of single electrons across the inter-

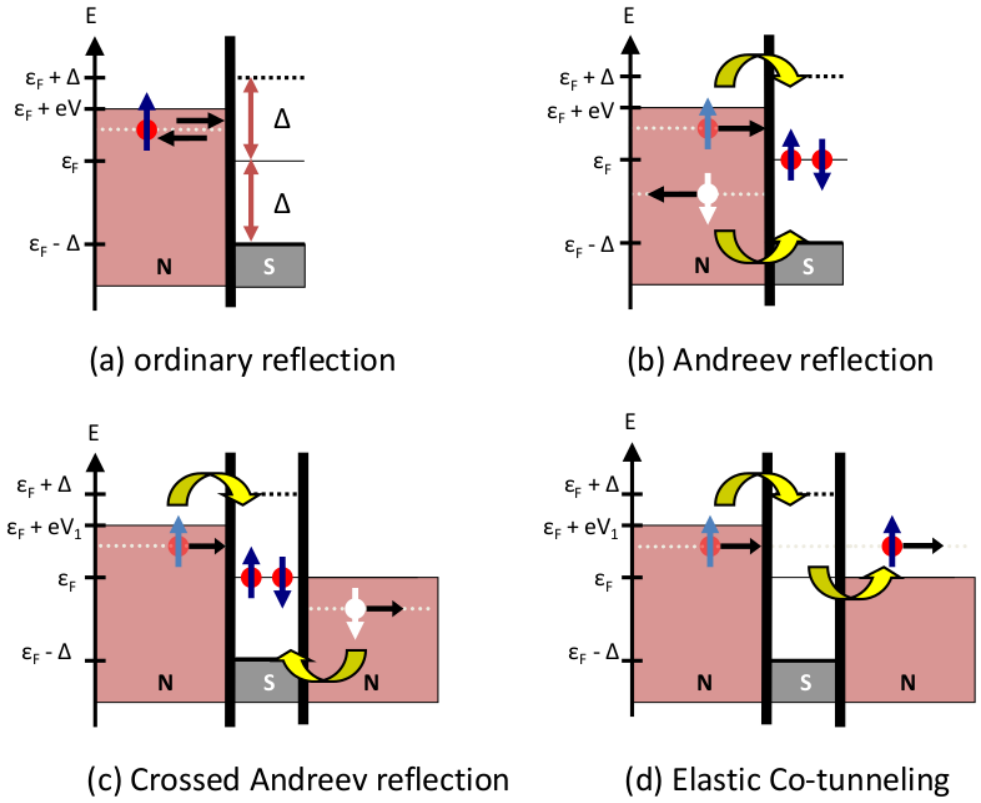

Figure 3.1: Schematic representation of ordinary reflection (a), Andreev reflection (b), Crossed Andreev reflection (c), and elastic Co-tunneling (d). Occupied states are represented by filled areas. No quasiparticle states are available within the energy gap of the superconductor.

face barriers which are given by $G_i^\sigma \approx 2G_Q N_i^\sigma(0) N_S(0) |T_i|^2 \frac{\mathcal{S}}{k_i^\sigma k_S} \mathcal{F}(k_S, k_i^\sigma, w_i)$ [82], where $N_i^\pm(0) = N_i(\mp\mu h)$ is the density of states at the Fermi energy in the normal metal. In ferromagnetic materials the spin-dependent density of states in the presence of the exchange field h is taken into account by shifting the energies of the spin-bands by $\pm\mu h$. Here μ is the effective magnetic moment. The conductance quantum is given by $G_Q = 2e^2/h$; further, $N_S(0)$ in the density of states at the Fermi energy of the superconductor in the normal state, T_i the tunneling matrix element, k_i^σ and k_S are the magnitudes of the Fermi wavevectors of normal metal and superconductor, respectively. The geometry of the contacts is captured by the contact area $\mathcal{S}$ and a shape-dependent factor $\mathcal{F}$ of order unity.

The expressions for the conductances of individual contacts i, $i = (1,\ 2)$, and of the contributions from CAR and EC can be read off directly form the diagrams in Fig. 3.2. We find, $G^i \propto G_i^\uparrow G_i^\downarrow$ whereas the nonlocal conductances $G^{EC(CAR)} \propto \sum_\sigma G_1^\sigma G_2^{\uparrow(\downarrow)}$. The probability factors for EC (CAR) depend on the

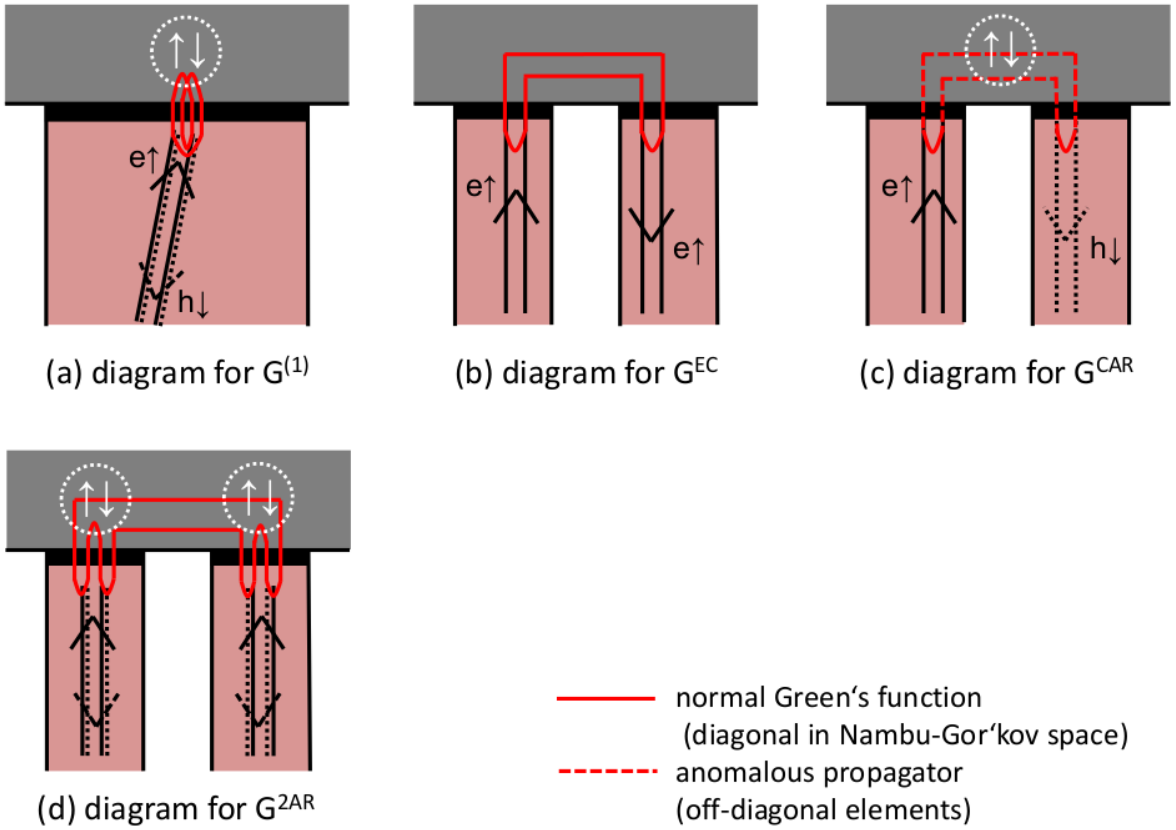

Figure 3.2: Diagrams for the perturbation expansion of nonlocal transport: Local Andreev reflection can be represented by a graph which involves quasiparticle tunneling at a single contact (a), whereas the CAR (b) and EC processes (c) couple the tunneling matrix elements of different contacts. The (distance-dependent) probabilities for nonlocal tunneling are calculated from the ordinary (solid) and anomalous (dashed) quantum mechanical propagators in the superconductor. A higher-order process may include (multiple) Andreev reflection events at an individual contact. The graph for double Andreev reflection is shown in (d).

contact separation d through the distance dependence of the normal (anomalous) propagators, i.e. the advanced and retarded Green's functions which connect the in- and outgoing wave states. In the ballistic limit the propagators are calculated using plane-wave states. The dirty-limit expressions are diffusion-averaged quantities. For $d \gg \xi$ we intuitively expect the amplitudes to fall off exponentially $\sim \exp(-d/\xi)$. A more careful derivation [82, 83] for contacts with small diameters, $w_1, w_2 < \xi$, reveals:

$$G^{CAR} \approx \frac{1}{4G_Q}\left[\sum_\sigma \mathcal{F}_1^\sigma G_1^\sigma \mathcal{F}_2^{-\sigma} G_2^{-\sigma}\right]\lambda(d)\ , \tag{3.1}$$

$$G^{EC} \approx \frac{1}{4G_Q}\left[\sum_\sigma \mathcal{F}_1^\sigma G_1^\sigma \mathcal{F}_2^\sigma G_2^\sigma\right]\lambda(d)\ . \tag{3.2}$$

The dependence on the contact separation is:

$$\lambda(d) = \frac{\exp(-2d/\pi\xi)}{(k_S d)^2} \qquad \text{ballistic transport,} \tag{3.3}$$

$$\lambda(d) = \frac{\exp(-d/\xi_d)}{\hbar N_S(0) D d} \qquad \text{diffusive transport}(\xi_d \approx \sqrt{\ell\xi}) \ . \tag{3.4}$$

In the above formula ℓ, ξ_d, and D are the mean free path in the superconductor, the dirty-limit coherence length, and the diffusion constant, respectively. As in the case of the conductances for transport across the barriers, geometry factors $\mathcal{F}_i^\sigma$ have been introduced which take into account interference effects between different parts of the contacts. Equivalently, one can perform averaging over electron phases of different channels [84]. It should be noted that for small $d \lesssim \xi$ the behavior of $\lambda(d)$ is dominated by the prefactor rather than the exponential. Therefore the cross-conductances are expected to be larger for dirty-limit superconductors although the dirty-limit coherence length is also smaller in this case.

Let us now take a look at the full subgap conductance matrix:

$$\begin{pmatrix} I_1 \\ I_2 \end{pmatrix} = \begin{pmatrix} G^{(1)} + G^{CAR} + G^{EC} & G^{CAR} - G^{EC} \\ G^{CAR} - G^{EC} & G^{(2)} + G^{CAR} + G^{EC} \end{pmatrix} \begin{pmatrix} V_1 \\ V_2 \end{pmatrix} \ , \tag{3.5}$$

The negative sign of G^{EC} is a consequence of the outgoing reflected state carrying negative charge. Rewriting equations (3.1) and (3.2) in terms of the spin polarizations $P_i = \frac{N_i^\sigma - N_i^{-\sigma}}{N_i^\sigma + N_i^{-\sigma}}$, $i = 1, 2$, we find $G^{CAR} \propto (1 - P_1 P_2)$ and $G^{EC} \propto (1 + P_1 P_2)$, hence the off-diagonal elements in the conductance matrix, which are proportional to $-P_1 P_2$, should vanish for unpolarized normal metals. This is the previously mentioned cancellation of CAR and EC.

Within the same theoretical framework nonlocal current fluctuations in three-terminal device geometry can be quantified. The calculation was carried out by Bignon et al. [86] in the limit of $|eV_1|,\ |eV_2|, k_\mathrm{B}T \ll \Delta$. They obtained,

$$S_{12} = 2e \left[(V_1 + V_2) \coth\left(\frac{e(V_1 + V_2)}{2k_\mathrm{B}T}\right) G^{CAR} - (V_1 - V_2) \coth\left(\frac{e(V_1 - V_2)}{2k_\mathrm{B}T}\right) G^{EC} \right]. \tag{3.6}$$

Surprisingly, the result does not depend on the conductances of the individual contacts, G^i, and the contributions of CAR and EC are of the same magnitude.

3.3 Previous experimental work

Shortly after the prediction of crossed Andreev reflection by Deutscher and Feinberg, Beckmann et al. [6] conducted an experiment in which several ferromagnetic probes were placed on an aluminum wire. The contact separations were only a few 100 nm, approximately the distance of the superconducting coherence length in the material, see Fig.3.3(a). The structure formed a lateral spin-valve in which shape anisotropy fixed the magnetization direction along the wire axes of the ferromagnetic wires. The coercive field differed for individual wires because of dissimilar wire widths. Thus the orientation of the magnetization could be adjusted for each wire separately.

The nonlocal resistance signal was measured with a small excitation current as the sample was cooled below the superconducting transition of aluminum, see Fig. 3.3(b). The measurement configuration for a nonlocal resistance measurement is indicated in Fig. 3.3(a). Just below the transition a large charge imbalance peak was observed. A small difference in nonlocal resistance between parallel and anti-parallel magnetization existed in the normal state and below the superconducting transition. In the normal state the nonlocal resistance difference is due to the spin-valve effect [90]. The inset shows the spin-valve signal in the normal state as the relative magnetization direction between the wires was switched by an applied magnetic field. A different scaling behavior was found for the nonlocal resistance in the superconducting state when compared to the normal state, see Fig. 3.3(c). In the superconducting state the nonlocal resistance difference decays on a scale comparable to the coherence length. An absolute negative nonlocal resistance, as predicted for pure CAR, was not observed for the anti-parallel magnetization configuration. Due to the large background signal, it is not clear how CAR or EC can be distinguished from spin-imbalance effects which have a typical decay length comparable to the coherence length in the aluminum superconductor [138].

A conceptually similar experiment was carried out by Cadden-Zimansky and Chandrasekhar [5]. Instead of ferromagnetic contacts they attached several closely-spaced normal metal wires to an aluminum wire, see Fig. 3.4 (a). This resulted in a strong inverse proximity effect in the superconductor. As the sample was cooled down, a broad charge imbalance feature appeared below the suppressed transition temperature $T_c \approx 600$ mK. Whereas no nonlocal signal was measured above the transition, a large nonlocal resistance was measured down to the lowest temperatures for closely-spaced contacts (Fig. 3.4 (b)). In a separate experiment an additional dc current bias was applied and nonlocal differential resistance was measured all the way through the current-induced transition of the superconducting wire (Fig. 3.4 (c)). The zero-bias nonlocal resistance and the peak-height of the charge imbalance peak at the transition are found to

scale differently with contact separation (Fig. 3.4 (d)). The first decays exponentially with the estimated superconducting coherence length whereas the latter can be fit using the predicted functional form for charge imbalance recombination [91, 92], $R \propto (1-\tanh(x/\Lambda_{Q^*})$, with $\Lambda_{Q^*} \approx 1.1\ \mu$m. The distance dependence of the zero-bias nonlocal resistance fits expectations for CAR- and EC-like nonlocal transport. A later theoretical discussion [94] showed that the exponential decay of the zero-bias nonlocal resistance is also expected in non-perturbative models of nonlocal transport in NSN structures. The model was also able to predict the temperature at which the charge imbalance peak occurred in the data. In another version of the experiment Cadden-Zimansky and Chandrasekhar incorporated the injecting contact for the nonlocal measurement as normal metal branch into an Andreev interferometer [98, 97] and demonstrated how phase-coherent

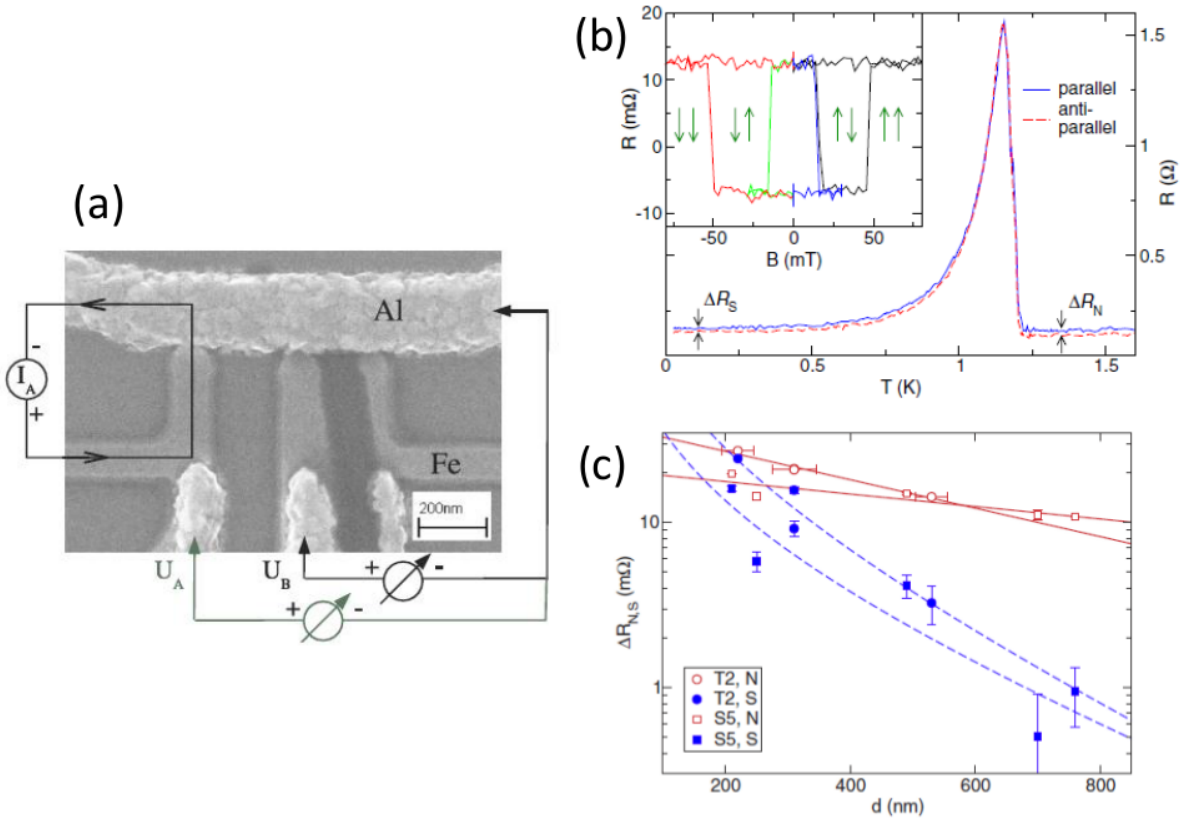

Figure 3.3: The nonlocal transport experiment by Beckmann et al. (from ref. [6]): Transport measurements in Fe-Al spin-valve structures (a) reveal a difference in nonlocal resistance between the two relative magnetic polarization states of the contacts in normal and superconducting state of the aluminum wire (b). A spin-valve effect is observed in the normal state, see inset in (b). The dependence of the nonlocal signal on contact separation is different in the superconducting state and scales with the coherence length as expected for CAR.

manipulation of the quasiparticle distribution in the injector contact reflects in the nonlocal resistance signal.

Several experiments were designed to study nonlocal transport in NSN structures with tunnel barriers of different interface transmission (and barrier quality) [99, 88, 71]. For the experiment by Brauer et al. [71], see Fig. 3.5, two closely-spaced copper-aluminum tunnel junctions were carefully prepared using the shadow-evaporation technique. The contact spacing was similar to the coherence length in the aluminum. At low voltage bias the contacts showed a zero-bias anomaly which was mirrored in the nonlocal conductance. The

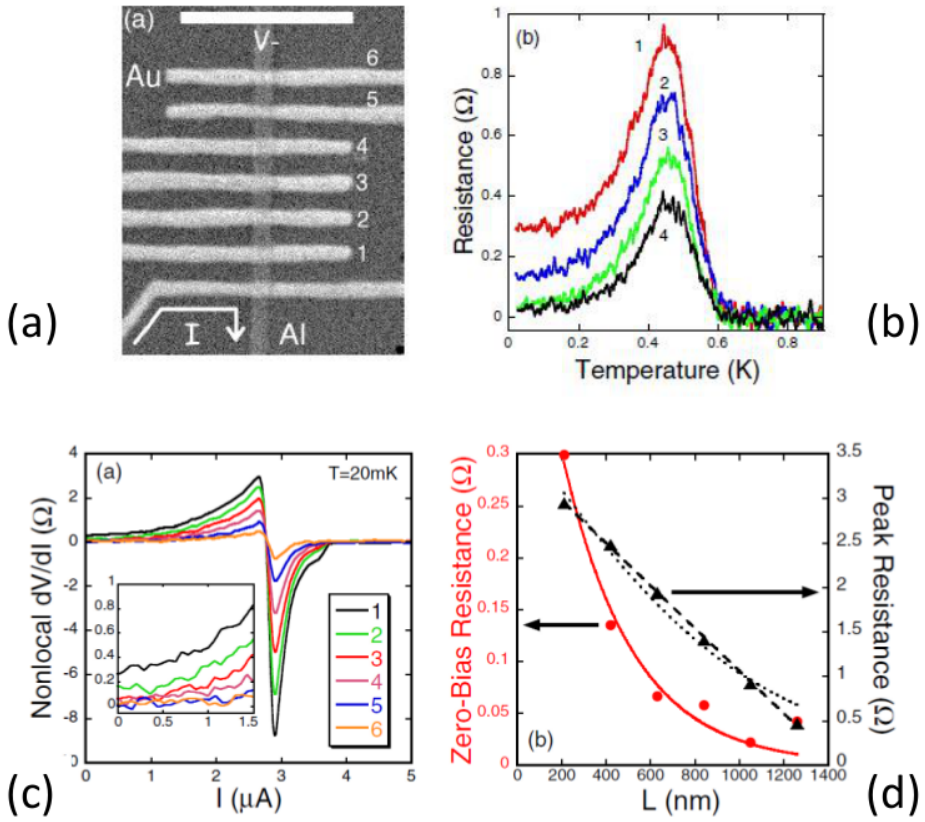

Figure 3.4: Distance and bias dependence of nonlocal resistance in a NSN wire structure by Cadden-Zimansky and Chandrasekhar (from ref. [5]): Multiple normal metal leads are contacting a superconducting wire (a). Upon cooling below the transition the nonlocal resistance shows a large charge imbalance peak and flattens out a finite value (b). The differential nonlocal resistance has peak dip structure when the superconductor is driven normal with bias current (c). Zero-bias nonlocal resistance and peak-height at the transition exhibit a different dependence of contact separation (d). Whereas the zero-bias value decays exponentially and thus is attributed to CAR- and EC-like transport, the peak values decrease with a longer length scale which is consistent with charge imbalance.

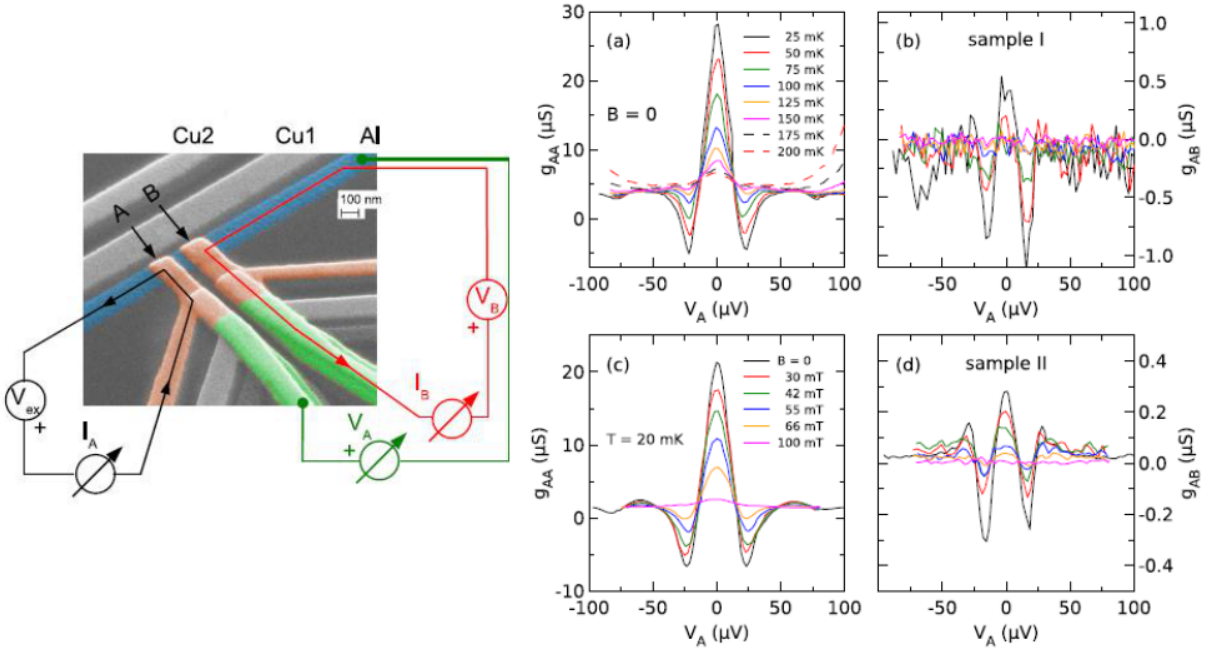

Figure 3.5: The nonlocal conductance measurements of Brauer et al. (from ref. [71]): A zero-bias anomaly is observed in the conductance of the injecting contact and a similar feature is found in the nonlocal conductance at the detector contact. The features are attributed a phase-coherent enhancement of Andreev reflection at the tunnel barriers. Different phase-coherent mechanisms are proposed to account for the presence of multiple maxima and minima in the conductance. Phase-coherence in demonstrated by modulating the signal with a small magnetic field (not shown).

origin of the zero-bias anomaly was attributed to phase-coherent enhancement of Andreev reflection (reflectionless tunneling) [100, 101]. Other models were suggested to account for the regions of negative differential resistance and several side-peaks, e.g. phase-diffusion in a Josephson junction (the other superconducting electrode is formed by the aluminum shadow on the copper lead) or ballistic scattering in the contact region. By applying a small magnetic field in perpendicular direction, the nonlocal transport can be modulated. Offset and shift of the nonlocal conductance pattern were studied as a function of contact bias and scaled with the square of the amplitude of the subgap anomaly in the local conductance as predicted by Ref. [94]. However, the overall magnitude of the nonlocal conductance was larger by three orders of magnitude. The experiment demonstrates the importance of phase-coherence for nonlocal transport.

Current correlations in NSN tunnel devices were studied by Wei and Chandrasekhar [81]. They measured the cross spectral density of voltage fluctuations in current biased three-terminal copper-aluminum NSN tunnel devices, see Fig. 3.6. The strong conductance enhancement due to the disorder induced zero-bias

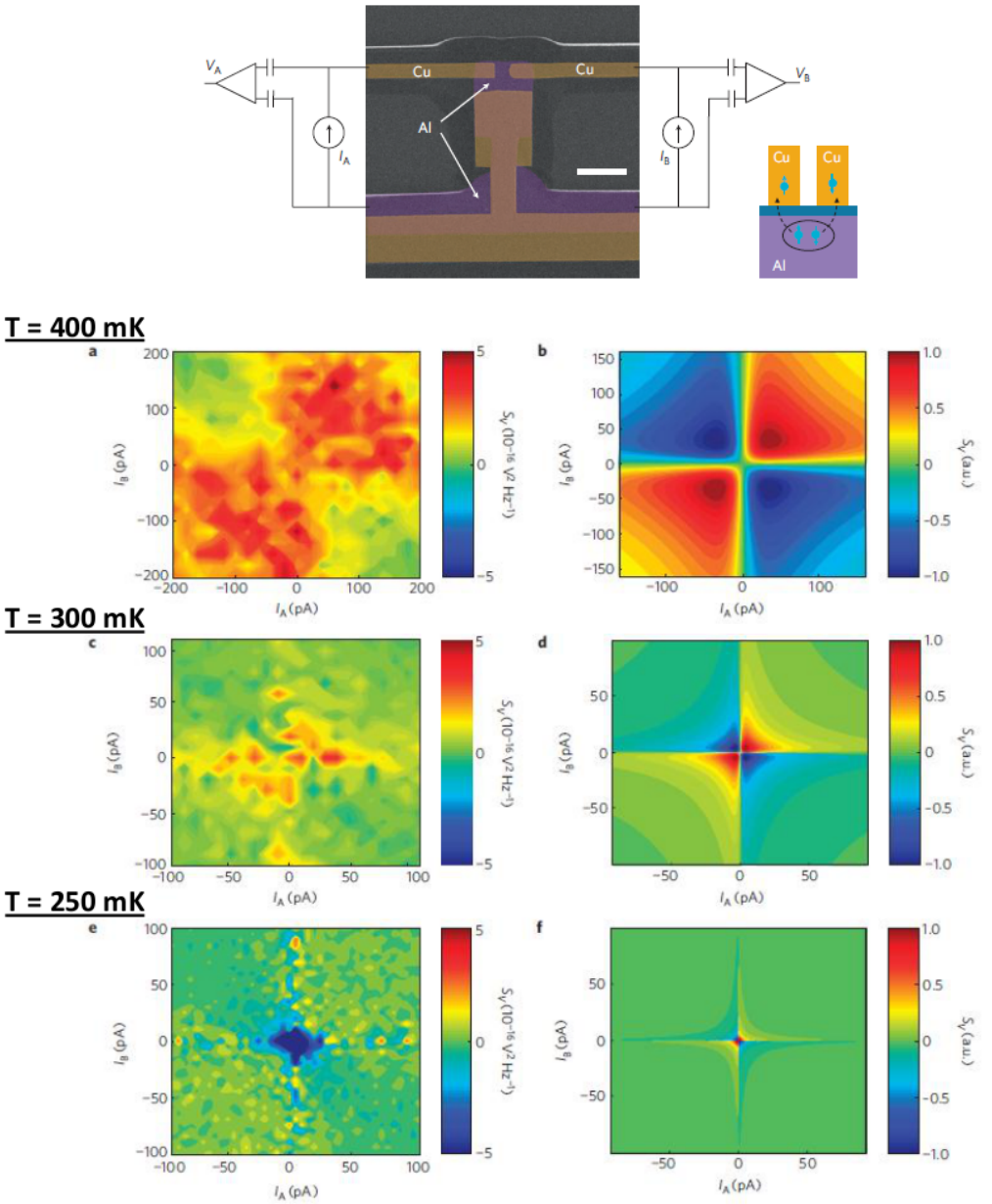

Figure 3.6: The current correlation experiment of Wei and Chandrasekhar (from ref. [81]): A measurement of voltage fluctuations in a current biased three-terminal Cu-Al tunnel junction device. Current fluctuations scale with dynamical resistance of the tunnel junction which exhibits a strong zero-bias anomaly due to the coherent enhancement of Andreev reflections in the presence of disorder at the tunnel interface and thus allows to resolve a signal. A prediction of the current correlations is plotted on the right-hand side and the data on the left. Positive, CAR-like correlations dominate.

anomaly at the tunneling contacts allowed them to resolve correlated current fluctuations in their device. Voltage noise was converted in current noise using the dynamical resistance of the biased contacts in a semiconductor model. Predominately positive, CAR-like correlations were observed. At higher temperature qualitative agreement with Eqn. 3.6 was found but without the predicted symmetry between CAR and EC, $G^{CAR} \neq G^{EC}$. The predicted current correlation signal is shown on the right-hand side of Fig. 3.6 and the data on the left. As pointed out by the authors quasiparticle tunneling at finite temperatures may contribute to the signal and may cause the discrepancy between model and data.

Another current correlation experiment was performed by Kaviraj et al. [63]. A mesoscopic structure of two Cu-Al SNS Josephson junctions was fabricated which form a SNSNS device with transparent interfaces. The two SNS junctions were biased in parallel configuration and the current noise in each branch was measured with separate SQUID devices (Fig. 3.7(a)). When the SNS junctions are biased into the voltage state Incoherent Multiple Andreev reflections (IMAR) occur in both junctions. Electron and hole quasiparticles traverse the junction several times undergoing Andreev reflection at the junction boundaries. Each time a quasiparticle travels across the junction it increases its energy by an amount $|eV|$ due to the voltage drop across the junction. Eventually, it reaches an allowed quasiparticle state in one of the superconducting electrodes and escapes. Contrary to expectations for NSN transport in devices with transparent interfaces, a negative current correlation signal is measured for the SNSNS device in the whole bias range, see Fig. 3.7(b). This was interpreted as partition noise of quasiparticles which are injected above the gap by the IMAR process and therefore have a fermionic characteristic with negative correlations and thus unrelated to nonlocal subgap

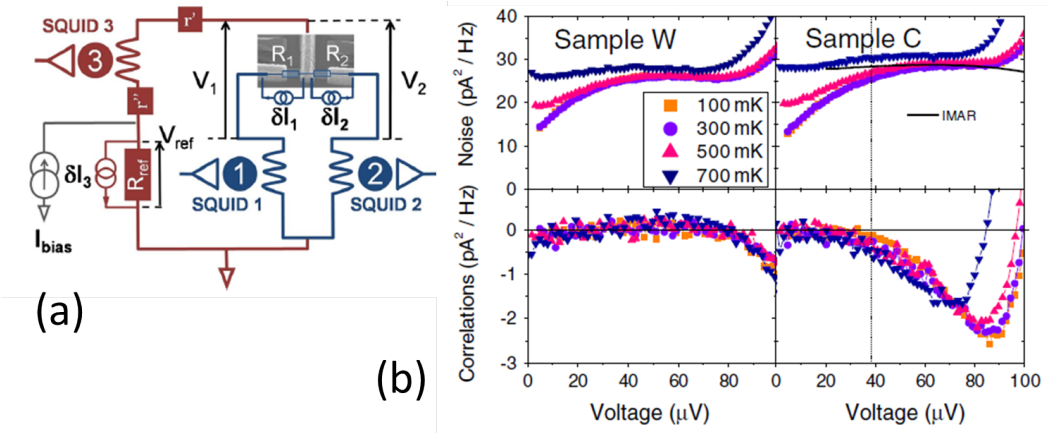

Figure 3.7: Current correlation measurement of Kaviraj et al. (from ref. [63]): Two mesoscopic SNS Josephson junctions that form a SNSNS device are measured in parallel (a). Both SNS junctions are biased in the voltage state and current noise due to incoherent Multiple Andreev reflections (IMAR) is observed (b). The current correlation signal is negative over the whole bias range contrary to expectations for NSN devices with highly transparent interfaces.

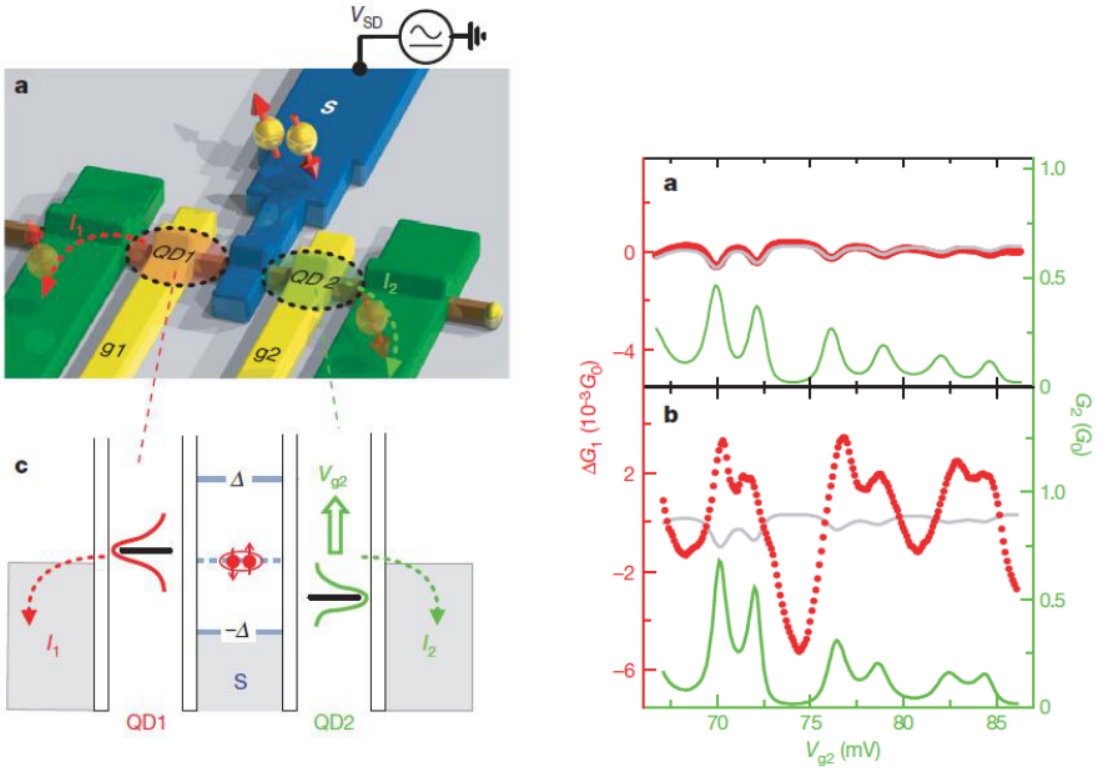

Figure 3.8: The Cooper-pair splitter experiment by Hofstetter et al. (from ref. [68]): Two InAs quantum dots (QD1 and QD2) are coupled to a mesoscopic superconductor (left (a)). The energy levels of the quantum dots can be tuned on and off resonance with the chemical potential of the superconductor (left (c)). On resonance Cooper pairs can tunnel through the quantum dot and the conductance shows a maximum. The change in conductance of QD1 (red) and in the conductance of QD2 (green) is plotted as the gate voltage at QD2 is swept (same as energy level diagram on the left): When a magnetic field suppresses superconductivity (right (a)) the conductance curve of QD1 is the same as in the normal state (grey). In the superconducting state (right (b)) the change in cross conductance scales with the conductance of QD2.

transport.

Most recently, progress toward tunable Cooper-pair splitting was made in the experiments by Hofstetter et al. [68] on superconductor-InAs quantum dot devices, see Fig. 3.8 (left), and by De Franceschi et al. [70] using a carbon nanotube-quantum dot based architecture. In the experiment by Hofstetter et al. the applied gate voltages allowed to bring the energy levels of the quantum dots in and out of resonance with the chemical potential of the superconductor. On resonance Cooper pairs were able to tunnel through the dot and the local conductance showed a maximum. By leaving one of the quantum dots (QD1) on resonance ("detector") and sweeping the gate of the other dot (QD2), the change in nonlocal conductance was mapped out (red

line), see Fig. 3.8 (right). Although 3 orders of magnitude smaller in magnitude, the signal clearly modulated with the conductance of QD2 (green line). In comparison, when superconductivity was suppressed, a signal much smaller in magnitude (gray line) was measured at QD1. The same signal was measured above the transition temperature of the superconductor.

In a follow up experiment [69] finite bias was applied across the quantum dots. Cooper-pair splitting (CPS) was found to be the dominant nonlocal process on resonance whereas off-resonance CPS and EC contributions were of similar magnitude. This was attributed to the energy dependent effective density of states for quasiparticles in the InAs nanowire.

3.4 Non-perturbative calculations and higher-order coherent processes

3.4.1 Finite nonlocal conductance

Historically, Deutscher and Feinberg devised crossed Andreev reflection and elastic co-tunneling processes in a simple BTK-model [66, 67]. First explicit calculations of the distance dependence of nonlocal conductance were implemented using the tunneling Hamiltonian formalism [82, 86, 84, 83], which I presented earlier. Only the lowest-order in perturbation theory was considered, for which nonlocal transport is carried by CAR and EC processes. The finite nonlocal conductance we saw in the experiments on NSN and Cooper-pair splitter devices cannot be explained satisfactory using either approach. Without an explicit breaking of symmetry, e.g. by introducing the spin-dependent density states of ferromagnetic electrodes into the problem or coupling the device to electrical modes of the environment, CAR and EC will cancel exactly. The cancellation is lifted by introducing higher-order terms and weak localization at the interfaces into the perturbation expansion of nonlocal transport [84, 102, 103]. An example of such a higher-order graph is shown in Fig. 3.2(d). Coherent nonlocal processes couple Andreev reflection events at both interfaces. Consequently, at high interface transparencies we may expect current correlations to behave qualitatively different from the CAR and EC prediction by Bignon et al., Eqn. 3.6. We will discuss predictions in the next section.

The theoretical framework of the Keldysh-Usadel equations can be used to describe nonlocal transport in diffusive conductors [104, 105, 94]. This allows to address directly the interplay between CAR and nonlocal charge imbalance. The conductance enhancement due to electron interference in the normal metal

and the broadening of the density of states in the superconductor can be calculated from the solutions of the (linearized) Keldysh-Usadel equations. The method is non-perturbative and leads to finite positive nonlocal conductance. The predictions for nonlocal charge imbalance are in agreement with the data by Cadden-Zimansky and Chandrasekhar [5].

3.4.2 Current correlations in NSN structures

As was already mentioned, including higher-order processes in the perturbation expansion introduces correlations between Andreev reflection events localized at the two interfaces. One may intuitively expect a strong enhancement in the current correlations between the two contacts. Such a behavior was first reported in theoretical studies by Mélin et al. [106]. They performed a non-perturbative, single channel BTK-model calculation using the noise correlation formula by Anantram and Datta [137]. Their main observation was a crossover between positive correlations at high barrier transparencies, to predominantly negative correlations for intermediate transparencies (Fig. 3.9(a)). In the tunneling limit the result by Bignon et al. [86], Eqn.3.6, is reproduced.

For a perfectly transparent interface ($T_N \simeq 1$) correlations are always positive. They are caused by higher-order diagrammatic contributions to nonlocal transport in which an electron quasiparticle in one electrode is converted into a hole quasiparticle in the other electrode and *vice versa*. In the process a Cooper pair

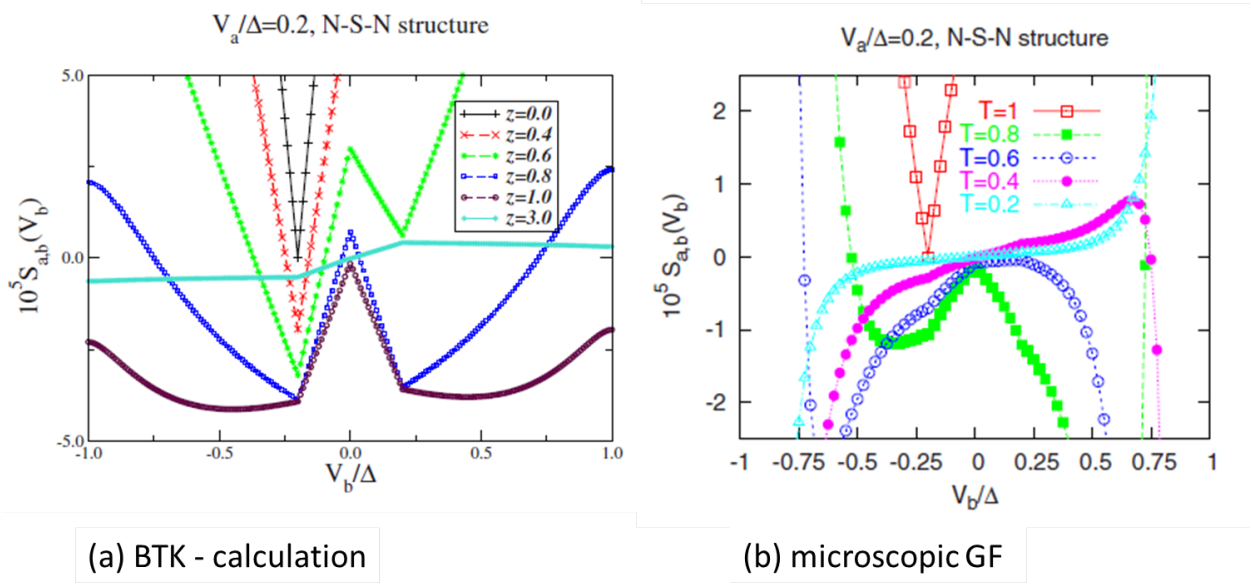

Figure 3.9: Current correlations calculation using a BTK model (a) and microscopic Green's functions (b). The calculations were carried out for a distance $d/\xi_S = 4.6$ between the contact interfaces. From ref. [106].

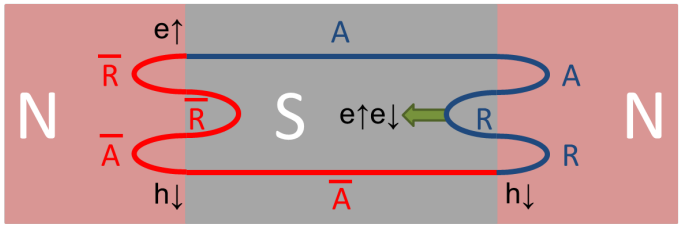

Figure 3.10: Schematic representation of a positive contribution to current cross-correlations: An electron quasiparticle from the left electrode is transmitted to the right electrode where it is converted in to a hole quasiparticle and a Cooper pair is ejected into the superconductor (blue line). The diagram is completed by the time-reversed process (red line). The Cooper-pair state on the left-hand side is not shown. Propagation forward in time is marked by A and R for advanced and retarded Green's functions. $\overline{A}$ and $\overline{R}$ represent the time-reversed Green's functions.

is created at one of the interfaces (Andreev reflection, AR) and a hole pair at the opposite interface (anti-Andreev reflection, $\overline{\mathrm{AR}}$) [107]. The positive correlation comes from the exchange of a fermion in the process. The strength of the correlations varies with the available density of states for electron quasiparticles in one electrode and hole quasiparticles in the other electrode. This dependence is the same as for crossed Andreev reflection thus we call the process 'CAR-like.' Assuming the quasiparticles distribution in the electrodes is given by a Fermi distribution with chemical potential $\mu_i = eV_i$, the correlations show a minimum at $V_1 = -V_2$ (compare the diagram in Fig. 3.2(c)). A schematic diagram for one of the contributing processes is shown in Fig. 3.10.

At intermediate interface transparencies, $T \simeq \frac{1}{2}$, higher-order processes are suppressed (e.g. the probability for the AR$-\overline{\mathrm{AR}}$ process in Fig. 3.10 is proportional to T^8). Negative contributions to the current correlations dominate. Positive contributions arise from processes with 'CAR-like' and 'EC-like' dependence on the quasiparticle density of states in the electrodes. Assuming the contacts have the same transparency, both types of processes contribute with similar magnitude and the current correlations have a 'W-shape' with two minima. The first minimum at $V_1 = -V_2$ corresponds to the suppression of processes with 'CAR-like' dependence on the density of states and the second minimum at $V_1 = V_2$ to the suppression of 'EC-like' processes. In the tunneling limit the result by Bignon et al. [86] is recovered in which positive correlations are related to CAR processes and negative correlations to EC. Microscopic Green's functions calculations by the same authors show qualitatively similar results in the three transparency regimes discussed above (see Fig. 3.9(b)).

The path-integral formalism of quantum field theory provides another, conceptually different way of incorporating perturbations to all orders into nonlocal transport calculations. Under certain simplifying as-

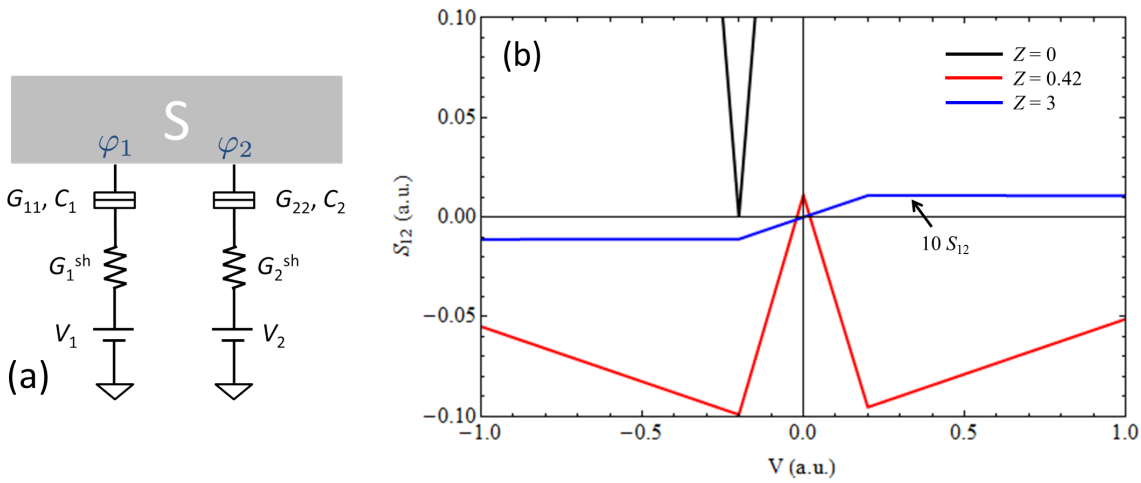

Figure 3.11: Calculation of current calculations for NSN devices with different barrier strength, Z: Golubev et al. [95] calculated the noise in a NSN device using the equivalent circuit in (a). The Langevin sources in the Langevin equations for (a) are derived from the effective action of a path-integral formulation of nonlocal transport in the device. Results of eqn. 3.7 are plotted for different barrier strengths Z at temperature $T = 0$ (b). In the plot the cross spectral density S_{12} has arbitrary units and the distance-dependent factor in the nonlocal conductance G_{12} is set to unity.

sumptions, Golubev et al. [95] were able to derive an effective action for the path-integral in terms of the superconducting phases φ_r at the two interfaces $r = (1, 2)$ of a NSN device. They assume barriers with transmissions T_r. The voltage drops in the circuit branches formed by the tunnel barrier of conductance G_{rr} and capacitance C_r and the shunt resistor of conductance G_r^{sh} which represents the impedance of the external circuit, see Fig. 3.11(a). The pairing potential of the superconductor is assumed to be much larger than the other characteristic energy scales, $|eV_r|, k_BT \ll \Delta$.

The action is composed of quadratic forms in the phase difference variables φ_r^- between forward and backward branch of the Keldysh contour. The shot noise is calculated from the Langevin equations for the circuit in Fig. 3.11(a). The source terms for the shot noise at the NS barriers can then be read off from the quadratic forms. The presence of the external circuit introduces electron-electron interactions which can be disregarded by taking the limit $1/G_r^{sh} \to 0$. In this case, a simple expression for the nonlocal current correlations in the NSN device is found,

$$\begin{aligned} S_{12} &= -2G_{12}(2-\beta_1-\beta_2)W(\omega,0) - 2G_{12}\beta_1 W(\omega,2V_1) - 2G_{12}\beta_2 W(\omega,2V_2) + \\ &+ G_{12}\gamma_+ W(\omega, V_1+V_2) - \\ &- G_{12}\gamma_- W(\omega, V_1-V_2), \end{aligned} \tag{3.7}$$

where

$$W(\omega, V) = \frac{1}{2} \sum_{\pm} (\omega \pm eV) \coth \frac{\omega \pm eV}{2k_{\mathrm{B}}T}.$$

The transparency dependent factors are

$$\beta_r = 1 - \tau_r, \tag{3.8}$$

$$\gamma_{\pm} = \pm 1 + \frac{(1 - 2\tau_1 - 2\tau_2 + 4\tau_1\tau_2)}{(\tau_1\tau_2)^{1/2}}, \tag{3.9}$$

and $\tau_r = \frac{T_r^2}{(2-T_r)^2}$ are the effective Andreev transmissions of the barriers. The terms in the first line of eqn. 3.7 are negative. Positive correlations are added by the γ_+-term which has a 'CAR-like' dependence on the density of states. The γ_- term comes with a negative sign and has an 'EC-like' density of states-dependence. For $T > \frac{2}{3}$ γ_- becomes negative and the term also contributes positively to nonlocal current correlations. When comparing eqn. 3.7 in the zero-frequency limit ($\omega \to 0$) to the results by Mélin et al. (see Fig. 3.11(b)), we find that the general trends of the BTK model calculation and the numerical microscopic Green's function results are reproduced.

We may summarize important features of the various theoretical models for current correlations: Firstly, for highly-transparent interfaces ($T \simeq 1$) positive correlations are expected and higher-order processes (e.g. $AR - \overline{AR}$) contribute significantly. For 'CAR-like' processes Pauli blocking introduces a minimum in the current correlations at $V_1 = -V_2$ because of a lack of available electron and hole quasiparticle states. Secondly, for intermediate interface transparencies ($T \simeq \frac{1}{2}$) the positive contributions of higher-order processes are diminished and the correlations become negative. Thirdly, depending on device geometry and similar interface transparencies at both contacts, a 'W'-shaped dependence of the current correlations on bias voltage may be observed. It has two minima at bias voltages $V_1 = \pm V_2$ which correspond to 'CAR-like' and 'EC-like' density of states dependence of the involved processes. We will use the above mentioned characteristics to guide the discussion of our experimental results in Chapter 5.

In the next chapter we will concern ourselves with the practical implementation of shot noise and current correlation measurements. Important considerations regarding sample design and details of our measurement setup will be discussed.

Chapter 4

Methods

4.1 Sample considerations and fabrication techniques

4.1.1 Reservoir heating

In shot noise experiments the physical system under investigation is driven far out of thermal equilibrium. For electrical devices this is achieved by attaching charge carrier reservoirs (with well-defined temperatures and chemical potentials) to the device and applying a voltage difference between them. The bias voltage has to be larger than the thermal energy scale of the system, $|eV| \gg k_{\mathrm{B}}T$. In a device of electrical resistance R the external bias generates the power $P = V^2/R$ which must be dissipated in the reservoirs without changing their temperature significantly. One way to ensure adequate thermal and electrical conductance of the reservoirs is by proper choice of geometry and material. Following the work by Henny *et al.* [47] I will summarize how an estimate of the effective reservoir temperature in a biased system can be obtained. A more detailed discussion of the relevant mechanisms is given in [61].

Schematically heating effects can be described by a chain of (nonlinear) thermal resistances (Fig.4.1). The temperature drop over each resistance is a function of the dissipated power P and the temperature T_{x-1} of the subsystem which acts as heat sink, $\Delta T_x = R_x(P, T_{x-1})$. The device sees an effective reservoir temperature $T_{\mathrm{eff}} = T_{\mathrm{bath}} + \sum_x \Delta T_x$, where T_{bath} is the temperature of the cryogenic bath, i.e. the mixing chamber temperature of the dilution refrigerator.

When the sample is biased, a power $P = V^2/R$ is generated and must be dissipated in reservoir and substrate. The device experiences the effective temperature $T_{e,hi}$ of the electron system in the thermalization region of the reservoir close to the contact, see Fig. 4.1. In the absence of inelastic impurity scattering electron-electron interactions will thermalize the energy distribution of electrons. Thus the characteristic dimension of thermalization region is set by the electron-electron scattering length, $\ell_{\mathrm{e-e}}$. At milli-Kelvin temperatures the scattering length can be quite long, e.g. $\ell_{\mathrm{e-e}} \sim$ several 10 μm in long metallic wires[46, 47].

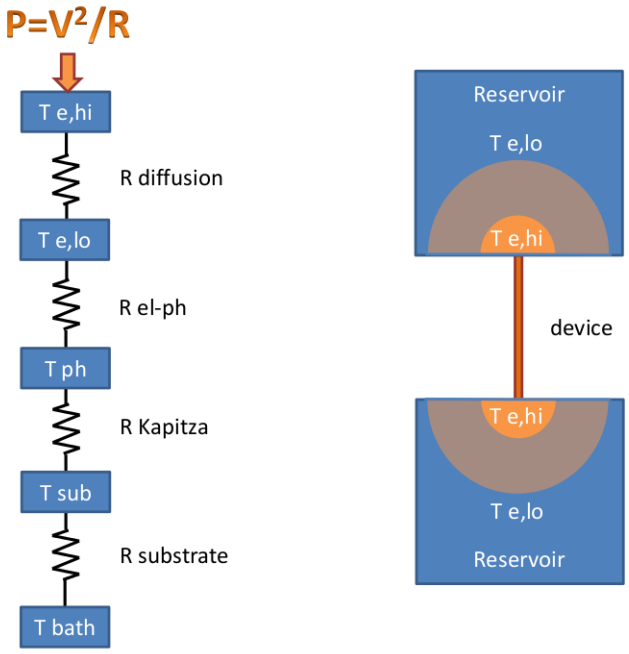

Figure 4.1: Reservoir heating: The power $P = V^2/R$ that is generated in the device and must be dissipated in the reservoirs and substrate. The thermal impedances are symbolized by a chain of resistors between heat baths (left). The temperature difference between baths depends on the thermal impedance and the dissipated heat. The device experiences the effective temperature $T_{e,hi}$ of the electrons in the thermalization region close to the contact (right). The heat diffuses away from the contact into the reservoir ($R_{\rm diffusion}$). Far away the electron temperature drops to $T_{e,lo}$. The heat is transferred into the phonon system of the reservoir by electron-phonon scattering ($R_{\rm el-ph}$) and passed on into the phonon system of the substrate ($R_{\rm Kapitza}$). The thermal impedance between substrate and cryogenic bath is represented by $R_{\rm substrate}$).

The heat diffuses radially away from the contact region and distributes the heat in the reservoir. The electron temperature drops to $T_{\rm e,lo}$ over a distance which is set by the smaller of the electron-phonon scattering length, $\ell_{\rm e-ph}$, and the smallest reservoir dimension l. To obtain an estimate for the temperature difference between $T_{e,hi}$ and $T_{e,lo}$, we solve the two-dimensional heat diffusion equation $\mathbf{j}_Q = -\kappa\nabla T_{\rm e} = \frac{P}{2\pi r t} e_{\mathbf{r}}$ in radial coordinates. The thermal conductivity is given by the Wiedemann-Franz law $\kappa = \frac{\pi^2}{3}\sigma T_{\rm e}$ and we find

$$T_{\rm e,hi}^2 = T_{\rm e,lo}^2 + \frac{3}{\pi^3}\frac{R_\Box}{R}\ln\left(\frac{\ell_{\rm e-ph}}{\ell_{\rm e-e}}\right)\left(\frac{e}{k}\right)^2 V^2 \tag{4.1}$$

Here the resistance per square $R_\Box = 1/\sigma t$ is introduced to replace the product of reservoir conductivity σ and thickness t. The ratio of reservoir sheet resistance to sample resistance, $R_\Box/R$, is the relevant design parameter for reservoirs.

For simplicity let us now assume the electron temperature is $T_{\mathrm{e,lo}}$ everywhere in the reservoir. By equating the power which is dissipated by electron-phonon collisions in the reservoir volume Ω to P/Ω the difference between phonon and electron temperature is estimated by [108]

$$T_{\mathrm{e,lo}} = \left(T_{\mathrm{ph}}^5 + \frac{1}{\chi A} \frac{R_\square}{R} (\frac{e}{k})^2 V^2 \right)^{\frac{1}{5}} , \tag{4.2}$$

where A denotes the reservoir area. The parameter χ is know from studies of electron-phonon scattering in long diffusive wires [47], where $\ell_{\mathrm{e-ph}} = 1.31/\sqrt{\chi T_{\mathrm{e}}^3}$.

The acoustic mismatch between reservoir and substrate material creates an additional boundary (or Kapitza) resistance which causes a temperature difference between reservoir and substrate phonons,

$$T_{\mathrm{ph}} = \left(T_{\mathrm{sub}}^4 + \frac{P}{A\sigma_K} \right)^{\frac{1}{4}} , \tag{4.3}$$

where σ_K is a parameter, which characterizes the interface. Finally, the temperature difference between substrate phonons and cryogenic bath depends on the thermal resistance between substrate and test fixture and the thermal resistance of the fixture to the bath. The latter is typically dominated by (several) compression joints between the metal parts of the fixture and the refrigerator. In a carefully designed test fixture these contributions are negligible compared to the other effects which are discussed above.

$R_\square/R$	≈ 0.01
$\ell_{\mathrm{e-ph}}/\ell_{\mathrm{e-e}}$	≈ 50 at $T = 100$ mK
d	1 mm
χ_{Cu}	8.9×10^9 m^{-2}.K^{-3} [61]
σ_K	60 W.m^{-2}.K^{-4} [109]

Table 4.1: Typical reservoir parameters.

We can now proceed to obtain an estimate of the effective reservoir temperature in the experiments. Using device and material parameters of the copper-aluminum NSN samples of this study (table 4.1) we calculate the electron temperature in the contact area between reservoir and device, $T_{\mathrm{e,hi}} \approx 142$ mK for a mixing chamber temperature $T_{\mathrm{bath}} = 100$ mK and an applied voltage of $V \lesssim 100$ μV. However, the value might be overestimated, as inelastic impurity scattering processes which also transfer energy from the electron system to the reservoir lattice are not taken into account in the above analysis.

4.1.2 Nanopatterning of metallic wire structures

Mesoscopic phenomena are observed at an intermediate length scale when characteristic system dimensions are much larger than the size of individual atoms yet small enough for the system to retain quantum mechanical properties which are not accessible in larger, truly macroscopic samples. At low temperatures quantum mechanical effects can be observed for distances up to several microns in solid-state systems. The upper limit is typically set by some inelastic scattering processes which destroys wavefunction coherence.

Great advances in the study of mesoscopic physics have been made possible by the steady improvement of micro- and nanofabrication techniques. While two-dimensional quantum systems can be obtained with thin-film deposition or exfoliation methods in a straight-forward manner, lateral structuring requires more involved lithographic methods. Electron-beam lithography has become a standard tool for sub-micron patterning in research applications and was used for the fabrication of the metallic wire structures in this study. With state-of-the-art electron-beam lithography tools (such as the Raith e-Line instrument at the Microfabrication Facility of the Frederick Seitz Materials Research Laboratory) feature sizes ~ 10 nm and equal precision in the alignment of subsequent patterning layers are routinely achieved.

Below I will give details of the fabrication process for sub-micron normal metal-superconductor devices for shot noise measurements. As outlined above it is essential to attach large normal metal reservoirs to the structure. At the same time good contact between the wire part and the reservoir portion of the normal metal structure is required. In a first batch of test samples a 3 step EBL process was executed by first defining the normal metal wires, then adding the reservoirs and the superconductor structure. Before deposition of each subsequent metal layer a gentle surface clean by argon ion etching removed surface contamination and surface oxides from the underlying structure. The superconductor is added last because the aluminum wires need to be much thicker than the normal metal wires to minimize gap suppression effects in the contact area. The same procedure was chosen for the sample without reservoirs in the length dependence study.

While the 3-step lithography process is simple to execute it is desirable to minimize the exposure of the copper wires to the processing chemicals. Chemical impurities and surface oxides add inelastic and spin-flip scattering in the wires. To reduce the number of processing steps in later samples the thinner copper wires and the thick reservoirs were deposited in a single step using the angle evaporation (or shadow mask) technique . Between processing steps vacuum storage or storage in pure argon gas prevented surface oxidation of the metal films. Immediately after the final processing step electrical connections were made with a wirebonder and the device was cooled down for testing as room-temperature inter-diffusion between

copper and aluminum (or gold and aluminum in some devices) quickly degrades the quality of the interfaces between the two metals.

Substrate preparation

Samples are prepared on a single-side polished silicon substrate of 300 μm thickness. The substrates are doped and conducting with a room-temperature resistance of 1–5 Ω·cm which is necessary to drain the charge from the electron beam that is used during the patterning process. The doping is non-degenerate and thus the substrate becomes insulating when the temperature is lowered. A 500 nm thick layer of thermally-grown silicon-oxide provides electrical insulation between sample and substrate which allows us to test the device resistances at room-temperature. Before processing commences the surface is cleaned from organic residues by etching in a 1:1 (by volume) solution of sulfuric acid and hydrogen peroxide (96% H_2S0_4:30% H_2O_2) for 10 minutes and a subsequent triple wash in deionised water. In a second step metallic (ionic) contaminants are removed by immersing the substrate in a 1:1:6 solution (by volume) of HCl:30% H_2O_2:H_2O at 80℃ for 10 minutes, again followed by a triple wash in deionised water. The substrates are then blow-dried and baked at 180℃ on a hot plate to remove adsorbed water.

Electron-beam lithography

In standard photo- and electron-lithographic methods the substrate is spin-coated with a layer of polymer resist. A pattern is formed by irradiating portions of the film with ultra-violet light or an electron beam. In positive tone lithography a sufficiently high radiation dose breaks down the polymer chains and the broken-down polymers are washed away by developer chemicals. In negative tone lithography the polymers are cross-linked and only exposed areas remain covered after the developing process. Positive tone resist is typically used for lift-off processes where the resist forms a sacrificial layer that acts as a patterning mask for material deposition. After the deposition the photo-resist mask is "lifted-off" and only material that was deposited directly onto the substrate remains.

The poly-methyl-methacrylate resist PMMA A4 by MicroChem Corp. was used for all electron-beam lithography (EBL) steps. The substrates were spin-coated with two layers of PMMA A4 at 2000 rpm for 45 seconds and dry-baked at 180℃ for 60 seconds. This resulted in EBL resist stack of $\approx$ 400 nm thickness.

Subsequently the resist was exposed with the Raith e-Line tool by Fa. Raith GmBH, Germany. The tool consists of a Scanning Electron Microscope column by Carl Zeiss AG, Germany, with integrated pattern generator and deflection electronics by Raith. It features a laser-positioned sample stage which performs

advanced positioning tasks and allows for high-precision pattern stitching. The highest electron energy of 30 keV was chosen for the exposure to minimize electron backscattering from the substrate thus forming only a small undercut region in the exposed resist. The minimal clearing dosage was found to be $\approx 315\ \mu C/cm^2$ and shape biasing methods were applied to obtain the desired mask geometry. Small features were exposed with a 20 μm aperture size for the electron beam and a beam current of 150 pA. For large reservoir areas and wirebonding pads a larger aperture of 120μm with a resulting larger beam current of 6 nA were used. Aside from the device a set of alignment marks was defined to index the position of the device for subsequent patterning steps.

The exposed areas of the resist film were cleared by a 70 second immersion in a 1:3 (by volume) solution of methyl-isobutyl-ketone (MIBK) and isopropyl alcohol (IPA). This was followed by an IPA wash of 30 seconds duration and blow-drying the sample with nitrogen gas. Resist and solvent residues were removed by a 45 second low-power oxygen plasma ashing using a PDG-32G plasma cleaner by Harrick plasma, Ithaca, NY.

Metal deposition

The metal deposition was carried out in a high-vacuum system with a base pressure of 5×10^{-8} Torr. The sample was attached to a sample holder and transferred into the vacuum chamber. Inside the chamber the sample holder mount was cooled to liquid nitrogen reservoir. After the sample holder had reached sufficiently low temperatures for the deposition, it was transferred to a magnetically-coupled movable rod. A Thermionics 2 kV research-style electron-beam evaporator was used to deposit metal vapor onto the substrate. In the angle evaporation procedure 50 nm of 99.9999% (6N) pure copper was deposited perpendicular onto the substrate surface. Next the sample was tilted by 30° and another 230 nm of copper were deposited for the reservoirs, see figure 4.2. In the narrow EBL resist gaps which define the shape of the normal metal wires the material accumulates against the sidewalls of the resist film thereby avoiding to form a shadow deposit typical of the shadow-angle mask method which in this device geometry would create an electric short. For other fabrication steps sources of 99.999% (5N) pure aluminum, 99.995% pure palladium, and 99.999% (5N) gold were used. Angle deposition was not required.

After deposition the resist mask was removed by immersion in a bath of Remover PG at 50℃ for 30 minutes. Remover PG is a product of Microchem Corp. which is based on the organic solvent N-Methyl-2-pyrrolidone (NMP). Residues of the lift-off chemicals were eliminated by dipping the sample in an acetone bath followed by an immersion bath in IPA for 5 minutes and blow-drying the substrate with dry nitrogen

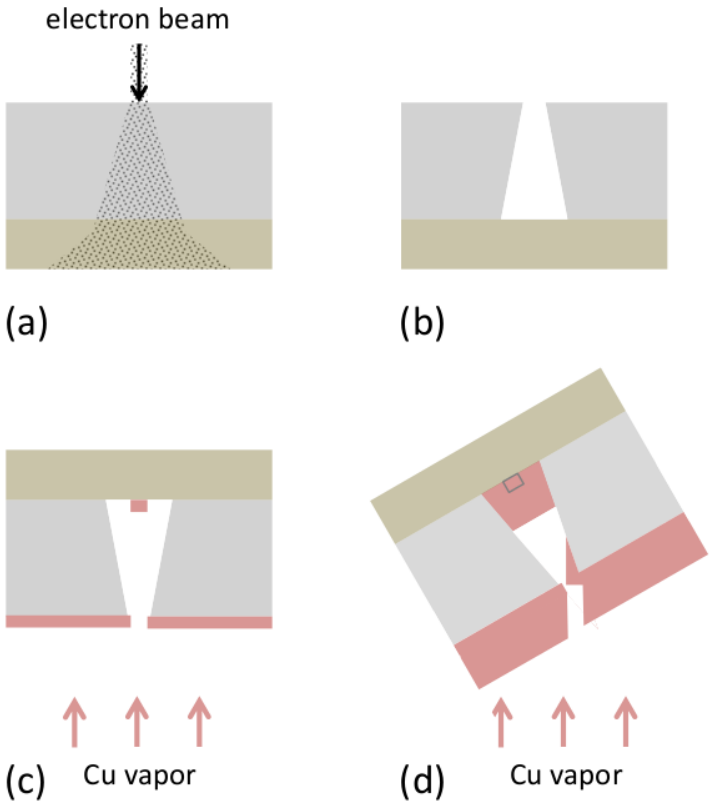

Figure 4.2: Electron-beam lithography and shadow-angle evaporation: The EBL resist is exposed with an electron beam (a). Scattering of the electrons in the resist and backscattering from the substrate results in a small undercut region after developing removes the exposed resist (b). In the first step of the shadow mask evaporation the material is deposited perpendicular to the substrate surface (c). Before depositing the second layer, the sample is tilted by 30°(d).

concluded the procedure.

4.2 Measurement techniques

4.2.1 Noise measurements on low resistance samples

The low source impedance of the normal metal-superconductor device adds an additional level of complexity to the experiments. Whereas for high impedance samples such as single electron transistors (SETs) [110] or 2-dimensional electron gas devices (2-DEGs) [111, 64] it suffices to send a current through the sample and measure the voltage fluctuations, in our samples the voltage fluctuations are much smaller than the intrinsic noise of the voltage preamplifier. We need to resolve current correlations of magnitude $10^{-2} - 10^{-3}$

in samples of source resistance $\leq 10\ \Omega$ at milli-Kelvin temperatures. The commercial low-noise preamplifier SR552 from Stanford Research, Inc., which is often used for low impedance samples has a noise figure of 20 dB at a frequency of 1 kHz for an input resistance of 10 Ω[112], i.e. the voltage noise is 10 times larger than the thermal noise of a 10 kΩ resistor at room temperature. This corresponds to an input-equivalent base noise of $\sim 1.7\ \mathrm{nV}^2/\mathrm{Hz}$ which is 4 orders of magnitude larger than the thermal voltage fluctuations of a 10 Ω resistor at 100 mK. A cryogenic amplifier stage will improve this ratio insignificantly. A different measurement method is needed to resolve current noise in such samples.

DC-Superconducting Quantum Interference Devices (dc-SQUIDs) are used as sensitive current meters in many applications[113, 114]. High-quality commercial sensors and feedback electronics are available [115, 116]. A STAR Cryoelectronics SQ680 dc-SQUID sensor which is operated in flux-locked feedback mode has a total gain $G \sim 3.5 \times 10^6$ V/A [117]. The current noise floor is dominated by the flux noise in the SQUID sensor $S_\Phi^{1/2} \sim 5\ \mu\Phi_0/\sqrt{\mathrm{Hz}}$, where $\Phi_0 = \frac{\mathrm{h}}{2\mathrm{e}_0} \approx 2 \times 10^{-15}$ Wb is the magnetic flux quantum. Using the mutual inductance M_{in} between input inductor and SQUID loop this results in an input-equivalent current noise floor of $S_\mathrm{I} = S_\Phi \times M_{\mathrm{in}}^2 = 10^{-24}\ \mathrm{A}^2/\mathrm{Hz}$, which is of the same magnitude as the current noise of a 10 Ω resistor at 100 mK, $S_\mathrm{I} = 4k_\mathrm{B}T/R \approx 0.5 \times 10^{-24}\ \mathrm{A}^2/\mathrm{Hz}$. Thus commercial SQUIDs are well suited as current detectors in low temperature noise experiments with small sample resistances $\leq$ 10 Ω.

SQUIDs have previously been used for noise and correlation measurements of mesoscopic metallic structures [53, 46, 63]. For this study an electrical circuit for cross-correlation experiments has been devised which consists of two independent SQUID resistance bridges [62] for the two branches of the NSN samples. Thus – unlike in the experiment of reference [63] – it is possible to bias the two contacts independently. The use of four opto-isolated current sources allows to define signal ground at the sample inside the cryostat and ensures that sources of spurious cross-talk are eliminated, i.e. external noise is efficiently filtered from bias lines and ground loops are avoided. After a brief discussion of the measurement principle and circuit analysis of a single SQUID bridge circuit, I will present the circuit for nonlocal voltage and noise correlation measurements. I will conclude this section with implementation details and a description of the measurement electronics.

4.2.2 The SQUID resistance bridge circuit

A resistance bridge circuit is formed by connecting the sample with dynamic resistance $R_\mathrm{X} = R_\mathrm{X}(V)$ in series with the (superconducting) input inductor of a SQUID and a resistor of known value ("standard resistor") R_S. The condition $R_\mathrm{S} \ll R_\mathrm{X}$ is necessary for a sensitive readout of the current fluctuations in the sample.

Current sources are attached in parallel to the two resistors and the SQUID is used as null-detector for dc-current between the two branches of the bridge circuit. A schematic is provided in figure 4.3(a). Ideally, all connections between circuit elements in the resistance bridge loop are superconducting. Any additional connection resistance r_i (not included in the schematics of fig. 4.3) must be kept small, $r_i \ll R_X, R_S$, to achieve reasonable accuracy in the measurements. Contact resistances r_i will add a constant contribution $\approx 4k_B \sum_i (T_i r_i)/(R_X + R_S)^2$ to the detected current noise. Thus failure to make a superconducting joint at the input terminals of the SQUID, which is kept at a much higher temperature than the sample, can introduce a significant error in the readout and must be avoided.

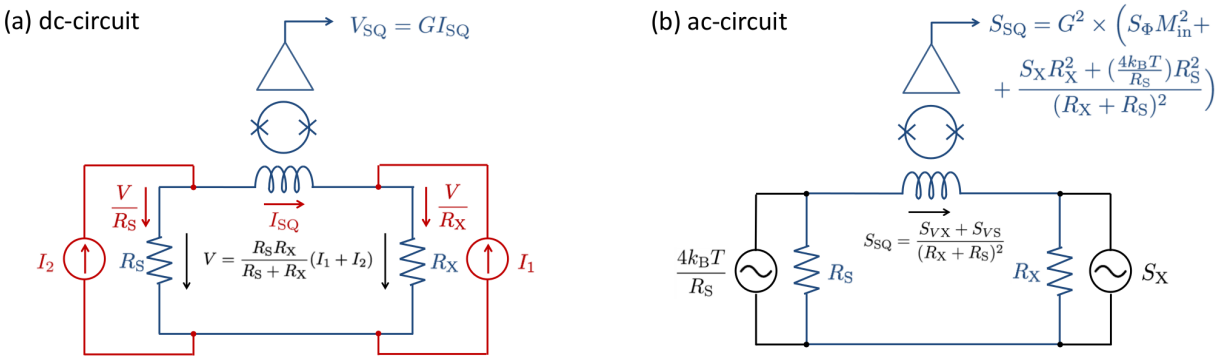

Figure 4.3: Simplified schematics of the SQUID resistance bridge: The circuits for DC-feedback measurement (a) and the AC-equivalent circuit which is used in the analysis of the current noise measurement (b). The noise characteristics of sample and standard resistor are modeled by connecting an ideal noise source in parallel to an ideal (noiseless) resistor.

To illustrate the measurement principle we start with an unbiased circuit, $I_1 = I_2 = 0$ and $V_{SQ} = 0$. The current I_1 is increased in small steps. It divides between the sample and the standard resistor branch of the circuit. The current which flows toward the standard resistor is detected by the SQUID resulting in a dc-voltage signal $V_{SQ} \neq 0$. Next, I_2 is slowly adjusted until the SQUID signal disappears, $V_{SQ} = 0$. This "slow feedback" method was chosen because RC filters in the bias lines limit the feedback bandwidth to a few Hz. When the bridge is balanced, $I_1 = I_X$ and $I_2 = I_S$. Since R_S is known, we can calculate the voltage across the sample, $V_X = V_S = V = I_S R_2$. By differentiation, we obtain the dynamic resistance of the sample

$$R_X(V) = R_S \frac{dI_S}{dI_X} = R_S \frac{dI_2}{dI_1}\Big|_{bal,V} . \tag{4.4}$$

Once the circuit is balanced, the SQUID voltage noise S_{SQ} can be recorded, e.g. by a FFT analyzer. There

are two contributions: the (constant) flux noise from the SQUID sensor and the current fluctuations in the input inductor which consists of a sample component and the Johnson noise contribution from the standard resistor. In the following analysis it is most convenient to replace the current noise sources in figure 4.3(b) by Thévenin-equivalent voltage noise sources in series with ideal, noiseless resistors. They represent the voltage fluctuations across the physical resistors. We can now relate the total current fluctuations in the loop to the voltage fluctuations at sample and standard resistor by the square of the total circuit impedance,

$$S = \frac{S_{V\mathrm{X}} + S_{V\mathrm{S}}}{(R_\mathrm{X} + R_\mathrm{S})^2} \ .$$

In the last equation we neglected a small contribution from the input inductance of the SQUID, as $\omega L_\mathrm{in} \ll R_\mathrm{X}, R_\mathrm{S}$ in the experiment. The total voltage noise at the SQUID output is ($S_0 \equiv S_\Phi M_\mathrm{in}^2$):

$$S_\mathrm{SQ} = G^2 \times \left(S_0 + \frac{S_\mathrm{X} R_\mathrm{X}^2 + (\frac{4k_\mathrm{B}T_\mathrm{S}}{R_\mathrm{S}}) R_\mathrm{S}^2}{(R_\mathrm{X} + R_\mathrm{S})^2} \right) .$$

From the last equality we find the expression for the current noise in the sample,

$$S_\mathrm{X} = \frac{(S_\mathrm{SQ} G^{-2} - S_0)(R_\mathrm{X} + R_\mathrm{S})^2 - 4k_\mathrm{B}T_\mathrm{S}R_\mathrm{S}}{R_\mathrm{X}^2} \ . \tag{4.5}$$

More precisely, the quantity S_X is the current noise which would be observed, if the sample were not shunted by the standard resistor [60]. Equation 4.5 requires us to know the flux noise offset, S_0, and the temperature of the standard resistor, T_S. In the experiments standard resistors were thermally anchored to the sample PCB board at mixing chamber temperature, $T_\mathrm{M/C}$; $T_\mathrm{S} = T_\mathrm{M/C}$ is assumed without further mentioning.

4.2.3 The cross-correlation circuit

For nonlocal voltage and current cross-correlation experiments a bridge circuit is attached to each branch of the sample that is to be studied, see figure 4.4. The measurement principle is unchanged. The sample bias current is stepped in small increments and both bridge circuits are balanced simultaneously using the respective SQUID as null-detector for current in the loop. Any voltage change across the sample branch will be followed by a change in the bias current for the standard resistor. The current-voltage characteristic for arbitrary sample bias can be obtained in this way. In the study of nonlocal transport it is useful to normalize the change in nonlocal voltage V_i by the change in the driving current $I_{\mathrm{X}j}$, thus we define a nonlocal dynamic resistance (or "nonlocal resistance")

$$R_{ij} \equiv R_{\mathrm{S}i} \frac{\partial I_{\mathrm{S}i}}{\partial I_{\mathrm{X}j}}, i \neq j. \tag{4.6}$$

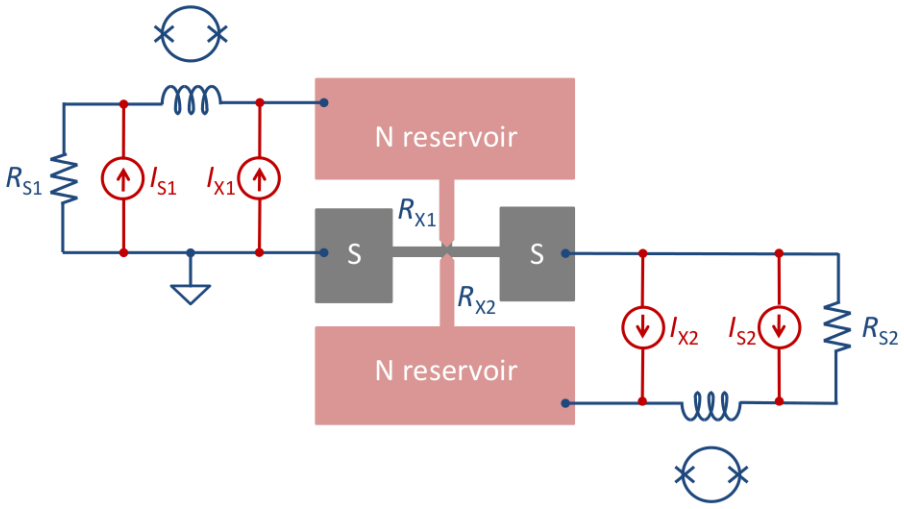

Figure 4.4: A simplified schematic of the SQUID resistance bridge circuit for nonlocal voltage and current correlation measurements.

The cross conductance in the device can be obtained by inverting the resistance matrix, we have

$$G_{ij} = -\frac{R_{ij}}{R_{\mathrm{X}i}R_{\mathrm{X}j} - R_{ij}R_{ji}} \ . \tag{4.7}$$

Flux noise in the SQUIDs and thermal noise in the standard resistors are uncorrelated noise sources and can be disregarded in the analysis of noise cross-correlations. Correlated current fluctuations in the device are partially shunted by the finite impedance of the standard resistors in the resistance bridge circuits. The branch resistance $R_{\mathrm{X}i}$ of the sample and the standard resistor $R_{\mathrm{X}i}$ form a current divider: A fraction $R_{\mathrm{X}i}/(R_{\mathrm{X}i} + R_{\mathrm{S}i})$ of the fluctuating current flows in the standard resistor branch and is detected by the SQUID. Again, we disregarded the input inductance of the SQUID. We can calculate the cross spectral density of current fluctuations for the unshunted device from the correlations in the SQUID signals,

$$S_{12} = G_1 G_2 \times S_{\mathrm{SQ}12}\Big(\frac{R_{\mathrm{X}1} + R_{\mathrm{S}1}}{R_{\mathrm{X}1}}\Big)\Big(\frac{R_{\mathrm{X}2} + R_{\mathrm{S}2}}{R_{\mathrm{X}2}}\Big), \tag{4.8}$$

where G_i is the gain of SQUID i.

4.3 Implementation

The study of Cooper-pair mediated nonlocal transport and current correlations in nanofabricated devices requires the use of a superconducting material with long coherence length. A suitable material is aluminum with a critical temperature, $T_c \approx 1.2$ K, and a dirty-limit coherence length, $\xi_D \approx 100 - 200$ nm (typical value in thin-film devices). The excitation gap 2Δ of superconducting aluminum sets the voltage scale in the experiments. Subgap bias requires $V_{\mathrm{X1}}+V_{\mathrm{X2}} \leq \Delta/e_0 \approx 200\ \mu$V. Biasing currents are limited by the depairing current in the superconducting wire of the structure which is measured to be (several) 100 μA for the wires of this study. Therefore, the resistances of the normal metal contacts are chosen in the range 1-10 Ω. The upper limit is imposed by the noise floor of the SQUID sensors which are used for the measurements. The temperature of the experiment must be low such that $k_{\mathrm{B}}T \ll e_0V_{\mathrm{X1}}, e_0V_{\mathrm{X2}} \sim 100\ \mu$eV which requires the use of a dilution refrigerator. On the other hand, given our choice of materials and sample geometry, reservoir heating effects are large below T =100 mK, which imposes a practical lower limit. Below I will describe the experimental setup in detail and address additional design requirements:

1. Several layers of rf- and magnetic shielding are necessary to decouple sample and measurement SQUIDs from the noisy laboratory environment.

2. Filtering and shielding of high-frequency (hf) thermal radiation ($f \gtrsim 1$ GHz) from sections of higher temperature in the cryostat must be employed to ensure that the sample thermalizes at the required low base values.

3. Quiet biasing electronics with a noise floor below the scale of the current noise signals in the sample are needed.

4. Bandwidth limitations of the SQUID feedback circuitry require a calibration in the frequency range of the measurement.

4.3.1 Measurement setup

The experiment was set up in a Kelvinox 400 dilution refrigerator by Oxford Instruments, PLC, U.K., with a base temperature of 9 mK. The cryostat is located in an rf-shielded room which is connected to its own earth ground, see figure 4.5. Pumping and gas handling systems of the refrigerator are outside the enclosure. During measurements the electrical power in the shielded-room is turned off which eliminates 60 Hz noise and harmonics. Only home-built battery-powered voltage sources and the STAR Cryoelectronics Phase-Locked Loop (PFL) electronics for both SQUID sensors are operated inside the room which shields the sensitive

electronics from electromagnetic pick-up. The thick steel panels also attenuate some of the magnetic signal generated by the pumping system. Despite some additional mu-metal shielding inside the room several broad low-frequency features originating from the pumping system are picked up by the measurement SQUIDs.

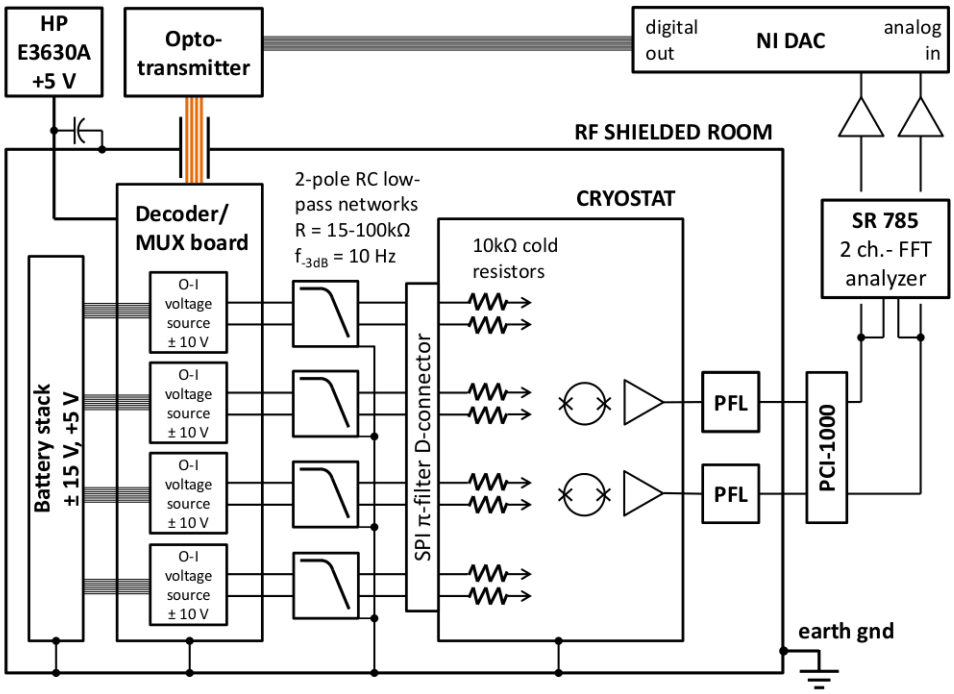

Figure 4.5: Wiring schematic of the experiments. Inside the rf-shielded room: Voltage source control box with optoreceiver and multiplexer, battery-operated opto-isolated voltage sources, 2-pol RC-filtering network for low frequency noise (together with 10 kΩ cold resistors), SQUID sensors and Programmable Feedback Loop electronics (PFLs). Outside the rf-shielded room: Personal Computer interface for PFLs, SR785 FFT analyzer, buffers and National Instruments DAC for SQUID dc-signal measurement, and DAC digital out with optotransceiver box and fiber-optic connection for communication with the voltage source control box inside the room.

SQUID current detectors

A commercial integrated 2-channel dc-SQUID system from STAR Cryoelectronics [116] was used for current detection in the resistance bridge circuits. The SQ680 dc-SQUID sensors with flux noise $S^{1/2} < 5\ \mu\Phi_0/\sqrt{\text{Hz}}$ are packaged in a customized LS 2076 package to which an extra copper braid is attached for heat sinking. L6118 niobium shield assemblies provide the magnetic shielding for SQUIDs and are mounted side-by-side on a copper plate which is attached to the 1K reservoir plate ($T_{1\text{Kpot}} \approx$1.6 K), see figure 4.6. A compression joint between the braid and the copper plate provides the thermal connection between the SQUID package and the 1K reservoir, necessary for operation in vacuum. Two custom-ordered stainless steel braid-shielded cryocables with copper heatsinks connect the SQUIDs to the programmable feedback-loop electronics (STAR

Cryoelectronics Model PFL-100) on top of the refrigerator. The heatsinks are connected to the top plate of the IVC ($T \approx$4.2 K) and at the 1K reservoir.

The PFL-100 generates its own clock signal for the lock-in measurement of the flux-locked loop SQUID read-out. It is recommended to synchronize the clocks of PFLs which are connected to the same system to avoid beating effects by crosstalk. This is a potential concern for cross-correlation experiments on devices. To test for crosstalk the two bridge circuits were attached to two independent samples in the test fixture and the cross-correlation signal was determined for different values of sample bias of the individual devices. Irrespective of the operation mode, only a bias independent noise floor was observed in the cross-spectral density of the SQUID voltage signals. Henceforth, the PFLs were operated in synchronized (or "master-slave") mode.

Well-shielded standard D-sub cables link the PFLs to a STAR Cryoelectronics Model PCI-1000 personal computer interface outside the shielded room. The interface provides DC power to the individual PFLs and buffers the SQUID feedback signal that it receives from the feedback electronics. The same cable is also used to change feedback-loop settings through an optoisolated digital communication interface with the PFLs. The buffered flux-locked loop signals are digitized by a SR785 dual-channel FFT analyzer by Stanford Research. The DC levels are measured by a National Instruments general purpose Digital-to-Analog Converter (DAC). Between SR785 inputs and DAC another buffer stage is used to minimize interference by the noisy DAC interface.

The SQUID input wiring is made from twisted copper-clad superconducting wire and shielded with superconducting lead tubing, see figure 4.6. Sample and bridge circuits reside in a hermetically sealed, radio frequency (rf)-tight enclosure which is attached to the mixing chamber of the dilution refrigerator. The SQUID leads are fed through stainless steel powder filters for rf-filtering. Before entering the powder filters a section of the copper-cladding has been etched away with nitric acid to minimize thermal conductance. Powder filters provide additional inductance and ensure that no rf-signals from the SQUID side couples back to the sample. The enclosure is surrounded by a magnetic shield made from Cryoperm 10, a soft-magnetic Ni-Fe-based alloy for applications at low temperature, which is lined with superconducting lead. This minimizes magnetic pick-up in the loops that are formed by the elements of the bridge circuits. Connections to superconducting solder traces on the printed-circuit board with sample and bridge circuits are made by another set of screw terminals.

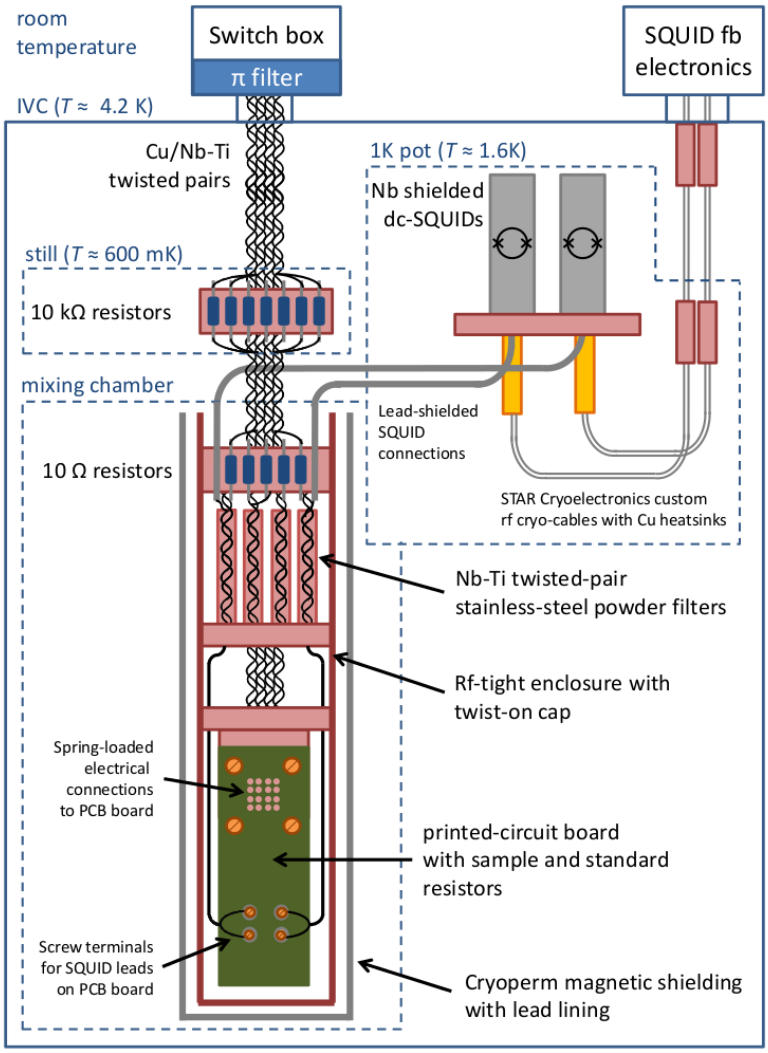

Figure 4.6: A schematic of the low-temperature experimental setup: Switch box with π-filter at room temperature; low-temperature bias resistors at the still of the refrigerator; rf-tight enclosure and high-frequency filtering, magnetic shielding, and sample mount for PCBs with spring-loaded connector attached to the mixing chamber; and DC SQUID sensors at the 1K reservoir with cryo-cable connections to the feedback electronics.

Sample mount and standard resistors

For sensitive detection of current fluctuations with a SQUID resistance bridge circuit the standard resistor R_{S} must be smaller than the device resistance R_{X}. Our optoisolated 10 V DAC voltage sources and the necessary RC-filtering network limit the bias currents to $\leq$ 1 mA. Thus standard resistor values are chosen in the range $R_{\mathrm{S}} = 0.4 - 1.2\ \Omega$ and constitute about $10\% - 20\%$ of the total resistance in the loop of the bridge circuit. Therefore, it is essential to place them with the sample at the lowest temperature.

Home-made thin-film resistors are used as standard resistors. They consist of a 90 nm thick film of Au:Cu alloy (ratio 1:1 by-weight) which is thermally evaporated onto a 5 mm-by-5 mm sapphire substrate through a mechanical mask. An additional layer of gold ($50-90$ nm) is evaporated perpendicular across the resistive film for bonding pads. The large surface area of the film and the good low-temperature thermal conductivity of sapphire provide the necessary heat dissipation for the resistor.

The "chip-on-board" method was chosen for a simple, cost-effective way of packaging sample and resistance bridge circuit. The whole circuit is quickly assembled using standard wirebonding methods. During the bonding process the board connections are shorted together with standard miniature connectors which are used in the mobile phone industry. Sample-to-board connections are made with aluminum wirebonds. Gold wirebonds are used for the standard resistors as they also transport heat away from the resistors. Gold bonding is not possible for the sample connections as it is a *thermosonic* bonding method and thus requires heating to temperatures $T \geq 100$ ℃. Elevated temperatures will degrade the sample. Sample damage from electrostatic discharge is prevented by grounding the circuit traces to the wirebonder and removing static charge from the sample with an α-radiation source (Polonium-210) before making bonds. The shorting plug will be removed after the circuit is installed in the test fixture. Sample and standard resistors are mounted with silver paint onto the copper ground-plane of the custom-made printed-circuit board (PCB). Thermal connection to the sample fixture is made through 4 compression joints with brass screws. They also press the PCB against spring-loaded connectors ("POGO pins") which provide the electrical connection between the sample fixture wiring and the PCB. The SQUID leads are connected with screw terminals (see above).

Rf-shielding and high-frequency filtering

A black body's spectral radiance is given by (Planck's law)

$$B_\nu(T) = \frac{2h\nu^3}{c^2} \frac{1}{\exp(\frac{h\nu}{k_B T}) - 1} \ .$$

The maximum in the spectral distribution for a black body at 100 mK occurs at a frequency $\nu \approx 2.821 \frac{k_B T}{h} \approx$ 5.9 GHz. Thus a sample in thermal equilibrium with its environment at temperature $T \leq 100$ mK must be shielded from thermal radiation of frequency $\nu \gg 1$ GHz coming from parts of the cryostat with higher temperature. For this purpose the sample is sealed in a radio frequency-tight enclose with a screw-on cap which I machined from oxygen-free high-conductivity copper. All electrical connections are passed through stainless steel powder filter. They consist of 2.5 meters of twisted-pair copper-clad superconducting wires which are tightly wound into a coil around a cylindrical core of 1/8 in diameter made from a mixture of

Stycast epoxy and stainless steel powder, see table 4.2. The assembly is covered with another layer of the mixture, carefully inserted into a 1/4 in diameter copper tube and then topped off with more mixture.

80 g	Stycast 2580FT with catalyst 23LV (Emerson & Cumming)
70 g	Stycast 1266 (Emerson & Cumming)
200 g	stainless steel powder alloy 304 (non-magnetic) -325 mesh (by ESPI)

Table 4.2: The recipe for the stainless-steel powder and epoxy mixture used in powder filters. The epoxy is outgassed for 10 minutes under vacuum before the stainless-steel powder is mixed in. Cylindrical cores are formed by filling the mixture into Teflon tubing of the appropriate diameter using vacuum suction. While hardening the epoxy, cores and powder filters are attached to a rotator which prevents the stainless steel powder from settling.

The inner diameter of the copper tube determines the frequency cut-off for propagating electromagnetic modes in the tube, $\nu \leq 0.5$ GHz, which was verified by a transmission/reflection measurement of the powder filters with a network analyzer. The skin effect in the stainless-steel grains makes the powder-epoxy mixture lossy at high-frequencies and dampens wave propagation along the twisted-pair conductors. A similar effect is provided by 10 Ω metal-film resistors in the bias lines which are made from a Ni alloy and are glued into tight cylindrical holes in a copper disk at the entry point of the enclosure.

Environmental high-frequency noise from outside the cryostat is removed from the signal lines by a standard pi-filtered D-subminiature connector (from Spectrum Control, Inc.) in the switch box which connects at the top of the cryostat. The switches are used to short the signal lines together and connect them to chassis ground through a 10 kΩ resistor when attaching external measurement circuitry. This is a safety precaution against electrostatic discharge.

4.3.2 Biasing electronics

The bias currents for the bridge circuits are sourced from double optoisolated voltage sources which are powered from batteries, see figure 4.7 upper panel. This biasing scheme has the advantage that there exist no ground loops between the outside of the rf-shielded room and the electronics. The digital control signals for the voltage sources are generated by a National Instrument DAC and converted by an optotransceiver into laser pulses. Optical fibers connect the transceivers to a receiver array on the voltage source control board inside the rf-shielded room. The DC power for the control logic board is provided by a floated HP E3630A voltage source outside the rf-shielded room. Ground is defined at the feedthrough panel of the room and electromagnetic pick-up is rolled off with a large filter capacitor. The control board buffers and distributes the a clock signal and a serial 16-bit pulse train which encodes a voltage value to all installed voltage source (max. 15). Then a 4-bit address is transmitted to a multiplexer which determines the number

of the DAC voltage source which is supposed to set the new voltage value. The multiplexer sets the "load dac" or "LDAC" line of this voltage source to low thus changing the voltage of this source to the programmed value.

The voltage sources are based on the Analog Device AD660 DAC which has a 16-bit latch architecture, see figure 4.7 lower panel. New voltage values are programmed into the upper level latch register and loaded into the DAC latch when receiving the "LDAC" signal. Once loaded, the DAC changes to the voltage value which is encoded in the DAC latch. No other external signal is needed for the DAC to remain in this state. This architecture allows the DAC to be quiet when no digital communication occurs. All input signals to individual voltage sources are optoisolated, therefore no undesired ground loops are formed between the sources.

A two-pole RC low-pass filter with a -3dB frequency of ≈ 10 Hz rolls off 1/f-noise from the AD660 DACs. Each bias line is filtered separately. Additional 10 kΩ low-temperature resistors are installed at the still level. They are used to increase the bias line resistance and thus minimize undesired current fluctuations in the wiring leads. The total resistance in the RC network and the refrigerator wiring (including the 10 kΩ cold resistors) determines the current range for the individual biasing circuit. The current noise of the biasing electronics falls below the noise floor of the SQUID detector at a frequency $f \leq 1$ kHz which was determined in separate calibration measurements.

4.3.3 Noise measurement details

The SQUID feedback voltage signals are digitized by a Stanford Research SR785 dual-channel FFT analyzer. The instrument performs Fast-Fourier analysis by digital signal processing. The power spectral densities for both input channels and the real and imaginary parts of the cross spectral density are recorded for a frequency range $f = 5$ kHz – 6.4 kHz with 2500 averages (typ. values) and a resolution of 800 FFT lines. The frequency range was chosen well above the roll-off frequency of the filtering network of the biasing electronics and below the bandwidth limit of the feedback electronics.

The SQUID feedback electronics have a theoretical bandwidth limit [114, 117] characterized by the frequency at which the feedback gain has dropped by 3 decibels,

$$f_{-3\mathrm{dB}} = f_i \frac{G_{\mathrm{det}}}{G_{\mathrm{fb}}} = f_i \left(\frac{\partial V}{\partial \Phi}\right)_m \frac{M_{\mathrm{fb}}}{R_{\mathrm{fb}}} \ . \tag{4.9}$$

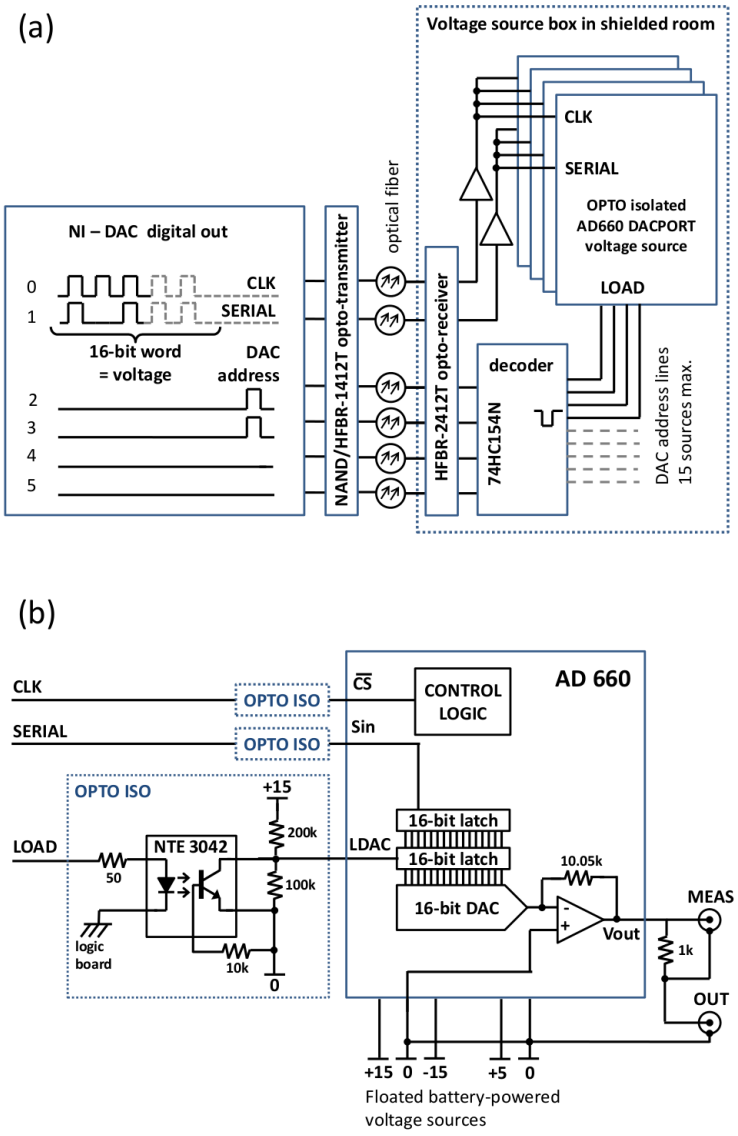

Figure 4.7: Custom-developed biasing electronics: A simplified schematic of the optoisolated programming electronics (a) for optoisolated AD660 DAC voltage sources (b). The double optoisolated design ensures that there are no ground loops between the data collection hardware outside the rf-screened room and the individual biasing circuits.

It originates from the RC-integrator stage that is used in the lock-in detection scheme for flux change in the SQUID. The characteristic frequency of the integrator is $f_i = 1/(2\pi RC)$. This must be scaled by the ratio of flux-to-voltage transfer coefficients in the feedback loop $G_{\rm det}/G_{\rm fb}$, where $G_{\rm det} = (\frac{\partial V}{\partial \Phi})_m$ is the SQUID transfer coefficient at the input of the integrator stage (i.e. after amplification) and $G_{\rm fb} = R_{\rm fb}/M_{\rm fb}$ is the gain of the flux feedback.

Using the datasheet parameters of our SQUIDs sensors, the ideal maximum feedback bandwidth is calculated to be $f_{-3\mathrm{dB}} \approx 15$ kHz. The real bandwidth is somewhat smaller as phase shifts in the electronics and wiring have been disregarded in the derivation of equation 4.9. The corner frequencies of the feedback circuits are of the same order of magnitude as the frequencies which are used in the noise experiments. Therefore for each experiment the exact gain of the SQUID feedback in the frequency range of interest was determined by measuring the Johnson noise of the resistance bridge $S_\mathrm{X} + S_\mathrm{S}$ and the zero-bias sample resistance R_X at several temperatures.

With the background information on sample design and fabrication as well as on the experimental techniques we used to acquire data, we will now proceed to discuss our experimental findings in the next chapter.

Chapter 5

Experimental results

Nonlocal subgap transport was observed in many mesoscopic superconductor - hybrid structures, e.g. with normal metal or ferromagnetic contacts, InAs quantum dots, and carbon nanotubes. Starting point of theoretical explanations are the mechanisms of crossed-Andreev reflection (CAR) and elastic co-tunneling (EC) (see Chapter 3). In the absence of spin-polarization the contributions of the two processes cancel to first order in tunneling probability. Non-perturbative calculations, numerical modeling, and calculations to all orders in perturbation theory suggest that coherent nonlocal transport should still exist – although an interpretation in terms of CAR and EC is not directly applicable. Previous studies of NSN structures in Andreev interferometers provided some evidence that nonlocal transport may be coherent, however the argument based on the current conversion in the contact area of one of the contacts and therefore addressed coherent processes between contacts only indirectly.

A surprising result of the class of theoretical models discussed above is that nonlocal current correlations are predicted to behave qualitatively different in the regimes of perfect transmission, intermediate barrier transparency, and tunnel barriers. The shape with respect to applied bias is distinct in each case. Thus the main objective of this study is to resolve nonlocal current correlations in mesoscopic NSN devices with transparent interfaces and compare it to the predicted behavior in the appropriate limit as direct proof for coherent nonlocal transport.

5.1 Overview

We will start the discussion with results on the distance dependence of nonlocal voltage signals in a superconducting wire. Previous experiments had been carried out in samples which exhibited strong inverse proximity effect [5] or were measured with ferromagnetic contacts [6]. We aim to clarify, if the suppression of the pairing potential is a necessary condition to observe finite nonlocal effects.

With this background we shift focus to the main body of work regarding current noise measurements in mesoscopic NSN devices. In the parameter region that is experimentally accessible to us, the injecting normal metal wires and the superconductor are in the diffusive limit. Typically the mean free path in the metals is $\ell \lesssim 20$ nm and thus much smaller than the relevant device dimensions $L \sim 0.1 - 1$ μm of our devices. And necessarily, for highly-transparent interfaces the normal metal wire part of our contacts will contribute most of the resistance. In this limit a comprehensive theoretical description is not available at this time. Therefore, an important part of the work was to develop the correct device geometry. Some of the initial designs were not suitable for studying nonlocal current correlations – the main goal of this work. Valuable insights from the earlier work was applied in subsequent experiments: I will present data of device **D1** in which current noise is dominated by reservoir heating and report on interesting observations regarding charge imbalance and nonequilibrium superconductivity in device **D2**. Although, our main focus of attention is on current noise and current noise correlations in the small bias regime, I will also include experimental results for the nonequilibrium state of the mesoscopic superconductor. To our knowledge current noise in this regime has not been explored so far. Therefore, I shall present some of the encountered effects which may provide a starting point for further experimental and theoretical studies.

The majority of data will be presented on devices **D3** and **D4**. The devices were fabricated simultaneously and thus allow us to compare datasets for the same materials and interface parameters at different contact separations. By means of numerical modeling of the contact resistances and by studying the shot noise of the individual contacts, wire and interface region with the superconductor were characterized and reasonable parameters were obtained. Most importantly, we were able to resolve the full bias dependence of nonlocal current correlations in these samples. Many aspects of the experimental data agree qualitatively with theoretical models for similar devices. We will conclude with a discussion of key observations.

5.2 Distance dependence of nonlocal transport

Our first experiment concerns the relationship between gap suppression and the distance dependence of nonlocal subgap transport in a superconducting wire. Similar experiments were performed by Beckmann et al. [6] and by Cadden-Zimansky and Chandrasekhar [5]. In the experiment of Beckmann et al., gap suppression was not reported. However, the experiment was carried out with ferromagnetic contacts thus there is no clear distinction between spin-imbalance effects and CAR and EC as the coherence length and the typical spin-flip length in aluminum thin-films are of the same magnitude. Our experiment is similar to the second measurement in using normal metal contacts. In reference [5] strong suppression of the pairing potential

and the critical temperature were observed. The suppression was attributed to the inverse proximity effect resulting from coupling many, closely-spaced normal metal contacts to the superconductor. The nonlocal signal was found to be large and decayed with an effective coherence length which corresponded well to a smaller pairing potential.

Our goal was to minimize the overlaps between the materials and test signal size and distance dependence of nonlocal voltage signals in the unperturbed superconductor. For this purpose we created a sample that consists of approximately 80 nm wide and 40 nm thick palladium wires which are attached in the center of a 39 μm long aluminum wire of 95 nm width and 85 nm thickness. The aluminum wire has a normal state resistance $R_N = 176\ \Omega$ and a critical temperature $T_c = 1.24$ K. The same critical temperature was obtained in other samples made from the same aluminum source. Contact area and nonlocal measurement configuration are shown in Fig. 5.1. For the resistance measurements I used SR830 lock-in amplifiers by Stanford Research and home-built preamplifiers which are based on the Analog Devices AD624 instrumentation amplifier. A home-built voltage sum box (current summing circuit with an INA 105 operational amplifier) was used to add DC bias and AC excitation signal. The output was converted into a current using a 1 MΩ series resistor. An AC excitation of 100 nA was used in the experiments. The current was injected at one of the contacts and the nonlocal AC voltage signal was recorded as a function of current bias at the detector contacts. A small, amplifier dependent offset was removed from the signal. All measurements were performed at the base temperature of our dilution refrigerator, $T = 15$ mK.

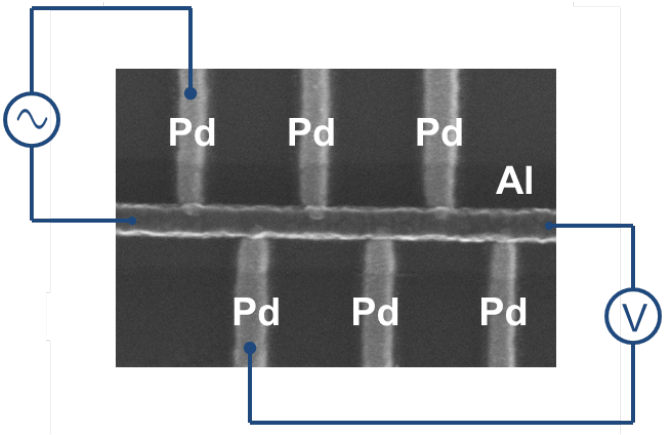

Figure 5.1: A scanning electron micrograph of an Al wire with Pd contacts which are spaced at an interval of 200 nm. The wiring for a nonlocal voltage measurement is sketched in the graph: The excitation current is sent through the injecting contact and extracted at one end of the superconducting wire. The voltage is measured between the detector contact and the other end.

Figure 5.2 shows the nonlocal differential resistance as a function of the distance, d, from the injecting contact. The nonlocal (differential) resistance, R_{NL}, is defined as the nonlocal AC voltage signal, V_{NL}, divided by the AC excitation current, I_{AC}; $R_{NL} = V_{NL}/I_{AC}$. At low current bias we observe a positive nonlocal voltage signal and thus a positive nonlocal resistance in all our NSN devices. This is in agreement with theoretical predictions [93, 94]. Above the critical temperature and when the superconducting wire is driven normal by a large bias current, the nonlocal resistance vanishes. At zero DC bias, it decays exponentially with contact distance. The dashed line in Fig. 5.2 is a fit to the nonlocal resistance formula derived by Golubev et al. [94],

$$R_{NL} = \frac{r_{\xi_S}}{2} \exp\left(-\frac{d}{\xi_S}\right). \tag{5.1}$$

I obtain $\xi_S = 133$ nm as the fit value for the coherence length, and $r_{\xi_S} = 0.488\ \Omega$ for the resistance of a section of length ξ_S of the superconducting wire. A small, constant offset, $R_0 = 8\ \mathrm{m}\Omega$, was introduced to improve the fit. A similar offset was reported in Ref. [5]. Its origin is unclear.

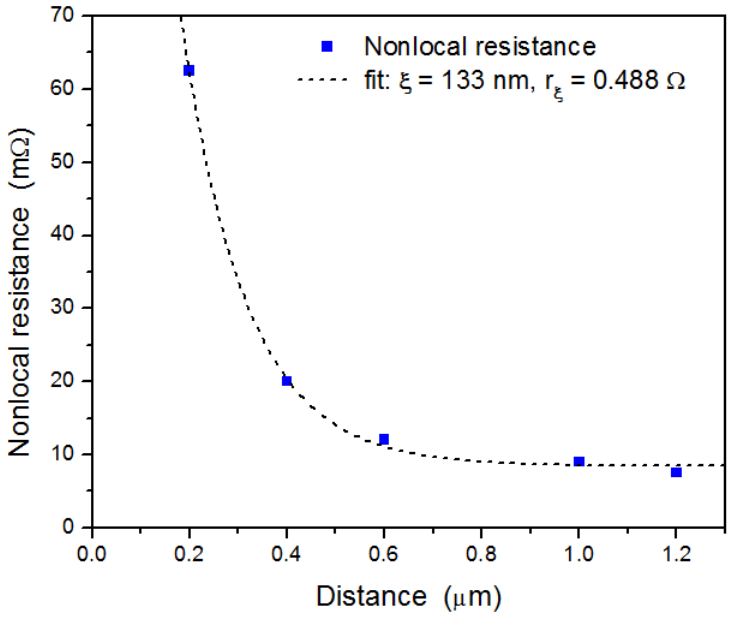

Figure 5.2: Nonlocal resistance at the detector contact as a function of distance from the injecting contact.

Let us compare the fit value with the theoretical value for the coherence length in the superconducting wire: From the Einstein relation for the conductance, $\sigma = e^2 N_F D$, we can calculate the diffusion constant of the superconducting wire, $D = 50\ \mathrm{cm}^2/\mathrm{s}$. Here, I used $N_F = 2.15 \times 10^{47}/\mathrm{J.m}^3$ for the density of states at the Fermi surface of aluminum [132]. The coherence length in the superconducting wire is given by

$\xi = \left(\frac{\hbar D}{\Delta}\right)^{1/2} = 133$ nm, where I assumed $\Delta = 186$ μV for aluminum with $T_c = 1.24$ K. The agreement between the fit value and the theoretical value is excellent and r_{ξ_S} is only somewhat smaller than the resistance of a segment of length ξ of the wire, $r_{seg} = 0.61$ Ω. We conclude that the decay length of the nonlocal voltage signal matches the coherence length of the unperturbed superconductor in our sample. Our signal magnitude is smaller by approximately a factor of 4.6 compared to Ref. [5]. This value also roughly matches an estimate based on the theoretical calculations by Golubev et al. [94]. The inverse proximity effect is not a necessary condition to observe nonlocal transport in superconducting wires.

5.3 Current noise experiments

5.3.1 Sample design and reservoir heating

It was already mentioned that an important part of the work was to find the right design for nonlocal current correlation samples. Several aspects had to be considered: On the technical side, sample fabrication methods, measurement sensitivity, and a limit to how much bias current can be sourced in our measurement setup put constraints on the contact geometry. On the other hand, large reservoirs need to be attached to the normal metal wires. A design with short normal metal wires, which are attached on opposite sides of a mesoscopic superconducting wire, was chosen. This allowed for small contact separations and still left enough space for the reservoirs. Of similar importance is to take into consideration the inverse proximity effect in the contact area and nonequilibrium effects in the superconducting wire. Both are affected by the film-thickness ratio of the materials in the contact region, the contact areas, and the conductance per unit length in the superconducting wire. As the nonlocal subgap transport scales with the inverse of the conductance per unit length, the design must be carefully balanced to observe a large enough signal and – at the same time – be able to study coherent effects within a large enough bias region.

The original sample design (device **D1**) is shown in Figure 5.3. Two copper wires (vertical) connect to an aluminum wire (horizontal). The film thicknesses of copper and aluminum are $d_N = 57$ nm and $d_S = 85$ nm, respectively. The Cu reservoirs are squares with 1 mm side-length. They were deposited in a separate lithography step and are of similar thickness as the Cu wire. For current noise measurements I attached two SQUID resistance bridges with standard resistors $R_{S1} = 0.91$ Ω and $R_{S2} = 0.957$ Ω to contacts **C1** and **C2** in nonlocal configuration (cp. Chapter 4). Current was sourced through **C1** and the resulting bias voltage was measured as a feedback voltage in the resistance bridge circuit. The nonlocal voltage was recorded as feedback voltage in the branch containing **C2**.

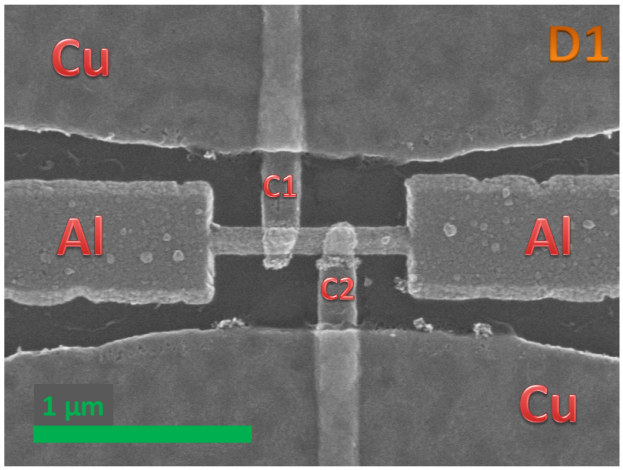

Figure 5.3: A scanning electron micrograph of device **D1**: Two Cu wires (vertical) are attached to an Al wire (horizontal). The center-to-center distance of the contacts is 280 nm.

Nonequilibrium effects and negative dynamic resistance

The dynamic resistance of **C1** and the nonlocal resistance at **C2** are plotted for different measurement temperatures in Figure 5.4 (upper panels). A larger bias range is covered for a measurement at base temperature, $T = 15$ mK (see lower panels of Fig. 5.4). The contact resistance shows the expected re-entrant behavior of a diffusive contact at low bias but also exhibits strong peaks and regions of negative dynamic resistance at higher bias. The first peak appears at a bias voltage $V = 117$ μV where the dynamic resistance abruptly changes sign. The nonlocal resistance is small and positive at low bias. It peaks at the same bias voltage as the resistance curve and then exhibits a first dip with negative values where the dynamic resistance becomes negative. At higher bias peak and dip features in the dynamic resistance and nonlocal resistance coincide although the sign does not necessarily correlate which likely indicates a series of different nonequilibrium states in the mesoscopic superconducting wire.

Regions of negative differential conductance and corresponding negative nonlocal resistance in NSN devices were described theoretically by Bergeret et al. [96]. They model the mesoscopic superconducting region as an island which is coupled to a superconducting and two normal metal reservoirs through (weak) barriers. In this 0-dimensional model the bias voltage reaches a critical value at $V^* \approx 0.8\ \Delta_0/e$ at which point the self-consistent order parameter of the superconductor experiences a sharp drop. Upon increasing the bias voltage further ($V \gtrsim V^*$) the quasiparticle current becomes considerably larger as the superconductor is driven out of equilibrium [96]. In case the coupling to the superconducting reservoir is strong, i.e. most of

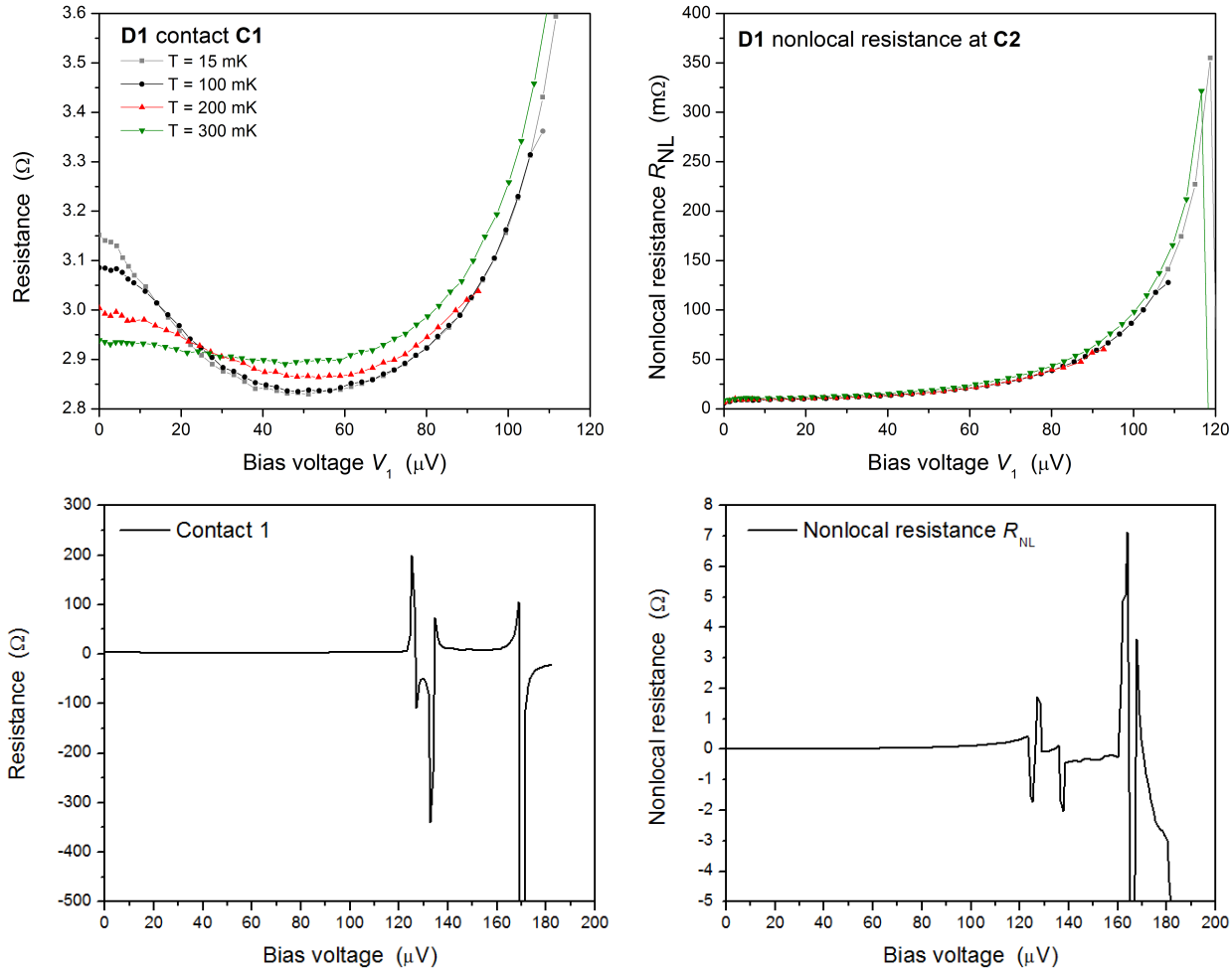

Figure 5.4: Contact resistance and nonlocal resistance of device **D1**: Dynamic resistance of contact **C1** (upper left) and nonlocal resistance (upper right) are plotted as a function of bias voltage at different measurement temperatures T. Dynamic resistance of **C1** (lower left) and nonlocal resistance (lower right) are shown for a larger bias range at temperature $T = 15$ mK. Above a bias voltage $V^* = 89$ μeV the superconducting wire is driven out of equilibrium and jumps in voltage are possible. Despite several attempts the SQUID resistance bridge feedback unlocked for temperatures 200 mK and 300 mK and thus the measurements ended abruptly before the bias sweep was completed.

the current is passed into the superconducting reservoir instead of the second normal electrode, this results in negative differential conductance at the contact. The nonlocal resistance is also negative since it is inversely proportional to the contact resistance of the current injecting contact.

In our device geometry the region of nonequilibrium superconductivity is likely to span across the entire aluminum wire and the inverse proximity effect modulates the pairing potential close to the normal metal contacts. For this region we expect to find similar critical voltage effects: Below the critical value the entire superconducting wire is essentially in equilibrium with an order parameter that varies spatially around the

contact region. When the critical voltage of the contact region is surpassed, the order parameter decreases and a substantial quasiparticle current can flow. The nonequilibrium charge relaxes over a distance Λ^* which is related to inelastic impurity scattering and orbital pair breaking [15] (The gradient in the order parameter provides for additional charge relaxation). The order parameter and the injected quasiparticle charge are coupled by the self-consistency relation in the superconductor. Possibly, more than one solution exists in certain situations (e.g. a related scenario was found in experiments of Ref. [134]). We will take another look at this in the next section.

We expect some similarities between the behavior of our device and the model by Bergeret et al. Although nonequilibrium effects may set in more gradually in the wire geometry, a strong drop in the order parameter is likely to occur when the bias is comparable to the order parameter in the contact region. In the model strong nonequilibrium effects set in around a bias voltage $V^* \approx 0.8\,\Delta/e$, where Δ is the bulk order parameter. We shall replace Δ with the approximate value for the order parameter in the contact region [17], $\Delta^* = \frac{d_S}{d_S+d_N}\Delta_0 \approx 111$ μeV. I this case the critical voltage becomes $V^* = 89$ μV. The value for the bulk order parameter, $\Delta_0 = 186$ μeV, in our calculations was inferred from the critical temperature of the aluminum wire, $T_c = 1.24$ K. In Figure 5.4 we can clearly identify several nonequilibrium states of the superconducting wire but no feature is observed at bias voltage V^*. This indicates that the onset of nonequilibrium effects is indeed more gradual in the wire geometry. When the bias voltage reaches the value of the order parameter in the contact region, Δ^*/e, a quasiparticle current starts to flow along the wire. A negative differential resistance feature is observed at this bias value.

Effective temperature model

The current noise of **C1** as a function of bias voltage is shown in Figure 5.5. The slope of the current noise curve is strongly temperature dependent and steepest for the lowest measurement temperature. In the shot noise regime, current noise only depends on bias current thus the strong temperature dependence which is observed in the experiment is attributed to heating. Limited heat diffusion in the reservoir will result in an elevated reservoir temperature which is experienced by the device. Employing the model for heat diffusion in Chapter 4, we can calculate the effective temperature for a given measurement temperature, T, and bias

voltage, V,

$$T_e = \sqrt{T^2 + \frac{3}{\pi^3}\frac{R_\square}{R}\alpha \ln\left(\frac{\ell_{\mathrm{e-ph}}}{\ell_{\mathrm{e-e}}}\right)\left(\frac{e}{k}\right)^2 V^2}, \tag{5.2}$$

$$\ell_{e-e} = \left[\frac{\sqrt{2}}{k_{\mathrm{B}}}\left(\frac{\hbar}{e}\right)^2 \frac{Dw}{TR_\square^w}\right]^{1/3}, \quad \text{and} \tag{5.3}$$

$$\ell_{e-ph} = \frac{1.31}{\sqrt{\chi T^3}}. \tag{5.4}$$

The scattering parameters in the reservoirs are estimated from Altshuler's formula for ℓ_{e-e} [133] and the formula for the electron-phonon scattering length ℓ_{e-ph} in 1-dimensional wires. Together these relations fix the temperature dependence of the logarithmic cut-off factor. The effect of the reservoir geometry is described by a dimensionless prefactor, α, which is of order 1. Other sample dependent parameters are the ratio of the resistance per square of the reservoir to the sample resistance, $R_\square/R = 0.46$, the resistance per square of the copper wire, $R_\square^w = 1.44$, the diffusion constant of the copper wire, $D = 30$ cm^2/s, and the wire width, $w = 170$ nm. The value $\chi = 8.9 \times 10^9$ m$^{-2} \cdot$ K^{-3} is taken from Ref. [61].

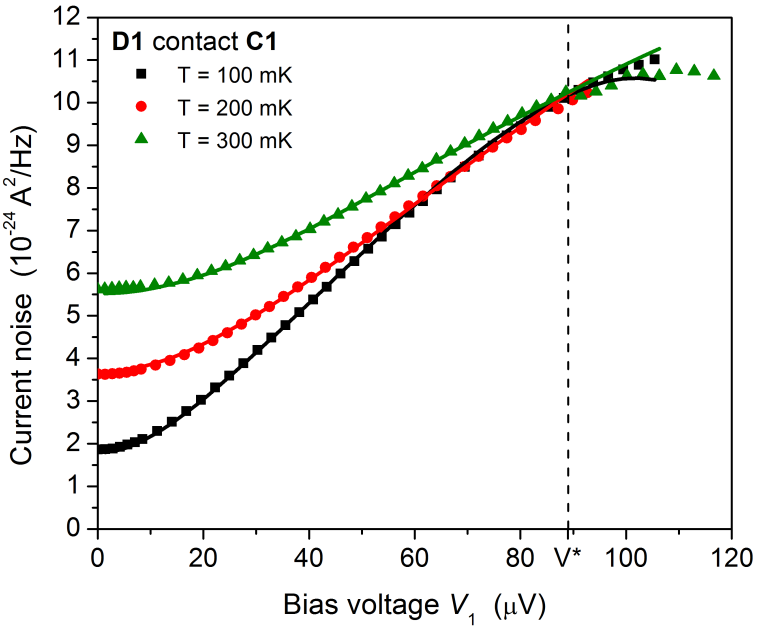

Figure 5.5: Current noise in **C1** as a function of bias voltage: Symbols are measured data and solid lines are plots of the result of the shot noise formula by Nagaev and Büttiker, Eqn. 2.66, using the the effective temperature T_e and the parameters in Table 5.1.

geometry factor α	contact resistance R	effective energy Δ'
0.5	$R(V)$ (see text)	150 μeV
0.5	3 Ω	150 μeV
0.5	3 Ω	110 μeV

Table 5.1: Parameters for modeling the current noise of **C1** based on Eqn. 2.66 and the effective reservoir temperature in Eqn. 5.2. An effective energy scale Δ' is used to replace the reservoir order parameter Δ of the original theory.

Modified shot noise formula

In the presence of reservoir heating it is not clear whether we actually observe the shot noise signal of a diffusive NS contact. We would like to model the shot noise of the device for the effective temperature that we derived above. The model is required to cover a large bias range for reasonable accuracy. In Chapter 2 we discussed the work by Nagaev and Büttiker. Using the Boltzmann-Langevin approach they derived a shot noise formula for the regime of incoherent transport in a diffusive normal metal wire that is attached to a superconducting reservoir. It is valid for the whole bias range. The boundary condition for the (even part) of the distribution function is chosen such that no energy current is flowing into the reservoir below the energy of the reservoir pairing potential, Δ. For our purpose, we shall simply assume that an effective energy scale Δ' exists below which quasiparticle transport is irrelevant and no energy current flows in the superconducting wire. At the very lowest temperatures, the model will not be accurate as the proximity effect changes the density of states in the normal metal wire considerably. We can partially compensate for it by using the dynamic resistance of the contact, $R(V)$, instead of the normal state resistance in Formula 2.66. We will do so for $T = 100$ mK as the Thouless energy $E_C = \frac{\hbar D}{L^2} \approx 15$ μeV is larger than $k_\mathrm{B}T$ for this temperature. It still remains to determine the geometric prefactor α in the temperature formula, Eqn. 5.2, and the effective energy Δ' for each temperature. We can adjust these to fit the data in Figure 5.5 reasonably well (solid lines in the plot). The parameters are given in Table 5.1. Here, it should be noted that, of course, the value for α must be the same for all temperatures. The values of Δ' can be determined with an accuracy of about ± 5 μeV and are somewhat smaller than the typical bulk pairing potential of aluminum, $\Delta_0 \approx 180$ μeV. This may be a sign that the inverse proximity effect spreads out along the entire superconducting wire.

The bias region above the critical voltage V^* of the contact region cannot be captured with our simple model. At this point a larger portion of the superconducting wire is driven out of equilibrium. The resulting quasiparticle current allows to transport heat along the wire. As a result, the current noise is stagnant until the quasiparticle energy becomes comparable to Δ^*, the order parameter in the contact region. Beyond this point the current noise increases steeply and the whole wire is driven into a nonequilibrium state. We shall

study this effect in greater detail in another sample (device **D2**). Meanwhile, we conclude that it is indeed possible to model the current noise in device **D1** by adding a few modifications to the Nagaev-Büttiker shot noise formula for a diffusive NS contact. The problem of reservoir heating can be avoided entirely by increasing the reservoir conductance, e.g. by depositing a thicker film for the normal metal reservoirs. This was done for the remaining samples which will be presented below.

5.3.2 Nonequilibrium states in the superconducting wire

The issue of nonequilibrium superconductivity in the mesoscopic wire warrants a more detailed study. We intended to minimize the inverse proximity effect by using small interface areas and a favorable thickness ratio between superconductor and normal metal films. This was achieved by changing the aspect ratio of the aluminum wire while – at the same time – keeping the cross-sectional area approximately the same. The wire resistance was increased by depositing gold films of only 30 nm thickness for the injecting contacts. Gold was used as it does not oxidize and thus larger coherence lengths can be achieved. The reservoirs of this sample were designed as squares with 1 mm side-length and 200 nm thickness to avoid the reservoir heating effects which we previously encountered. They were deposited from the same gold source as the wires. The sample was measured using two SQUID resistance bridge circuits with standard resistors $R_{S1} = 0.985\ \Omega$ and $R_{S2} = 1.060\ \Omega$ in nonlocal configuration.

Constriction model and numerical calculations of the contact resistance

The resistance of contact **C1** and the nonlocal resistance in the branch of contact **C2** are plotted in Fig. 5.7. The data show some striking features: Firstly, the re-entrant resistance effect is absent. Even at the lowest temperature the zero-bias resistance does not approach the normal state resistance, $R_N \approx 11.4\ \Omega$, of the wire. Instead, the resistance flattens out at some lower value for $eV \leq 5E_C \approx 25\ \mu$eV. Here, the Thouless energy is given by $E_C \approx 5\ \mu$eV. It was determined using the diffusion constant in the gold film, $D = 114\ \mathrm{cm}^2\mathrm{s}$, which was measured separately. Secondly, the resistance at higher bias is significantly lower compared to a diffusive NS contact with superconducting order parameter $\Delta \approx 180\ \mu$eV (see the quasi-classical solution (gray $\bigcirc$) which is plotted in Fig. 5.8). Thirdly, the nonlocal resistance scales linearly with the bias voltage at **C1** above the transition.

By closely inspecting the scanning electron micrographs of device **D2**, we can identify a possible reason for the unexpected shape of the resistance data. The wire narrows considerably close to the interface and appears to be thinner because of surface etching that was performed before the aluminum deposition. We

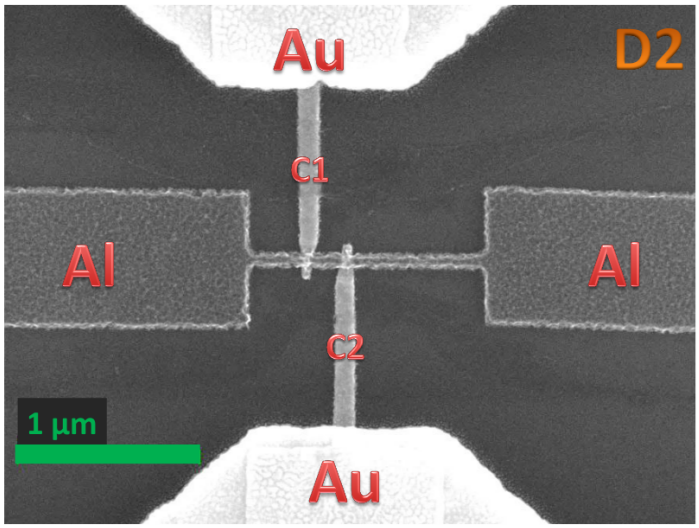

Figure 5.6: A scanning electron micrograph of device **D2**: Two Au wires (vertical) are attached to an Al wire (horizontal). The center-to-center distance of the contacts is 216 nm. The left and right section of the aluminum wire are, respectively, 315 nm and 765 nm long. The aluminum wire is $d_S = 120$ nm tick and the copper wire thickness is $d_N = 30$ nm.

can use this insight to define a model for the contact by adding a constriction region next to the NS interface. The contact geometry for the model calculations is sketched in Fig. 5.8 (right panel) alongside a table of parameters. The relative conductances are inferred from resistance measurements on gold and aluminum wires and from the geometry and approximate thickness, $\tilde{d}_N \approx 20$ nm, of the gold film in the etched region. In the contact region the pairing strength in the superconducting wire is assumed to increase linearly from $\lambda' = \frac{d_S}{d_S+\tilde{d}_N}\lambda_0 = 0.86\lambda_0$ to its bulk value, λ_0, within a distance of the coherence length from the interface. The pairing strength λ_0 is calculated from the Debye temperature of bulk aluminum $T_{\mathrm{Debye}} = 398$ K [135] using

$$\lambda_0 = \frac{1}{\cosh^{-1}\left(\frac{k_B T_{\mathrm{Debye}}}{\Delta}\right)}.$$

I assumed a bulk order parameter of $\Delta = 180$ μeV throughout. There are no free parameters in this model.

Numerical calculations of the contact resistance were performed using the `USADEL1` code by Pauli Virtanen [26, 33]. It solves the quasi-classical Keldysh-Usadel equations (see Chapter 2) on a network of 1-dimensional wires. The results are compared to the resistance of **C1** in Figure 5.8. The solution for a simple diffusive wire without constriction (gray ○) shows poor agreement with the data whereas the constric-

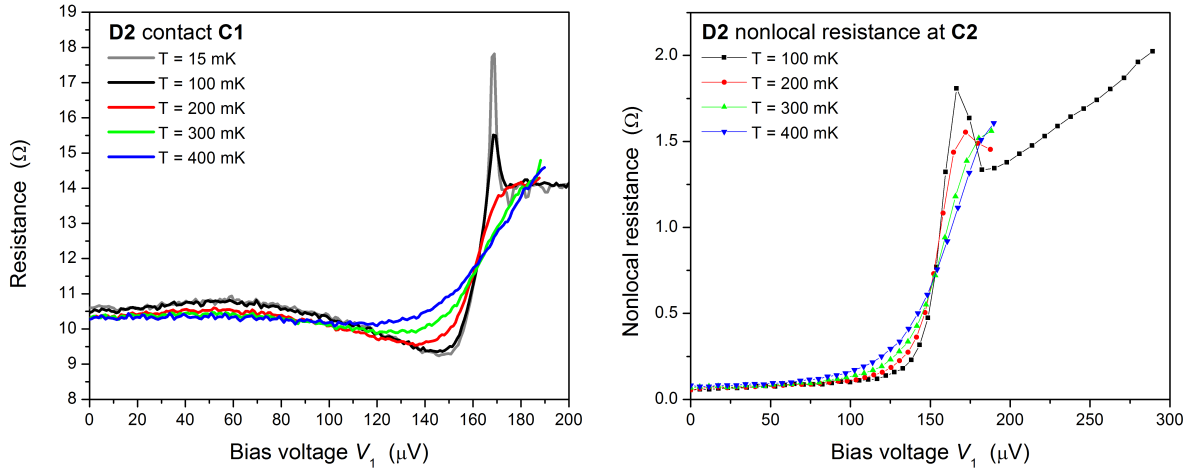

Figure 5.7: Dynamic resistance of contact C1 and nonlocal resistance at **C2**: The resistance of **C1** does not exhibit re-entrant behavior (left panel). Instead a 'hump'-like feature is observed (left panel). The nonlocal resistance is small and increases proximately linearly with bias voltage at low bias (right panel). Above the transition we see a large nonlocal signal which, again, scales linearly.

tion model (blue △) reproduces the resistance dip at higher bias voltages qualitatively. Excellent qualitative agreement is found by solving the equations in the superconducting wire self-consistently (red ▽). However, the low bias behavior is not reproduced correctly by either model. All models predict re-entrant behavior for the contact resistance with a zero-bias value $R(0) = 11.75\ \Omega$. This value is in good agreement with the effective contact resistance of a diffusive NS contact, $R_{NS} \approx R_N + R_{\xi_S} = 1.72\ \Omega$, where the resistance of a portion of the superconducting wire of length $\xi_S \approx 207$ nm is included; here, $R_{\xi_S} = 0.32\ \Omega$. This takes into consideration that quasiparticles and electrical field penetrate into the superconductor over a length comparable to the coherence length, ξ_S, see reference [26].

The re-entrance effect is cause by an exact cancellation between pair-enhanced transport and the reduction of normal transport due to the decrease in the density of states. We may speculate why it is absent in this device. The constriction region is much shorter than the coherence length in the gold wire, $L_T = \sqrt{\frac{\hbar D}{k_B T}} \approx$ 270 nm (for $T = 100$ mK) and of the same order of magnitude as the mean free path, $\ell \approx 15$ nm. Therefore coherent scattering between the point contact of diameter $d \ll \xi_S$ with the superconductor and the disorder potential in the constriction region may occur. A similar effect which enhances the low bias conductance was observed in NS tunnel contacts [100, 101], where the coherent disorder–back-scattering increased the tunneling probability across the interface. Since coherent scattering is not taken into account in the Keldysh-Usadel formalism, such effects are not covered by the numerical calculations.

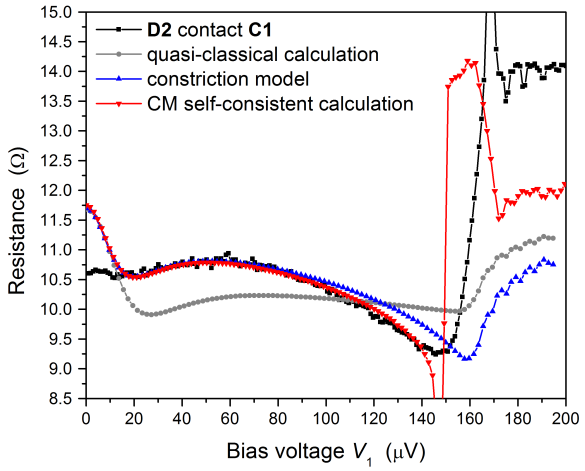

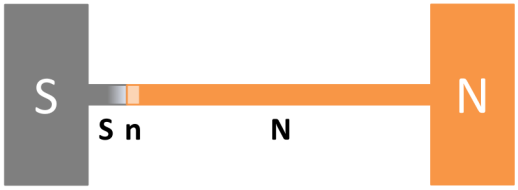

	length (nm)	relative conductance
S	300	9
n	100	0.333
N	900	1

Figure 5.8: Three different models for the dynamic resistance of contact **C1**: The resistance data for **C1** was measured at the base temperature of our dilution refrigerator, $T = 15$ mK (black □). The quasi-classical calculation (gray ○) uses the Keldysh-Usadel equations for a diffusive wire without a constriction and shows poor agreement with the data. The shape of the data at high voltage bias is replicated by a model with a short constriction region at the interface between superconductor and diffusive wire (blue △). A sketch of the model geometry and the parameters of the model are displayed in the right panel of the figure. Excellent qualitative agreement is obtained by solving the equations in the superconductor self-consistently (red ▽). For all models a strong re-entrance effect is seen at low bias which is not present in the data.

Shot noise and nonequilibrium effects

As I mentioned earlier, the device geometry of **D2** was designed to minimize the inverse proximity effect in the superconducting wire and study the onset of nonequilibrium effects. The film thickness of the gold film in the contact area is $d_N \approx 20$ nm and the superconducting wire thickness is $d_S = 120$ nm. Thus an estimate for the order parameter in the contact region is given by $\Delta^* = \frac{d_S}{d_S+d_N}\Delta = 154$ μeV. We assume a pairing potential of $\Delta = 180$ μeV and do not expect the inverse proximity region to extend far into the wire because of the point contact geometry between normal metal and superconductor. Thus the critical voltage in the device should be related to Δ and $V^* = 0.8\Delta = 144$ μeV. This value is reproduced in the self-consistent calculation of Fig. 5.8 which implicitly assumes point contacts between normal metal and superconducting wires.

The current noise of contact **C1** is shown in Fig. 5.9. As we did previously, we will base our analysis on the formula for incoherent shot noise in a diffusive wire, Eqn. 2.66. The Thouless energy of the wire is smaller than the thermal energy, $E_C \approx 5$ μeV $< k_B T$, for all measurement temperatures, T. The solid lines in Fig. 5.9 are solutions of the Nagaev-Büttiker shot noise formula, where I replaced the reservoir order parameter Δ with an effective energy scale for heat transport $\Delta' = \Delta^*$. Again, we find good agreement

below the critical voltage V^* of the superconducting wire. Heating is observed only for $T = 100$ mK in the regime of higher bias.

We can also study the bias dependence of *nonlocal* current noise at **C2** and the cross-correlation between the current noise signals, see Fig. 5.9 (right panel). Whereas the current noise in **C1** increases linearly with bias, the nonlocal current noise in **C2** rises only slowly below the transition at Δ^*/e. Still, the amount of current noise is too large to be caused by the nonlocal voltage that is measured at **C2** and the current correlation is vanishingly small. We will attempt to establish a connection between the nonlocal current noise and subgap heat transport later in this chapter. In the nonequilibrium regime above the transition the current noise in **C1** increases steeply. On the other hand, the current noise at **C2** scales linearly with the bias at **C1** and a Fano factor of $F_{21} = \frac{1}{2e}\frac{\partial S_2}{\partial I_{x1}} = \frac{1}{3}$ is observed. In the same bias region the nonlocal resistance also increases linearly with bias voltage, see Fig. 5.7 (right panel), but only a small fraction of the current fluctuations are correlated. The current noise enhancement is likely a consequence of nonequilibrium superconductivity in the mesoscopic superconducting wire. To the best of my knowledge, current noise in this regime has not been studied before. We may consider it as an interesting topic for future study.

Nonlocal measurement of charge imbalance effects

Another interesting observation related to nonequilibrium superconductivity in the mesoscopic wire is presented Fig. 5.10. We measured the resistance of the contact and a part of the superconducting wire in

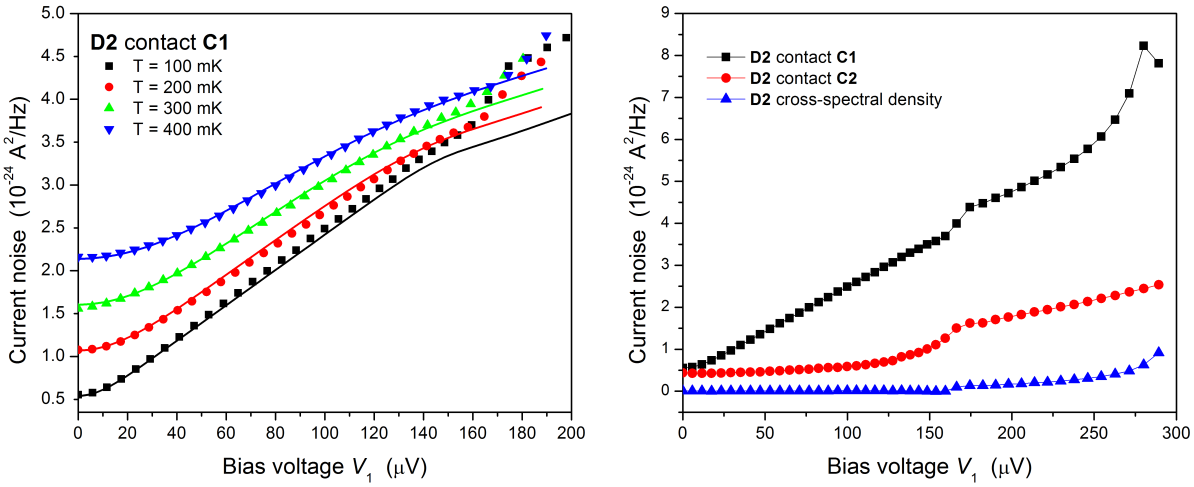

Figure 5.9: Shot noise data of device **D2**: The shot noise of **C1** is graphed for different measurement temperatures T (left panel). Solid lines are solutions of to the Nagaev-Büttiker formula, Eqn. 2.66. Current noise in **C1**, **C2**, and current cross-correlation are compared for a measurement at temperature $T = 100$ mK (right panel). The nonlocal current noise at **C2** increases slowly below the transition but scales linearly with the applied bias voltage at **C1** above. Only a fraction of the current is correlated.

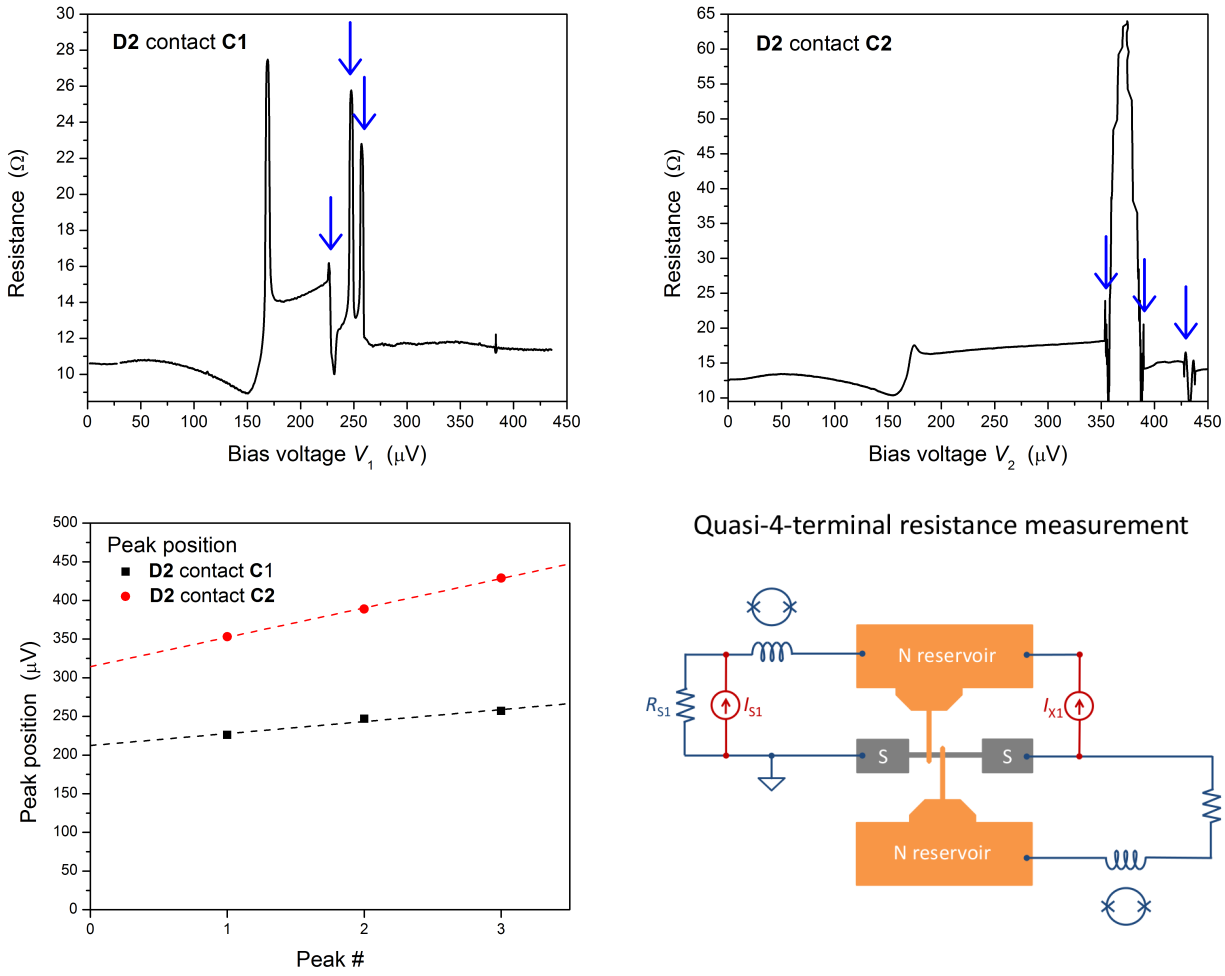

Figure 5.10: Dynamic resistance of contact **C1** and contact **C2** of device **D2**: The dynamic resistance of **C1** (upper left) and **C2** (upper right) are plotted for a measurement in quasi-4-terminal configuration (see lower right panel). A large charge imbalance signal is observed above the transition voltage Δ^*/e. Additional peaks and switching features appear in the resistance plots. The voltage values at which the features are observed are graphed in the lower left panel.

"quasi-4-terminal" geometry, Fig. 5.10 (lower right panel). Unlike in studies of local charge imbalance in the literature, we measure voltage along the normal metal contact and a portion of the superconducting wire that is not in the current path. Above the transition voltage Δ^*/e we observe a strong charge imbalance signal in Fig. 5.10 (upper panels). The bias region over which it extends roughly scales with the inverse of the length of the current path in the mesoscopic superconducting wire. Additionally, several sharp peaks and switching features appear, which are marked by blue arrows in Fig. 5.10. The voltages at which the features occur are graphed in Fig. 5.10 (lower left panel) and they appear to be scaling. However, the origin of the peaks is unclear. Typical charge imbalance lengths, Λ_{Q^*}, in mesoscopic aluminum wires are found to be between 1 to 10 μm long [5, 6, 136]. The injection efficiency is energy dependent and the effective

injection volume, Ω, in a wire can be estimated by $\Omega = A \times 2\Lambda_{Q^*}$, where A is the cross section area of the wire [136]. The observed peaks and switching features may, therefore, result from the redistribution of charge along the wire due to boundary effects. An indication for this could be that the ratio of peak spacing between the measurements in the two configurations shown in Fig. 5.10 matches the length ratio of the left and right portions of the superconducting wire.

5.3.3 Nonlocal current correlations

We shall now focus on the main body of results regarding subgap nonlocal transport, current noise and current correlations. We commence with a presentation of the experiments on devices **D3** and **D4** and will refer back to measurements on **D1** and **D2**, as needed.

Devices **D3** and **D4** were fabricated simultaneously to achieve similar materials and interface parameters. Using the same methodology we developed in the last sections, we will analyze shot noise and contact resistance to assert that we are in the regime of diffusive transport and intermediate barrier transparencies. We will then proceed to discuss nonlocal transport and current correlations, which will be compared with available theoretical predictions on devices very similar to ours. Temperature and bias dependence of the nonlocal signals will be presented. Additionally, I will try to quantify the uncorrelated part of nonlocal current noise which has not been given attention in the literature.

Scanning electron micrographs of devices **D3** and **D4** are shown in Fig. 5.11. To minimize the distance between the contacts, the copper wires were attached on opposite sides of the aluminum wire. This way we obtained approximate contact separations of $d_3 \approx \frac{\xi_S}{2}$ for **D3** and $d_4 \approx \xi_S$ for **D4**, where $\xi_S \approx 200$ nm is the coherence length in the superconductor. The copper wires are 200 nm wide and the wire lengths are $l_3 = 800$ nm and $l_4 = 680$ nm, respectively, for the two devices. The copper film-thickness is $d_N = 50$ nm. The wires were deposited in the same lithography step as the 200 nm thick copper reservoirs using the shadow-angle method. The aluminum wire is approximately 185 nm wide and the nominal thickness of the superconducting film is $d_S = 150$ nm. The aluminum material was evaporated at a high rate to achieve a clean deposition. In this case the open angle for the deposition direction is large resulting in deposition of material in the undercut region. The wires bevel at the edges and the thickness in the interface regions is not uniform. Both devices were measured using two SQUID resistance bridges with standard resistors $R_{S1} = 0.63\ \Omega$ and $R_{S2} = 0.61\ \Omega$ in nonlocal configuration.

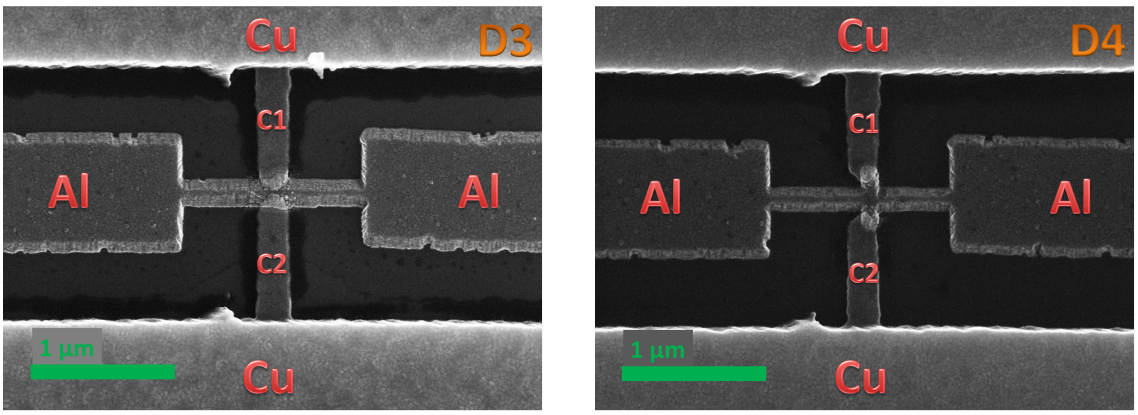

Figure 5.11: Scanning electron micrographs of device **D3** and **D4**. Two copper wires (vertical) are attached on opposite sides of a superconducting wire (horizontal).

Contact characterization

The dynamic resistances of the individual contacts of **D3** and **D4** are displayed in Fig. 5.12. All contacts exhibit the re-entrant resistance effect with a zero-bias resistance within 5% of the normal state value. Whereas the low bias limit shows similar behavior for all contacts, at higher bias an asymmetry is revealed between the contacts **C1** and **C2** of both devices. Two possible explanations come to mind: Firstly, the difference may come from a small dissimilarity in the morphology of the contacts, e.g. the surface cleaning was not performed uniformly over the interface regions of both contacts because of a slight misalignment of the device with respect to the Kaufmann sputtering source ("ion mill"). Since the magnitude of order parameter and chemical potential in the superconductor are established self-consistently in the interface region, chemical potential and quasiparticle diffusion pattern may deviate substantially at higher bias. Secondly, the device ground is located in the bridge circuit of **C1** whereas the second bridge circuit (encompassing **C2**) is connected to ground only through the superconducting wire (cp. Fig. 4.4 in Chapter 4). Thus the boundary conditions for the chemical potential at the two ends of the mesoscopic superconducting wire are different [137] which may also change the distribution of quasiparticle charge and the chemical potential in the contact region resulting in different resistances measured at the two contacts.

Unlike in device **D2** the resistance of the interface region and the wire resistance are of similar magnitude thus effects in the boundary region will alter the contact resistance distinctly. The order parameter and chemical potential need to be solved self-consistently in the whole scattering region and the superconducting wire. However, the dimensions of the superconducting wire are chosen large enough such that the individual contacts may not feel changes in the quasiparticle diffusion pattern around the other contact. Therefore

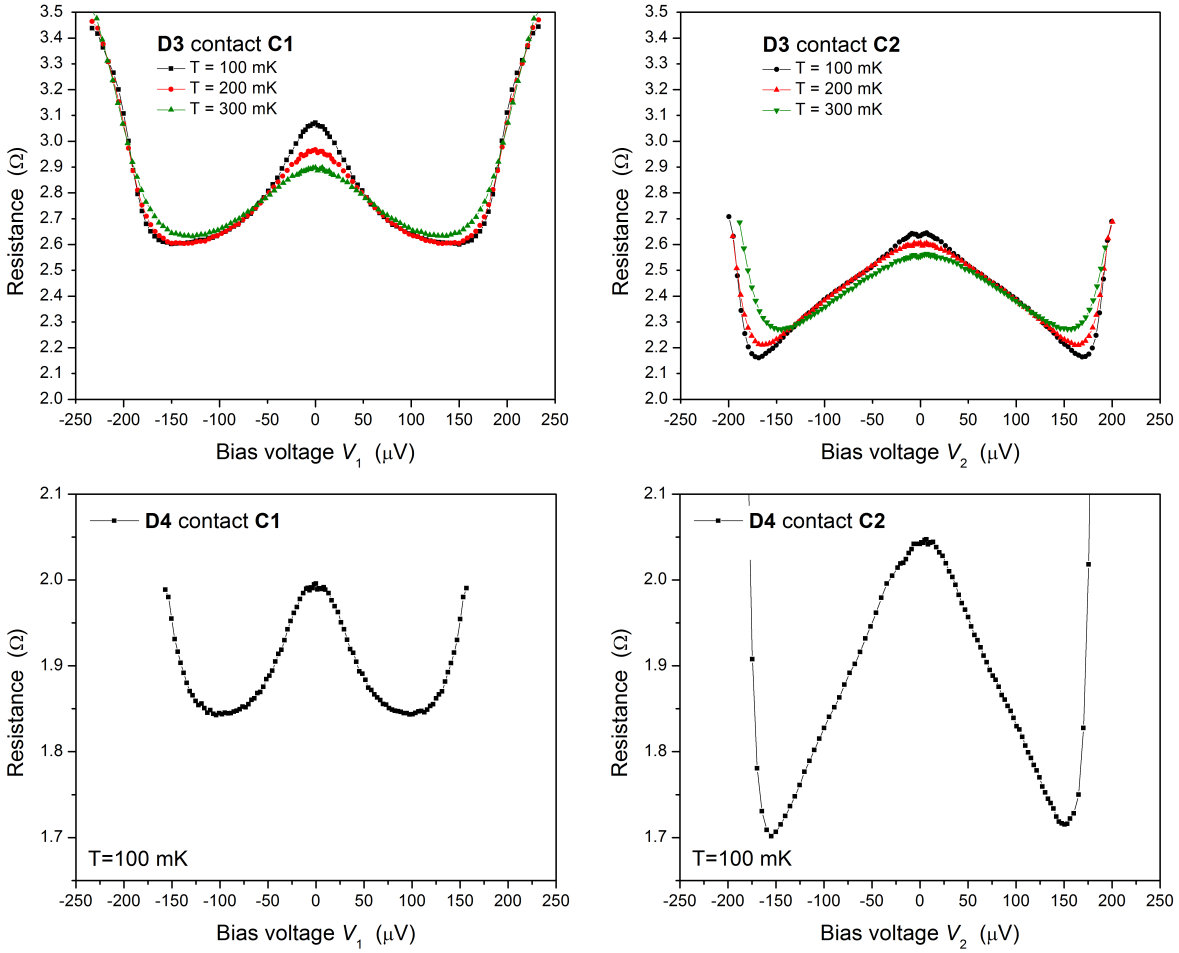

Figure 5.12: Dynamic resistances of devices **D3** and **D4**: The dynamic resistances of contacts **C1** and **C2** show qualitatively different behavior at higher bias.

signals which are measured in nonlocal configuration may not be affected. Detailed numerical modeling of the interface regions is difficult and was not attempted. Instead, I tried to gain some insight by comparing the resistance data in the low bias regime to a simple numerical model based on the Keldysh-Usadel equations for a diffusive NS contact with arbitrary interface barrier. For this purpose I developed a Python-code based on the formalism discussed in Ref. [28] and implemented inelastic and spin-flip scattering for the problem (cp. Chapter 2 and Appendix A). The numerical solutions are found using the `COLNEW` algorithm which is available as `scikits`-package for Python [31].

In Fig. 5.13 the numerical calculations are compared to contact resistance data for a sample temperature of $T = 100$ mK. The dynamic resistance of contacts **C2** is well described by the model up to bias voltages $V \approx \Delta/e$. The barrier region is assumed to contribute 1/4 to the total resistance of the contact and barrier strengths of $Z \approx 0.4$ correspond to an intermediate interface transparency of $T = 0.86$. The Thouless

energy parameters in the numerical calculations were chosen around 10 μeV and thus close to the estimated values based on a measurement of the diffusion constant in the copper material. Spin-flip scattering with a scattering length of $L_{sf} \sim 400$ nm was introduced. Similar values were obtained for spin-flip lengths in copper wires in the experiments by Poli on lateral spin-valves [138]. Spin-flip scattering in copper devices may be attributed to surface oxidation during sample fabrication.

The shapes of the resistance curves of contacts **C1** cannot be reproduced with the simple model. Assuming the deviations are due to a local suppression of the order parameter in the contact region at higher bias, we may fit the low bias data and extract parameters. For contact **C1** of device **C4** we find similar values for barrier resistance and Z-parameter compared to the other contact of the same device. The spin-flip parameter cannot be determined with a fit to just the low energy data and should be disregarded. The fit

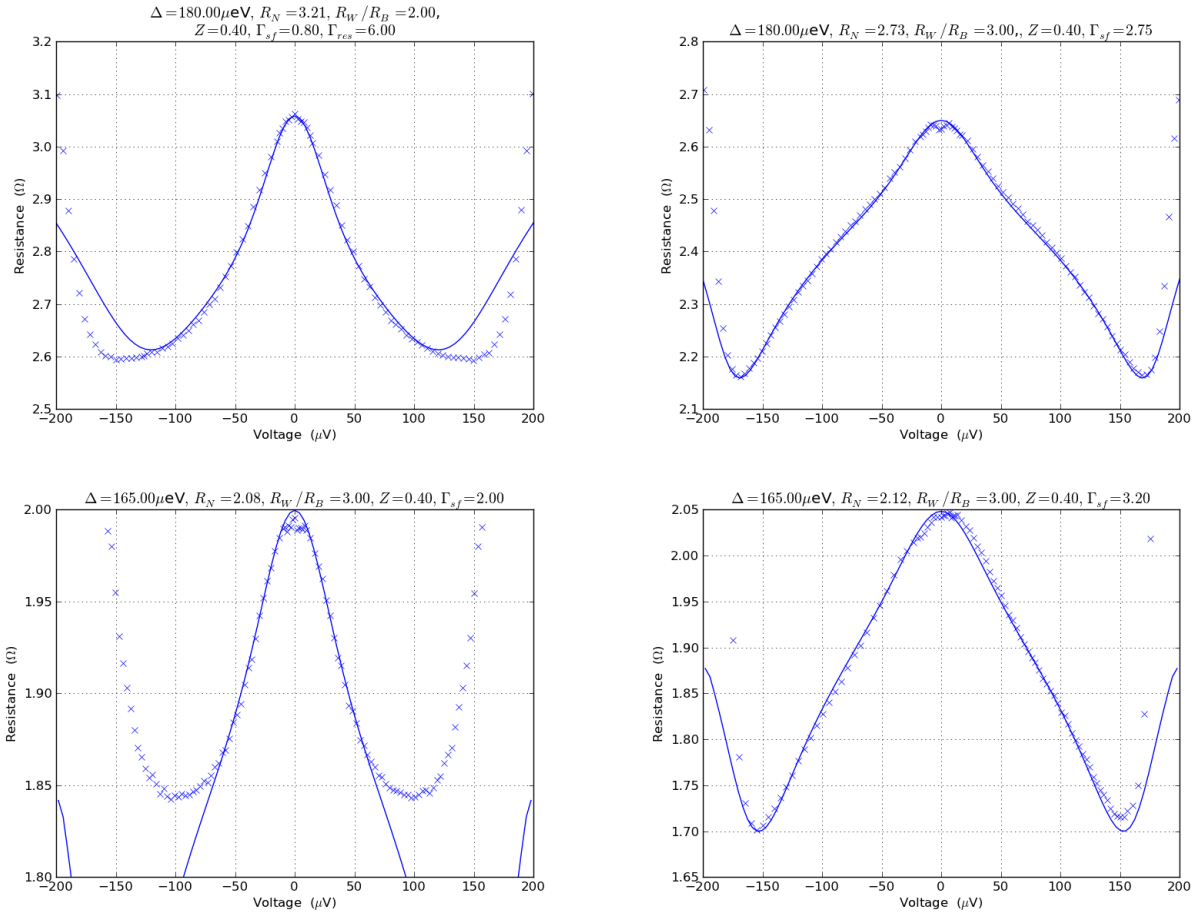

Figure 5.13: Dynamical resistance of both contacts of devices **D3** and **D4** and numerical results at temperature $T = 100$ mK: Numerical calculations (solid lines) agree well with the data ($\times$) of contacts **C2** but the shapes of the resistance curves of contacts **C1** cannot be reproduced with the model.

parameters of contact **C1** of device **D3** show a somewhat larger resistance contribution from the barrier region. Given the overall larger resistance of this contact, we extract identical wire resistances for both contacts of the device which indicates that the additional resistance is in the barrier region of **C1**. I achieved a fit over a somewhat larger bias region by introducing an additional parameter for the broadening of the density of states in the superconducting reservoir.

Shot noise and contact transparency

A difference in the characteristics of contacts **C1** and **C2** can also be seen in the shot noise. The differential Fano factors $|F_1| = \frac{1}{2e}|\frac{\partial S_1}{\partial I_{x1}}|$ and $|F_2| = \frac{1}{2e}|\frac{\partial S_2}{\partial I_{x2}}|$ are graphed in Fig. 5.14. We observe shot noise suppression with Fano factors of approximately 2/3. This is in agreement with the predictions of Eqn. 2.68 for incoherent shot noise in diffusive NS contacts with a barrier parameter $Z \approx 0.4$. A graphical representation for the

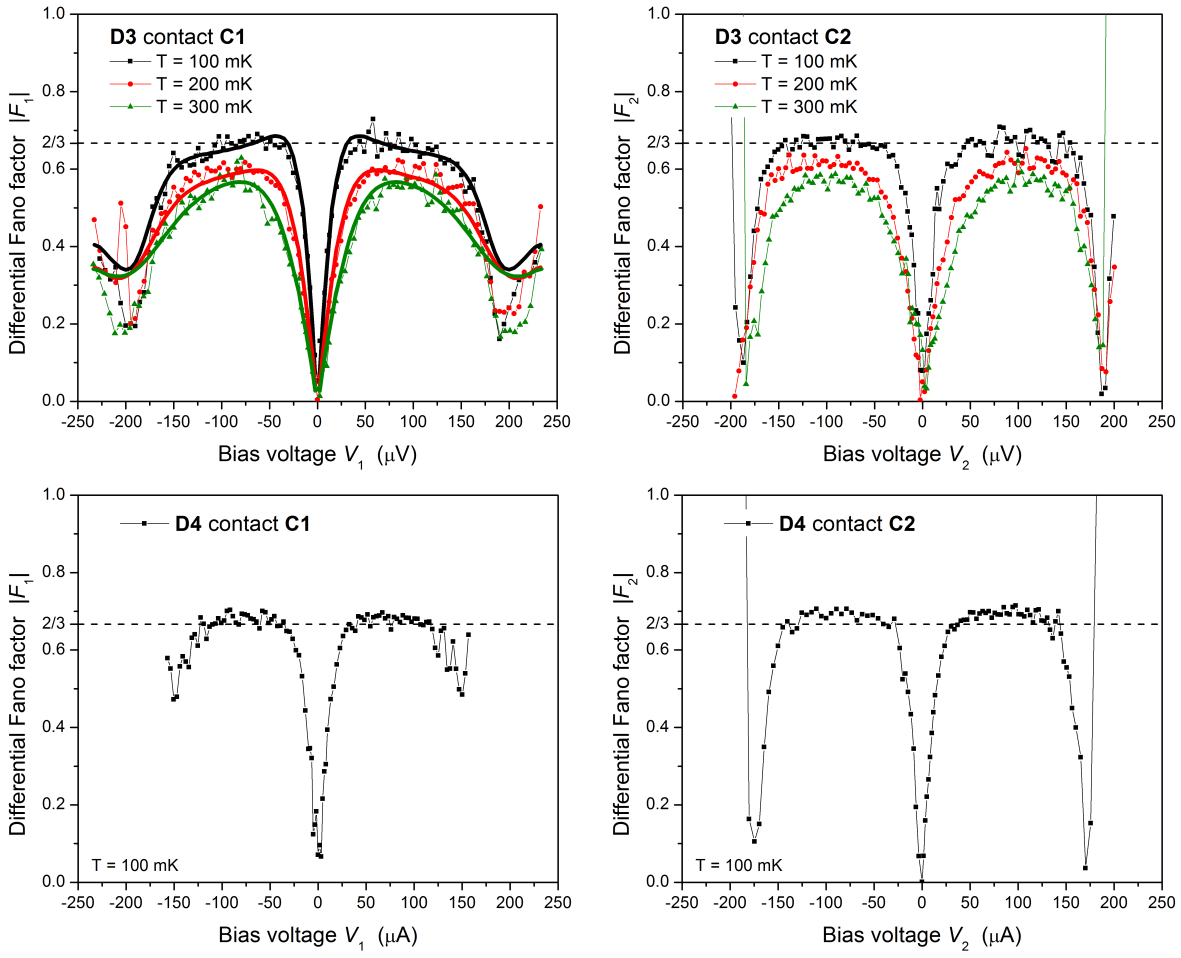

Figure 5.14: Differential Fano factors $|F_1|$ and $|F_2|$ for devices **D3** and **D4**. To illustrate the temperature dependence of the differential Fano factors I plotted the solutions of the Nagaev-Büttiker shot noise formula, Eqn. 2.66, as solid lines for contact **C1** of device **D3** (upper left).

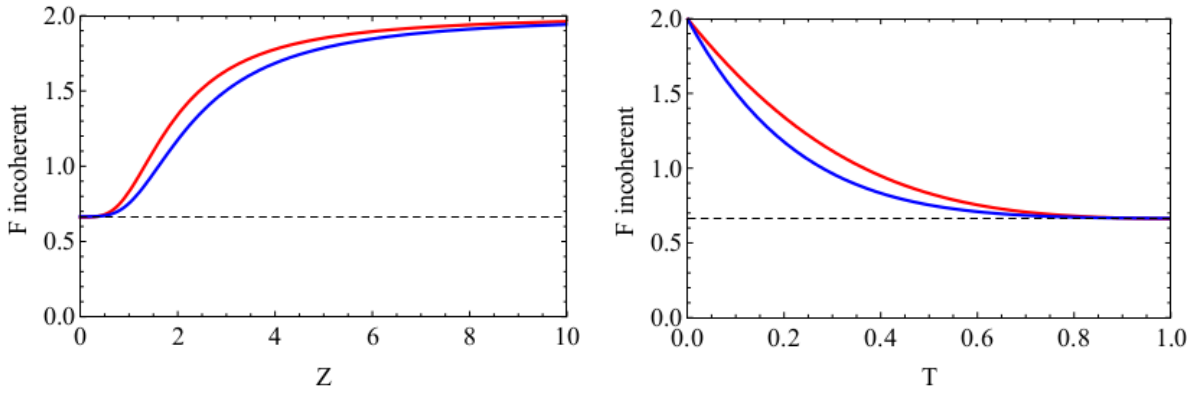

Figure 5.15: The Fano factor for incoherent shot noise in a diffusive NS contact with barrier: The Fano factor is plotted as a function of barrier strength Z (left) and barrier transmission T (right). The two curves correspond to different ratios of wire resistance to boundary resistance: $R_W/R_B = 2$ (red) and $R_W/R_B = 3$ (blue). A significant deviation of the shot noise suppression factor can only be observed for $Z > 0.5$ or $T < 0.8$, respectively.

relevant parameter range is shown in Fig. 5.15.

Regions of full shot noise extend to different bias values in the two contacts: For contacts **C1** the differential Fano factor starts to decrease around $V_1 \approx 110 - 120$ μV whereas contacts **C2** maintain full shot noise up to $V_2 \approx 145$ μV. These values roughly correspond to the lower and upper bounds for the critical voltages for the onset of quasiparticle transport, $V_1^* = 0.8\frac{\Delta^*}{e} = 108$ μV and $V_2^* = 0.8\frac{\Delta}{e} = 144$ μV. The order parameter in the contact region is estimated to be $\Delta^* = \frac{d_S}{d_S+d_N}\Delta = 135$ μeV and $\Delta = 180$ μeV.

Nonlocal resistance and nonlocal current noise

Nonlocal resistance data for measurements at $T = 100$ mK are shown in Fig. 5.16. Both measurement configurations are displayed, i.e. with **C1** as injecting contact and **C2** as detector and *vice versa*. As expected, the nonlocal voltage signals are two orders of magnitude smaller than the bias voltages. In the subgap regime the nonlocal resistance increases only slowly. Despite considerable differences in the behavior of the injector contacts the nonlocal resistance is (nearly) identical for both configurations. Differences are clearly visible only at large bias, $V \gtrsim 110$ μeV.

This is in stark contrast to the change in nonlocal current noise at the detector contact which is of similar magnitude as the shot noise signal at the injector (see Fig. 5.17). Only a small portion of the current fluctuations are correlated in the subgap bias regime, e.g. see Fig. 5.9(right panel). The additional uncorrelated current noise can be interpreted as an increase in the average temperature of the normal metal wire (cp. Chapter 2). Unlike Ref. [47] we may rule out substrate heating as the source of the temperature

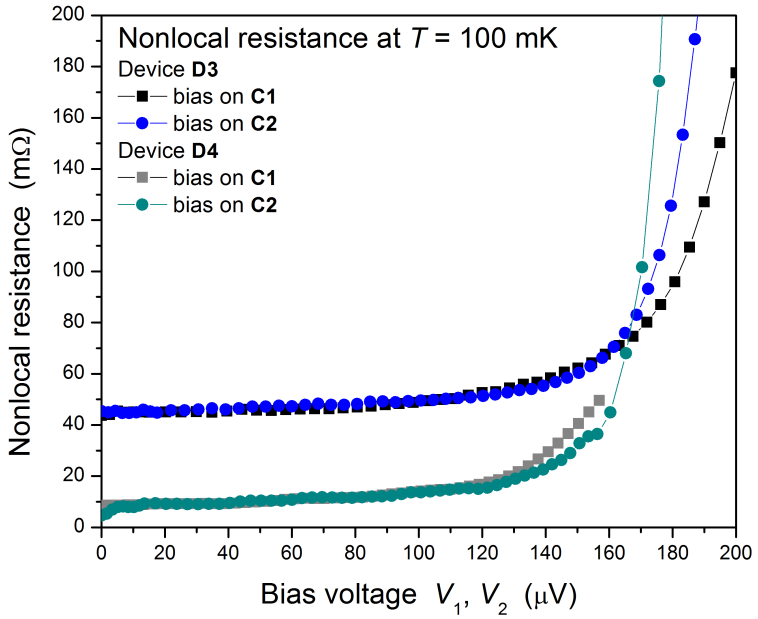

Figure 5.16: Nonlocal resistance of **D3** and **D4**: The nonlocal resistance is measured in both configurations, with **C1** as injecting contact and **C2** as detector and *vice versa*. There is no significant difference between the two configurations at low bias. The contact separations are $d_3 \approx \xi_S/2$ for **D3** and $d_4 \approx \xi_S$ for **D4**.

increase because the dissipated power in device **D2** is ten times smaller compared to **D3** and **D4**, yet the change in nonlocal current noise is of the same magnitude.

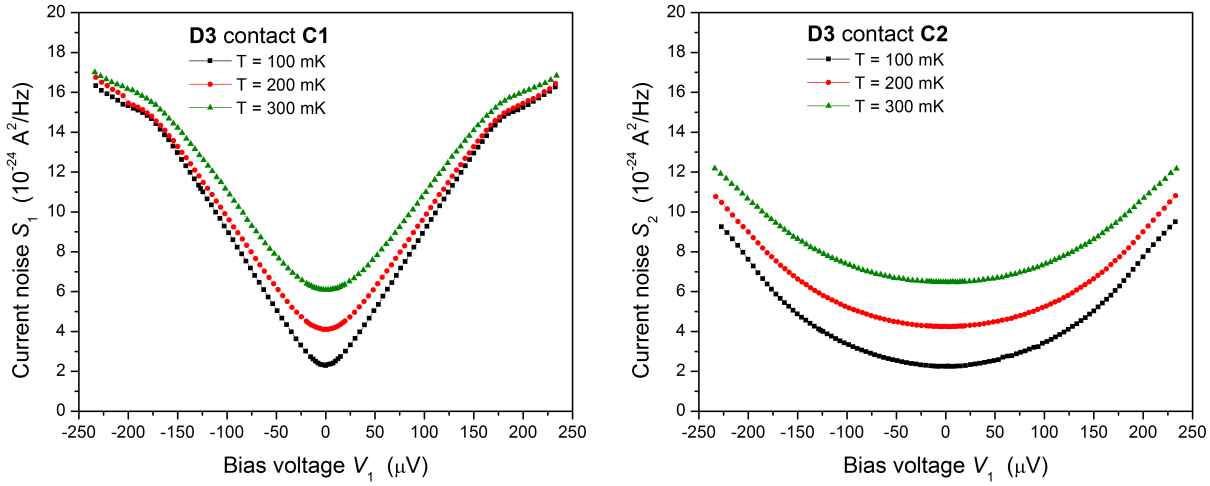

Figure 5.17: Current noise at injector **C1** and detector contact **C2**: A large amount of nonlocal current noise is observed at the detector when the injector contact is biased.

Heat transport in proximity structures was studied by Bezuglyi and Vinokur [139]. They assess that thermal transport across a short superconducting region of width $w \ll \xi_S$ is determined by the spectral thermal conductance of the adjacent proximity regions in the normal metal leads of the NSN structure. The spectral thermal conductance across the NSN structure is related to an average of the generalized diffusion constant $\mathcal{D}_L$ over the length of the proximity regions in the N wires in the same way as the spectral conductance $\mathcal{D}(E)$ represents an average of the generalized charge diffusion coefficient $\mathcal{D}_T$ along a diffusive wire, see Chapter 2. Assuming the approximations of their calculation are still valid for $w \sim \xi_S$, we obtain an order of magnitude estimate of the thermal conductance κ in our devices,

$$\kappa \sim \kappa_N \frac{k_\mathrm{B}T}{\Delta} \frac{L_T}{\xi_S} \sqrt{r} \approx 0.1 \kappa_N,$$

where κ_N is the normal state thermal conductance of the superconductor, $L_T = \sqrt{\frac{\hbar D_N}{2\pi k_\mathrm{B} T}}$ is the thermal length in the normal metal wire and r is the ratio of the diffusion constants in normal metal and superconductor. The estimate suggests that a significant fraction of the heat which is generated in the injector contact may cross the superconducting wire and flow into the detector contact. However, this should also decrease the Fano factor of the injector contact below 2/3 which we do not observe. At present, we cannot reconcile the apparent contradiction.

An indication for a more complicated relationship between heat flow and nonlocal current noise is given in Fig. 5.18. Here we quantify the nonlocal current noise by the voltage V_2^* which is defined as voltage value at which the shot noise in the detector were to equal the observed noise in the nonlocal configuration. We may disregard the divergence at low bias as an artifact of the interpolation method and find that the quantity V_2^* scales linearly with the bias voltage V_1 at the injector contact in the low bias region. Therefore, it would appear that the nonlocal noise behaves like shot noise for an effective applied voltage V_2^*, which is a fraction of the bias voltage at the injector contact.

Nonlocal current correlations – temperature dependence

In the calculations by Golubev and Zaikin [95] the nonlocal current correlations in an unbiased NSN device were predicted to scale linearly with temperature

$$S_{12}(0) = -4 k_\mathrm{B} T G_{12}(0).$$

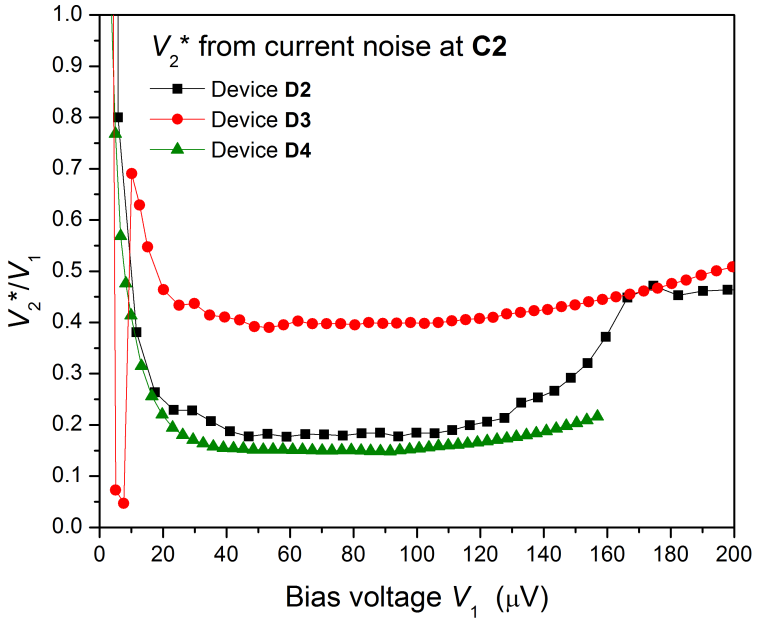

Figure 5.18: The quantity V_2^* is plotted as function of bias voltage for devices **C2** – **D4**. For a definition of V_2^*, see above.

Nonlocal current correlation data for devices **D1 - D4** are plotted as a function of temperature in Fig. 5.19. The cross spectral density S_{12} is normalized by the magnitude of the zero-bias cross conductance G_{12}, which can be calculated by inverting the resistance matrix. It is given by

$$G_{12} = -\frac{R_{NL}}{R_1 R_2 - R_{NL}^2}. \tag{5.5}$$

For the inversion we assumed symmetric off-diagonal (nonlocal resistance) elements, R_{NL}. Unlike Golubev and Zaikin, we define the cross-conductance as signed quantity here. Therefore, we divide by the absolute value. Despite the nonlinear temperature dependence of R_{NL} (see Fig. 5.20) and of the contact resistances R_1 and R_2, we find a linear temperature dependence of the normalized cross spectral density at the lowest temperatures.

Devices **D1** and **D4**, both with larger contact separation ($d \geq \xi_S$), show a proportionality factor of approximately -4, which is expected from theory. In the other two devices we find values smaller in magnitude. The current correlations in device **D2** scale with a proportionality factor of roughly -2.6, and for device **D3** the factor is -3.3. The reasons for the discrepancies are unclear.

Nonlocal current correlations – bias dependence

For an evaluation of the bias dependence of current correlations we need to invert the resistance matrix for arbitrary bias voltages at both contacts. In a bias sweep, however, we measure the dynamic resistance only for one of the contacts directly. We must approximate the dynamic resistance of the second contact from its $R-V$ characteristic for zero current bias at the first contact. The procedure is justified by experimental observations that the dynamic resistance of individual contacts is not affected by the current bias on the other contact up to large bias values. This is exemplified by data of an experiment on device **D3**. The resistance of **C2** is plotted for different current bias at **C1** in Fig. 5.21 and no significant differences in the resistance are observed up to high bias voltages at **C1**.

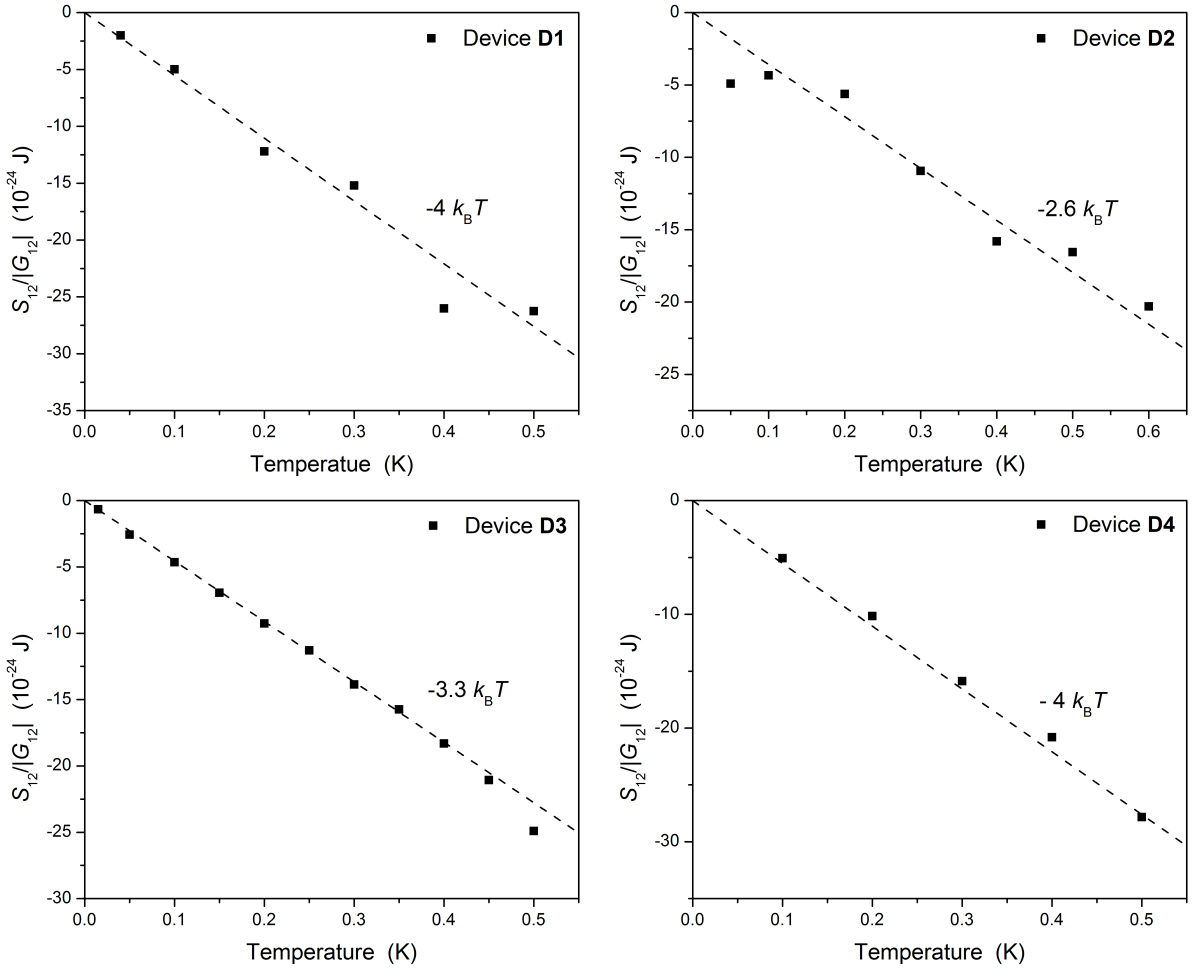

Figure 5.19: Temperature dependence of the normalized cross spectral density, $S_{12}/|G_{12}|$: A linear temperature dependence is observed at low temperatures. The proportionality factor differs clearly from the theoretically predicted value of -4 for **D2** and **D3**.

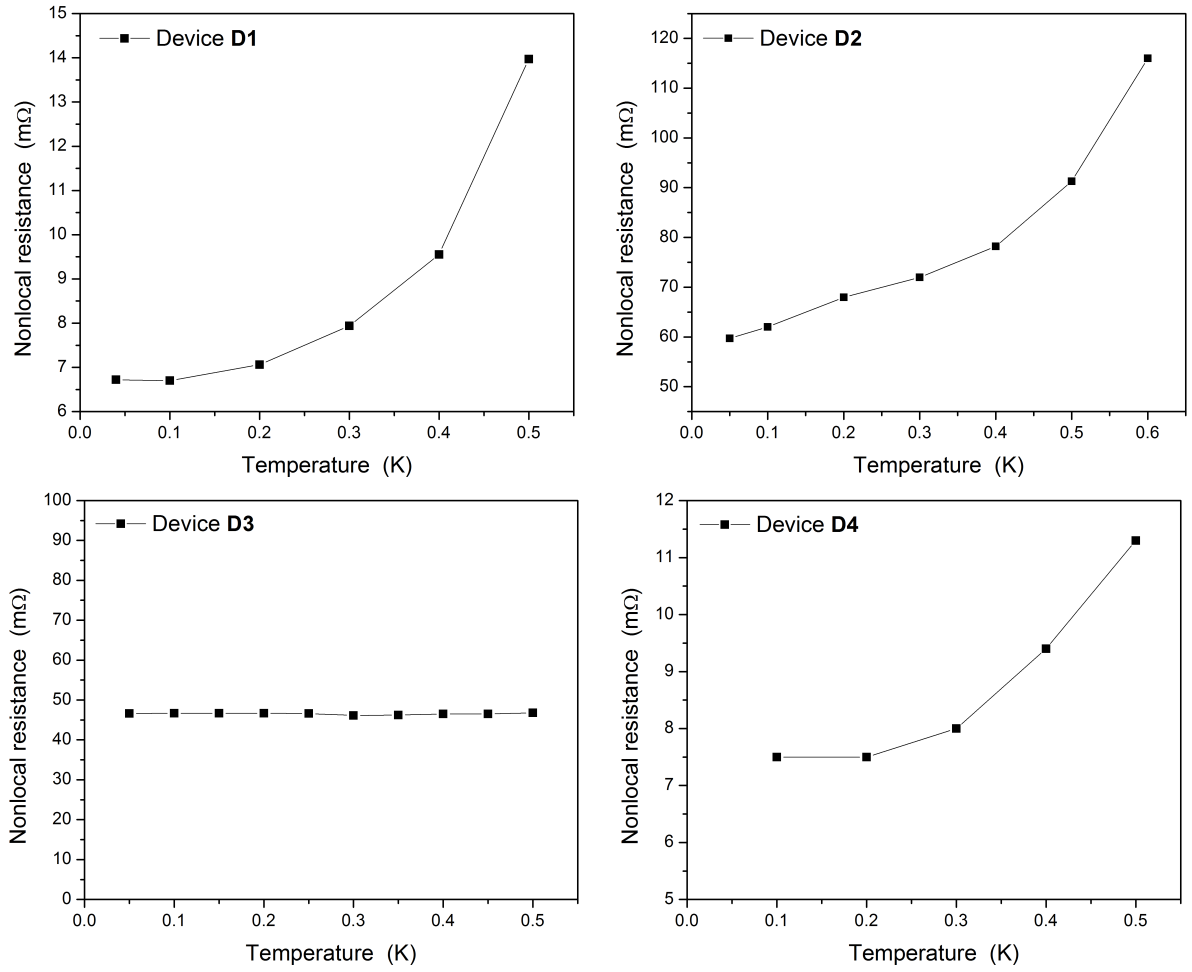

Figure 5.20: Temperature dependence of the zero-bias nonlocal resistance, R_{NL} for devices **D1-D4**. The zero-bias nonlocal resistance increases steeply with temperature except for device **D3**. This device has the closest contact spacing, $d \approx \xi_S/2$, and exhibits a flat dependence up to a temperature $T = 500$ mK.

The cross spectral density of device **D3** is plotted as a function of bias voltage at **C1** in Fig. 5.22. At a measurement temperature of $T = 100$ mK the bias dependence changes from a 'V'-shape for zero current bias at **C2** to a 'pyramid'-shape at 40 μA bias. A similar result is obtained when the roles of contacts **C1** and **C2** are reversed (not shown). At $T = 300$ mK the curves are offset and significantly broader. This is expected a crossover between thermal noise and shot noise correlations at higher temperatures.

We observe a progression from a 'V'-shaped bias dependence for zero current bias at **C2** to a 'W'-shape at higher bias in both devices. In Figs. 5.23 and 5.24 I plotted the normalized cross spectral density data for experiments at temperature $T = 100$ mK. Different current bias is applied at **C2** and the current noise correlations are recorded as the bias on **C1** is swept. In both devices a 'pyramid'-shaped peaks appears at $V_1 = 0$ as the current bias on **C2** is increased. The base of the feature extends between voltages $V_1 = \pm V_2$.

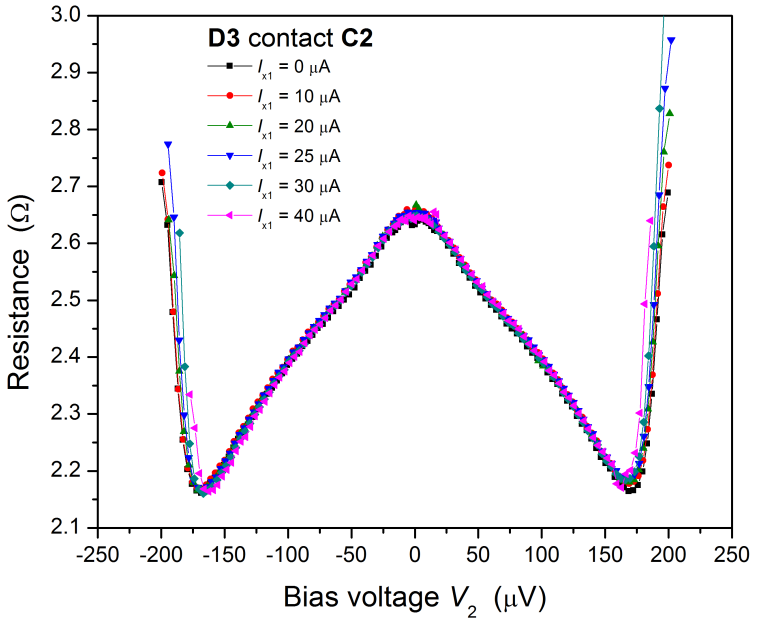

Figure 5.21: The resistance of **C2** for different current bias at **C1** in device **D3**: No significant difference in the resistance of **C2** is observed up to high bias values at contact **C1**.

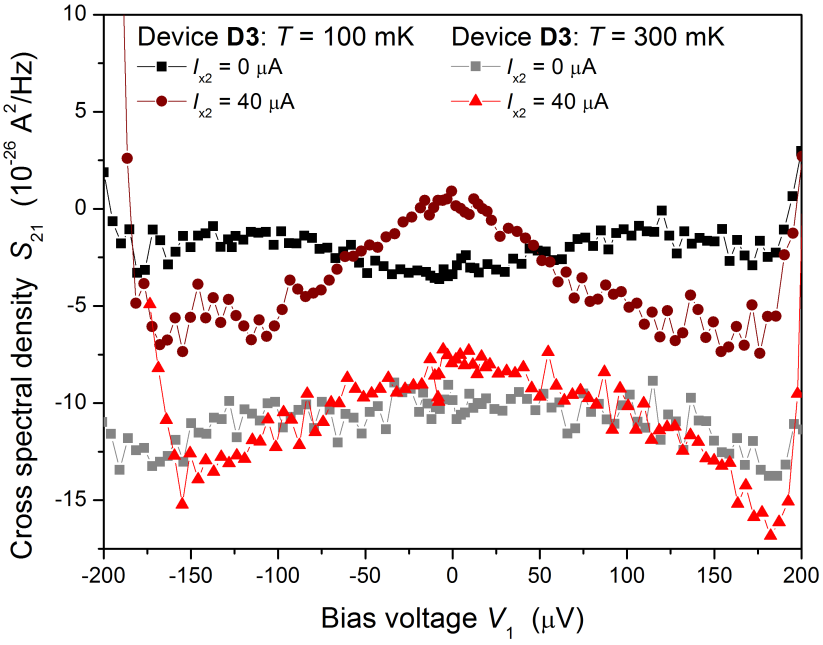

Figure 5.22: Cross spectral density of device **D3** at measurement temperatures T = 100 mK and T = 300 mK: The cross spectral density is graphed as a function of bias voltage at **C1** for an unbiased contact **C2** and for a current bias of 40 μA.

The voltage V_2 is set by the current bias at **C2** and is (approximately) constant over the whole bias sweep. The current correlations are mostly negative for device **D3** and approximately symmetric with respect to zero in device **D4**. The shapes of the current correlation curves of both devices bear striking resemblance to the theoretical predictions for NSN devices in the regime of intermediate interface transparencies which we examined in Chapter 3.

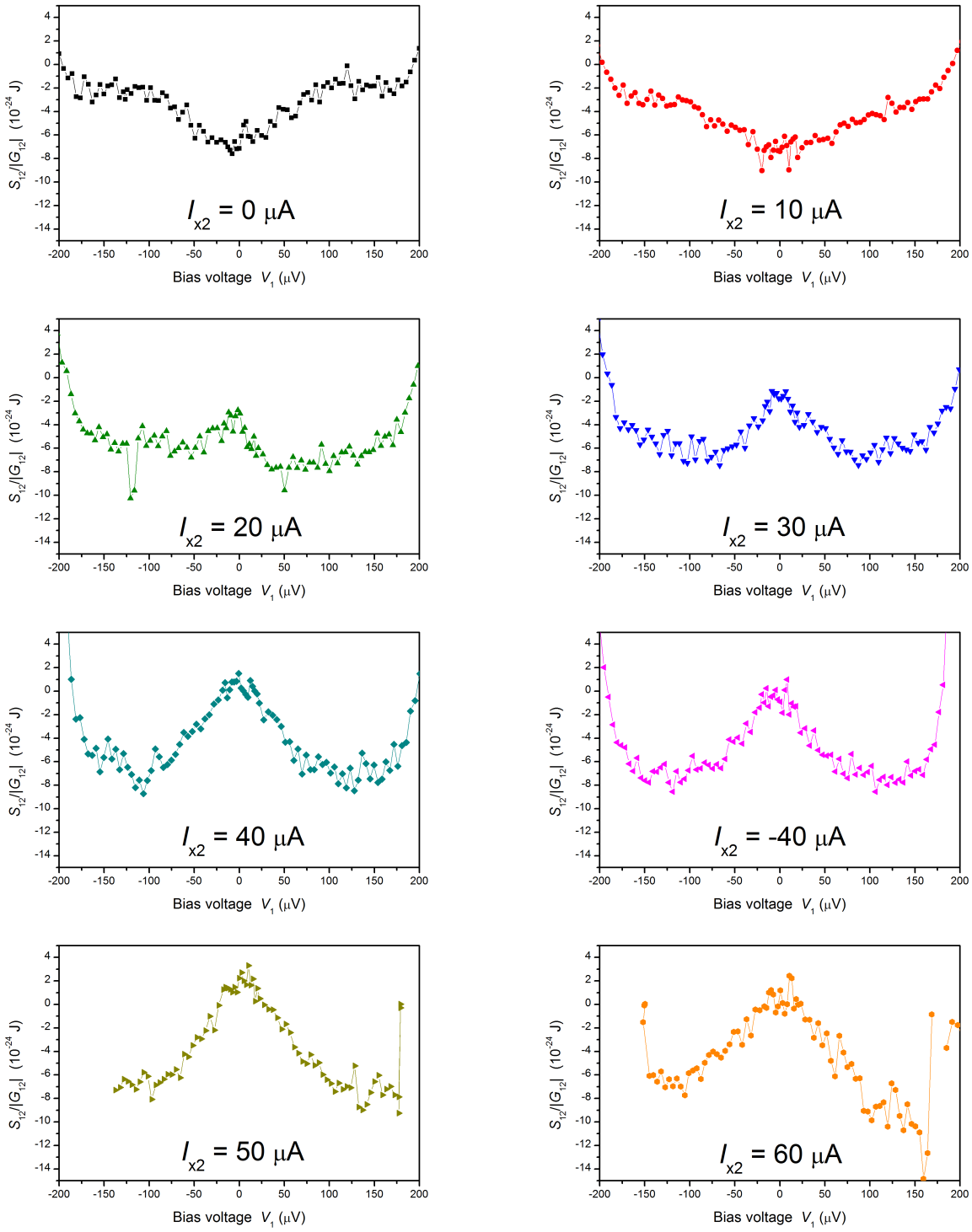

Figure 5.23: Normalized cross spectral density $S_{12}/|G_{12}|$ of **D3** as function of bias voltage at **C1** for different current bias at **C2**.

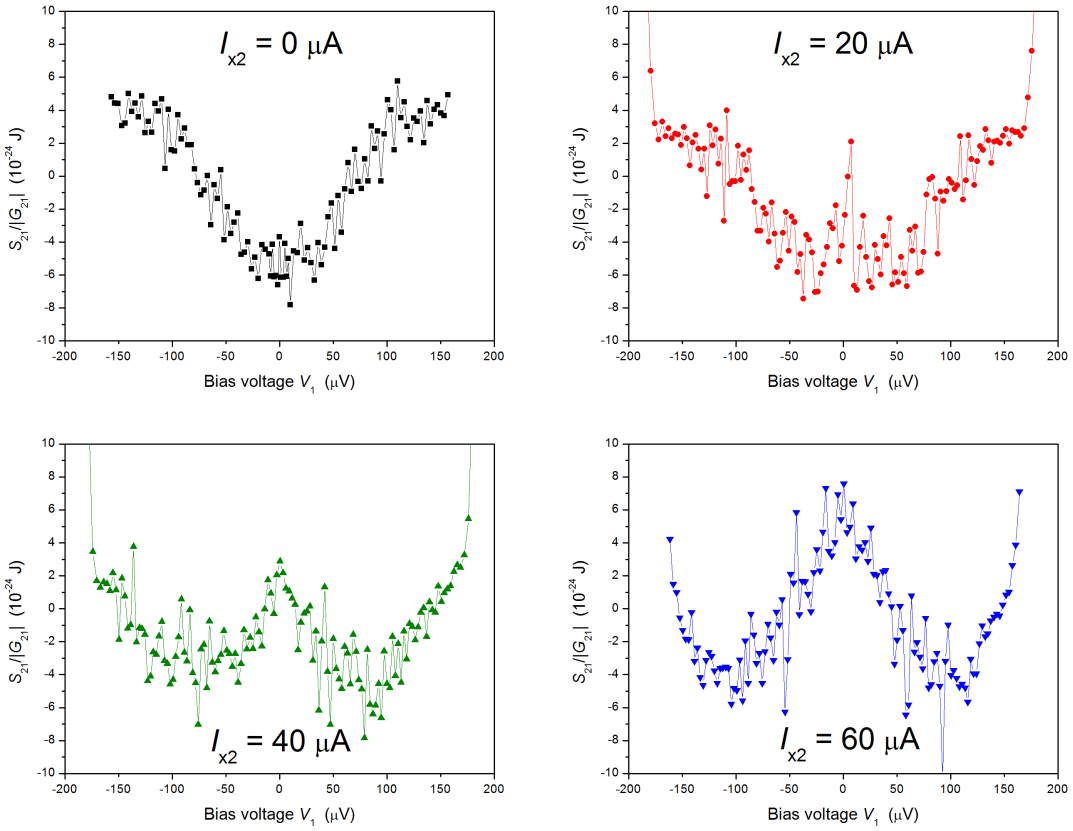

Figure 5.24: Normalized cross spectral density $S_{12}/|G_{12}|$ of **D4** as function of bias voltage at **C1** for different current bias at **C2**.

5.4 Discussion

The current correlation measurements in Figs. 5.24 and 5.24 and the temperature dependence of current correlations in Fig. 5.20 are the central results of this study. The data exhibits several important features which are expected for nonlocal shot noise correlations in NSN devices:

Firstly, zero-bias current correlations are negative. The signal scales linearly with cross conductance and temperature. This should apply irrespectively whether the normal metal contacts are reservoirs or diffusive wires. The quasiparticle distribution in equilibrium is the same in both cases. In two of the devices **D1** and **D4** the temperature dependence scales with the expected proportionality factor. In the other two devices we find a smaller value. The reason for the discrepancy is not clear. We may speculate that it is related to the enhancement of the zero-bias conductance in device **D2**. In device **D3** an increased resistance in the

interface region was observed. This may also affect the nonlocal transport.

Secondly, for an unbiased second contact, $I_{x2} = 0$, the current correlations increase with applied bias V_1 (for both polarities). The same behavior is observed when the roles of two contacts are reversed (graph not shown but may be inferred from Figs. 5.24 and 5.24). We may therefore rule out nonequilibrium quasiparticles as source of the signal at low bias as quasiparticles are expected to cause negative, fermionic correlations. This statement is corroborated by two other facts. Following our analysis of the shot noise data of devices **D1** and **D2** a substantial nonequilibrium quasiparticle current is expected to set in above a critical voltage value related to the order parameter in the contact region. This value is approximately 110 μV in devices **D3** and **D4**. A characteristic drop in the Fano factors of contacts **C1** are observed at this voltage indicating the onset of quasiparticle transport. The nonlocal resistance is (almost) constant up to this voltage which also suggests that nonequilibrium quasiparticle transport is negligible.

The fact that we obtain a similar behavior for the current correlation signal when we reverse the roles of contacts **C1** and **C2** is somewhat surprising as the shapes of the dynamic resistance curves are different. As we suggested earlier the effect may come from a local suppression of the order parameter in the contact region and parts of the superconducting wire along the diffusion path of quasiparticles. The dimensions of the superconducting wire are chosen large enough such that the second contact should not be affected. This claim is supported by the fact that the nonlocal resistance does not show signs of charge imbalance below 110 μV.

Thirdly, when the second contact is biased, $I_{x2} \neq 0$, a 'pyramid'-like feature appears around zero bias. The base of this feature extends between $V_1 = \pm V_2$. This peculiar bias dependence can be understood when 'CAR-like' and 'EC-like' nonlocal transport processes contribute to current correlations with probabilities of similar magnitude. In theoretical models of NSN devices with normal metal reservoirs this happens for intermediate barrier transparencies. The probability for an individual process depends on either electron or hole quasiparticle population in each of the electrodes, and therefore a symmetric bias dependence may be observed when the interface transparencies are of similar magnitude. Contact geometry and the resulting interference effects may also play a role in determining the relative strength of nonlocal processes. These are not accounted for in the BTK-model of Mélin et al. [106] and the work by Golubev and Zaikin [95].

The transmissions of the contacts are limited by the interface transparencies. Our numerical results for the contact resistances indicate barrier strengths of $Z \approx 0.4$ at the interfaces of our contacts which is equivalent

to a contact transparency of $T \approx 0.86$. In this regime a crossover to negative correlations is predicted. Our data suggests the devices are right at this crossover. We observe both, positive and negative correlations, as a function of voltage bias at the contacts.

A proper quantitative assessment of nonlocal current correlations must take the nonequilibrium quasiparticle distributions in the diffusive normal metal wires into consideration. Theoretical predictions for diffusive contacts do not yet exist. However, shape, sign, and order of magnitude of the nonlocal current correlations in our samples are in good qualitative agreement with available theoretical predictions for NSN devices with normal metal reservoirs and similar interface transparencies. We may therefore interpret our results as direct observation of coherent higher-order nonlocal transport.

We will discuss implications of our results for the implementation of Cooper-pair splitter devices in the next chapter. We will also suggest future directions of study.

Chapter 6

Conclusions and future directions

We studied transport, shot noise, and current correlations in mesoscopic normal metal-superconductor hybrid (NSN) devices and found evidence for coherent higher-order nonlocal transport in superconductors at subgap energies. The work was motivated by theoretical results which claimed positive nonlocal current correlations in NSN devices with high interface transparency. Such correlations are not believed to be cause by the splitting of Cooper pairs but by synchronized Andreev reflection events at the individual interfaces of the NSN device.

In a first experiment we measured nonlocal resistance as a function of contact separation between normal metal electrodes attached to a superconducting wire. We confirmed earlier findings by Cadden-Zimansky and Chandrasekhar [5] on the scaling of nonlocal voltage signals with the coherence length of the superconductor. We also found that order parameter suppression due to inverse proximity effect is not necessary to observe nonlocal transport. The decay length of the nonlocal transport signal is set by the effective pairing potential in the superconducting wire.

The main body of work consists of current noise measurements in mesoscopic NSN devices. We devised a model for current noise in mesoscopic NSN structures by introducing an effective energy scale for the onset of heat transport due to quasiparticles into the formula for incoherent shot noise by Nagaev and Büttiker. The effective energy scale is found to coincide with the suppressed order parameter in the contact region. The suppression is due to the inverse proximity effect that results from coupling normal metal electrodes to the superconductor. The data is well described by the model up to a critical voltage at which non-equilibrium effects become important in the contact region. Reservoir heating effects were observed in an earlier experiment and could also be accounted for in the model by introducing an effective temperature. Heating effects were not observed in subsequent experiments with improved device geometry.

The onset of nonequilibrium transport was also observed as a charge imbalance signal in nonlocal resistance measurements. Below the critical voltage the nonlocal resistance changed only slightly with applied bias

but a large increase was observed above the critical voltage. This finding was somewhat surprising to us as some of the contacts showed a resistance dependence which may be interpreted as local suppression of the order parameter. However, the dimensions of the superconducting wire were chosen large enough to prevent the diffusion of non-equilibrium quasiparticles into the other contact. This interpretation is consistent with nonlocal current noise and current correlation data.

Current correlation data were compared for two devices with contact spacing $\xi_S \approx \frac{1}{2}$ and $\xi_S \approx 1$, where ξ_S is the coherence length in the superconductor. Both devices were fabricated simultaneously and had matching materials and interface properties. Current correlations much larger than the predicted values for nonlocal Andreev reflection and elastic co-tunneling (i.e. the tunneling of an electron across the superconductor) were observed which suggests the contribution of higher-order nonlocal transport processes. Very large, positive current correlations, which are predicted for highly transparent interfaces, were not found in the experiments. Instead the devices exhibited regions of positive and negative current correlations with a symmetric bias dependence. This is in agreement with estimates for the interface transparencies of our contacts which are found to be in the intermediate regime. In this case contributions from 'CAR-like' and 'EC-like' higher-order processes are expected to be of similar magnitude which results in the observed symmetry. Positive correlations are mainly caused by synchronized Andreev reflection events at the two NS interfaces of the device. Shape and magnitude of the current correlation data are in good qualitative agreement with theoretical predictions. We are thus the first to directly observe signatures of coherent higher-order nonlocal transport.

An understanding of higher-order nonlocal transport may prove essential for the implementation of entanglement devices which intend to maximize the efficiency of Cooper-pair splitting. The relative contributions of nonlocal transport processes may be tuned by creating nonequilibrium quasiparticle distributions in the two branches of the Cooper-pair splitter. This may be achieved electrically or by photon-assisted manipulation of the quasiparticle distributions in a waveguide. Many open questions remain regarding nonequilibrium effects in the mesoscopic superconducting wires of our devices. To address these questions we may envision an experiment where current correlations are probed between several pairs of normal metal contacts which are attached along a superconducting wire into which current is injected from a normal metal reservoir. In this way the noise signal due to non-equilibrium distributions in the superconducting wire may be probed.

Appendix A

Keldysh-Usadel equations for a NS contact with interface barrier

The appendix lists the equations for calculating the resistance of a diffusive wire - superconductor contact with interface barrier. The equations are adapted from Tanaka et al. [28].

The retarded Green's function in the superconductor is parametrized by

$$\hat{G}_S^R = g\tau_3 + f\tau_2, \quad \text{with } g = \frac{E}{\sqrt{E^2-\Delta^2}}, \quad \text{and } f = \frac{\Delta}{\sqrt{\Delta^2-E^2}}. \tag{A.1}$$

The spectral equation in $\hat{G}^R = \tau_3\cos\theta + \tau_2\sin\theta$ parametrization is given by ($\hbar \equiv 1$)

$$D\partial_x^2\theta + 2i(E + i\Gamma_{in})\sin\theta - \Gamma_{sf}\sin 2\theta = 0, \tag{A.2}$$

where Γ_{in} and Γ_{sf} are used to introduce weak inelastic scattering and spin-flip scattering. A small but finite value for Γ_{in} is used to preserve the analytic structure of the Green's functions in the numerical calculations. The boundary condition for the spectral equation is

$$L\partial_x\theta(x)|_{x=0_+} = \frac{R_d}{R_b}\langle F\rangle, \tag{A.3}$$

$$F = \frac{2T_m(f\cos\theta_0 - g\sin\theta_0)}{(2-T_m) + T_m(g\cos\theta_0 + f\cos\theta_0)}, \tag{A.4}$$

with $\theta_0 = \theta(0_+)$. The transmission coefficients T_m are given in section 2.2.5 and the averaging is carried out over all angles of particle injection (see also section 2.2.5).

The Keldysh component of the equations reads

$$D\partial_x\left[(\partial_x f_T)\cosh^2(\text{Im }\theta)\right] = 0, \tag{A.5}$$

with the boundary condition

$$L(\partial_x f_T)\cosh^2(\mathrm{Im}\ \theta)\big|_{x=0_+} = -\frac{R_d}{R_b}\langle I_{b0}\rangle f_T(0_+), \tag{A.6}$$

and

$$\begin{aligned} I_{b0} &= \frac{T_m^2\Lambda_1 + 2T_m(2-T_m)\Lambda_2}{2|(2-T_m)+T_m[g\cos\theta_0 + f\sin\theta_0]|^2}, & \text{(A.7)}\\ \Lambda_1 &= (1+|\cos\theta_0|^2+|\sin\theta_0|^2)(|g|^2+|f|^2+1) + 4\mathrm{Im}\ [fg^*]\mathrm{Im}\ [\cos\theta_0\sin\theta_0^*], & \text{(A.8)}\\ \Lambda_2 &= \mathrm{Re}\ [g(\cos\theta_0+\cos\theta_0^*) + f(\sin\theta_0+\sin\theta_0^*]. & \text{(A.9)} \end{aligned}$$

Both reservoirs are kept at temperature T. The superconductor is always at zero voltage and the normal metal reservoir is biased at voltage V. Thus the distribution $F_{TL}(E,V) = F_T(L,E)$ in the normal reservoir is

$$f_{TL}(E,V) = \frac{1}{2}\left[\tanh\left(\frac{E+eV}{2k_\mathrm{B}T}\right) - \tanh\left(\frac{E-eV}{2k_\mathrm{B}T}\right)\right].$$

Finally, the current is given by

$$I(V) = \frac{L}{R_d}\int_0^\infty \mathrm{d}E\ \cosh^2(\mathrm{Im}\ \theta)\ (\partial_x f_T)|_{x=0+} = \int_0^\infty \mathrm{d}E \frac{f_{TL}(E,V)}{\frac{R_b}{\langle I_{b0}\rangle} + \frac{R_d}{L}\int_0^L \frac{\mathrm{d}x}{\cosh^2(\mathrm{Im}\ \theta)}}. \tag{A.10}$$

References

[1] L.N. Cooper, Phys. Rev., Vol. 104, p. 1189, 1956.

[2] J. Bardeen, L.N. Cooper, and J.R. Schrieffer, Phys. Rev., Vol. 106, p. 162, 1957.

[3] J. Bardeen, L.N. Cooper, and J.R. Schrieffer, Phys. Rev., Vol. 108, p. 1175, 1957.

[4] M.P. Marder, *Condensed Matter Physics*, John Wiley & Sons, New York, 2000.

[5] P. Cadden-Zimansky and V. Chandrasekhar, Phys. Rev. Lett., Vol. 97, No. 23, pp. 237003(4), 2006

[6] D. Beckmann, H.B. Weber, and H.v. Löhneysen, Phys. Rev. Lett., Vol. 93, No. 19, pp. 197003(4), 2004

[7] N.N. Bogoliubov, Nuovo Cimento, Vol. 7, p. 794, 1958; J.G. Valatin, *ibidem*, p. 843.

[8] J. Clarke, Phys. Rev. Lett., Vol. 28, p. 1363, 1972.

[9] M.L. Yu, and J.E. Mercereau, Phys. Rev., Vol. B21, p. 4909, 1979.

[10] C.C. Chi, and J. Clarke, Phys. Rev. B, Vol. 19, 4495, 1979.

[11] T.Y. Hsiang, and J. Clarke, Phys. Rev. B, Vol. 21, p. 945, 1980.

[12] D.J. Van Harlingen, J. Low Temp. Phys., Vol. 44, p. 163, 1981.

[13] T.R. Lemberger, and J. Clarke, Phys. Rev. B, Vol. 23, 1088, 1981.

[14] H.J. Mamin, J. Clarke, and D.J. Van Harlingen, Phys. Rev. B, Vol. 29, 3881, 1984.

[15] A. Schmid, and G. Schön, J. Low Temp. Phys., Vol. 20, p. 207, 1975.

[16] C.J. Pethick, and H. Smith, Ann. Phys. (N.Y.), Vol. 119, p. 133, 1979.

[17] P.G. de Gennes, *Superconductivity of Metals and Alloys*, Addison-Wesley, 1989.

[18] N.N. Bogoliubov, V.V. Tolmachev, D.V. Shirkov, *A New Method in the Theory of Superconductivity*, Consultant Bureau, New York, 1959.

[19] A.F. Andreev, Sov. Phys. JETP, Vol. 19, p. 1228, 1964.

[20] A. Kleine, A. Baumgartner, J. Trbovic, D.S. Golubev, A.D. Zaikin, C. Schönenberger, Nanotechnology, Vol. 21, p. 274002, 2010.

[21] G.E. Blonder, M. Tinkham, and T.M. Klapwijk, Phys. Rev. B, Vol. 25, p. 4515, 1982.

[22] Supriyo Datta, *Electron Transport in Mesoscopic Systems*, Cambridge studies in semiconductor physics and microelectronic engineering, Cambridge University Press, Cambridge, U.K., 1995.

[23] A.A. Abrikosov, L.P. Gorkov, and I.E. Dzyaloshinski, *Methods of Quantum Field Theory in Statistical Physics*, Dover, New York, 1963.

[24] W. Belzig, F.K. Wilhelm, Ch. Bruder, G. Schön, and A.D. Zaikin, *Quasiclassical Green's function approach to mesoscopic superconductivity*, Superlattices and Microstructures, Vol. 25, No. 5/6, pp. 1251-1288, 1999

[25] V. Chandrasekhar, *An introduction to the quasi-classical theory of superconductivity for diffusive proximity-coupled systems*, in "The Physics of Superconductors", Vol II, edited by Bennemann and Ketterson, Springer-Verlag, 2004.

[26] P. Virtanen, T.T. Heikkilä, Appl. Phys. A, Vol. 89, pp. 625-637, 2007.

[27] M.G. Flokstra, *Proximity effects in superconducting spin-valve structures*, PhD dissertation, Leiden, 2010.

[28] Y. Tanaka, A.A. Golubov, and S. Kashiwaya, Phys. Rev. B, Vol. 68, p. 054513, 2003.

[29] A.F. Volkov, A.V. Zaitev, and T.M. Klapwijk, Physica C, Vol. 210, pp. 21-34, 1993.

[30] H. Courtois, Ph. Gandit, B. Pannetier, D. Mailly, Superlattices and Microstructures, Vol. 25, No. 5/6, 1999

[31] A Python-wrapped solver by Pauli Virtanen for boundary value problems based on the collocation method. It is uses the Fortran code `COLNEW` from `www.netlib.org` and is available for download as a scikits-package from `http://www.iki.fi/pav/software/bvp`.

[32] Yu.V. Nazarov, Superlattices and Microstructures, Vol. 25, No. 56, pp. 1221-1231, 1999.

[33] The source code is available at `http://ltl.tkk.fi/ theory/usadel1/`.

[34] P.G. de Gennes, Rev. Mod. Phys., Vol. 36, p. 225, 1964.

[35] N. Wiener, Acta Mathematica, Vol. 55, p. 117, 1930; A. Khintchine, Math. Ann., Vol. 109, No. 4, p. 604, 1934.

[36] Ya.M. Blanter, M. Büttiker, Physics Reports, Vol. 336, pp. 1-166, 2000.

[37] A.D. Stone, P.A. Mello, K.A. Muttalib, and J.-L. Pichard, in *Mesoscopic Phenomena in Solids*, edited by B.L. Al'tshuler, P.A. Lee, and R.A. Webb, North-Holland, Amsterdam, 1991.

[38] C.W.J. Beenakker, M. Büttiker, Phys. Rev. B, Vol. 46, p. 4695, 1992.

[39] C.W.J. Beenakker, Rev. Mod. Phys., Vol. 69, p. 731, 1997.

[40] K.E. Nagaev, Phys. Lett. A, Vol. 169, p. 103, 1992.

[41] B.L. Altshuler, L.S. Levitov, A.Yu. Yakovets, JETP Lett., Vol. 59, p. 857, 1994.

[42] Yu. V. Nazarov, Phys. Rev. Lett., Vol. 73, p. 134, 1994.

[43] Ya.M. Blanter, M. Büttiker, Phys. Rev. B, Vol. 56, p. 2127, 1997.

[44] E.V. Sukhorukov, D. Loss, Phys. Rev. Lett., Vol. 80, No. 22, p. 4959, 1998.

[45] F. Liefrienk, J.I. Dijkhuis, M.J.M. de Jong, L.W. Molenkamp, H. van Houten, Phys. Rev. B, Vol. 49, p. 14066, 1994.

[46] A.H. Steinbach, J.M. Martinis, and M.H. Devoret, Phys. Rev. Lett., Vol. 76, No. 20, pp. 3806-3809, May 1996

[47] M. Henny, S. Oberholzer, C. Strunk, and C. Schönenberger, Phys. Rev. B, Vol. 59, No. 4, pp. 2871-2880, 1999.

[48] M.J.M. de Jong, C.W.J. Beenakker, Phys. Rev. B, Vol. 49, p. 16070, 1994.

[49] T. Martin, *Noise in Mesoscopic Physics*, les Houches Session LXXXI, H. Bouchiat et. al. eds., Elsevier, 2005.

[50] K.E. Nagaev, M. Büttiker, Phys. Rev. B, Vol. 63, No. 8, p. 081301(R), 2001.

[51] M. Houzet, V.P. Mineev, Phys. Rev. B, Vol. 67, No. 18, p. 184524, 2003.

[52] M.J.M. de Jong, C.W.J. Beenakker, Physica A, Vol. 230, pp. 290-248, 1996.

[53] X. Jehl, M. Sanquer, R. Calemczuk and D. Mailly, Nature, Vol. 405, p. 50, 2000.

[54] A.A. Kozhevnikov, R.J. Schoelkopf, and D.E. Prober, Phys. Rev. Lett., Vol. 84, No. 15, p. 3398, 2000.

[55] B. Reulet, A.A. Kozhevnikov, D.E. Prober, W. Belzig, and Yu.V. Nazarov, Phys. Rev. Lett., Vol. 90, No. 6, p. 066601, 2003.

[56] X. Jehl, M. Sanquer, Phys. Rev. B, Vol. 63, p. 052511, 2001.

[57] W. Belzig, and Yu.V. Nazarov, Phys. Rev. Lett., Vol. 87, No. 6, p. 067006, 2001.

[58] L.S. Levitov, H.W. Lee, and G.B. Lesovik, J. Math. Phys., Vol. 37, p. 10, 1996.

[59] M. Houzet, and F. Pistolesi, Phys. Rev. Lett., Vol. 92, No. 10, p. 107004, 12 March 2004.

[60] Ya.M. Blanter, M. Büttiker, Physics Reports, Vol. 336, pp. 1-166, 2000.

[61] M. Henny, PhD dissertation, Universität Basel 1998.

[62] X. Jehl, P. Payet-Burin, C. Baraduc, R. Calemczuk, and M. Sanquer, Rev. Sci. Instr., Vol. 70, No. 6, pp. 2711-2714, June 1999

[63] B. Kaviraj, O. Coupiac, H. Courtois, F. Lefloch, Phys. Rev. Lett., Vol. 107, No. 7, pp. 077005-077009, August 2011.

[64] B.-R. Choi, *et al.*, Phys. Rev. B, Vol. 72, pp. 024501-024511, 2005

[65] J.M. Byers, and M.E. Flatté, Phys. Rev. Lett., Vol. 74, No. 2, pp. 306-309, 1995.

[66] G. Deutscher, and D. Feinberg, Appl. Phys. Lett., Vol. 76, p. 487, 2000.

[67] G. Deutscher, J. Supercond., Vol. 15, No. 1, p. 43, 2002.

[68] L. Hofstetter, et al., Nature, Vol. 461, p. 960, Oct. 2009.

[69] L. Hofstetter, et al. Phys. Rev. Lett., Vol. 107, p. 136801, 2011.

[70] S. De Franceschi, L. Kouwenhoven, Ch. Schönenberger, and W. Wernsdorfer, Nature Nanotechnology, Vol. 5, p. 703, Oct. 2010.

[71] J. Brauer et al., Phys. Rev. B, Vol. 81, p. 024519, 2011.

[72] M.-S. Choi, C. Bruder, and G. Blatter, Phys. Rev. B, Vol. 62, No. 20, p. 13569, 2000.

[73] G.B. Lesovik, Th. Martin, and G. Blatter, Eur. Phys. J. B, Vol. 24, p. 287, 2001.

[74] C. Bena, S. Vishveshwara, L. Balents, and M.P.A. Fisher, Phys. Rev. Lett., Vol. 89, No. 3, p. 037901, 2002.

[75] V. Bouchiat et al., Nanotechnology, Vol. 14, pp. 77-85, 2003.

[76] P. Recher, D.S. Saraga, and D. Loss, in NATO Science Series II, *Fundamental Problems of Mesoscopic Physics, Interaction and Decoherence*, Vol. 154, eds. I.V. Lerner et al., pp. 179-202, Kluwer, Dortrecht, 2004.

[77] J. Torrés, and Th. Martin, Eur. Phys. J. B, Vol. 12, p. 319-322, 1999.

[78] P. Samuelsson, and M. Büttiker, Phys. Rev. Lett., Vol. 89, No. 4, p. 046601, 2002.

[79] J.C. Egues et al., in NATO Science Series, *Quantum Noise in Mesoscopic Physics*, Vol. 97, pp. 241-274, Kluwer, Dortrecht, 2003.

[80] M. Henny et al., Science, Vol. 284, pp. 284-286, April 1999; and W.D. Olivier, et al., *ibid.*, pp. 299-301

[81] Jian Wei, and V. Chandrasekhar, Nature Physics, Vol. 6, p. 494, July 2010.

[82] G. Falci, D. Feinberg, and F.W.J. Hekking, Europhys. Lett., Vol. 54, No. 2, pp. 255-261, 2001.

[83] D. Feinberg, Eur. Phys. J. B, Vol. 36, pp. 419-422, 2003.

[84] R. Mélin, and D. Feinberg, Euro. Phys. J. B, Vol. 26, pp. 101-114, 2002.

[85] F. Taddei, and R. Fazio, Phys. Rev. B, Vol. 65, p. 134522, 2002.

[86] G. Bignon *et al.*, Europhys. Lett., Vol. 67, p. 110, 2004.

[87] S. Russo, M. Kroug, T.M. Klapwijk, and A.F. Morpurgo, Phys. Rev. Lett., Vol. 95, No.2, p. 027002, 2005.

[88] A. Kleine, A. Baumgartner, J. Trbovic, and C. Schönenberger, Euro. Phys. Lett., Vol. 87, p. 27011, 2009.

[89] A. Levy Yeyati, F.S. Bergeret, A. Martin-Rodero, and T.M. Klapwijk, Nat. Phys, Vol. 3, p. 455, 2003.

[90] F.J. Jedema, A.T. Filip, and B.J. van Wees, Nature, Vol. 410, p. 345, 2001.

[91] B.I. Ivlev, and N.B. Knopin, Adv. Phys., Vol. 33, p. 47, 1984.

[92] C.-J. Chien, and V. Chandrasekhar, Phys. Rev. B, Vol. 60, p. 3655, 1999.

[93] R. Mélin, D. Feinberg, Phys. Rev. B, Vol. 70, p. 174509, 2004.

[94] D.S. Golubev, M.S. Kalenkov, and A.D. Zaikin, Phys. Rev. Lett., Vol. 103, p. 067006, 2009.

[95] D.S. Golubev, and A.D. Zaikin, Phys. Rev. B, Vol. 82, p. 134508, 2010.

[96] F.S. Bergeret, and A. Levy Yeyati, Phys. Rev. B, Vol. 80, p. 174508, 2009.

[97] P. Cadden-Zimansky, J. Wei, and V. Chandrasekhar, Nature Physics, Vol. 5, p. 393, June 2009.

[98] P. Cadden-Zimansky, *Nonlocal Coherence in Normal Metal-Superconductor Nanostructures*, PhD dissertation, Northwestern University, Evanston, IL, 2008.

[99] D. Beckmann, H. v. Löhneysen, Appl. Phys. A, Vol. 89, pp. 603-607, 2007.

[100] A. Kastalsky, A.W. Kleinsasser, L.H. Greene, R. Bhat, F.P. Milliken, and J.P. Harbison, Phys. Rev. Lett., Vol. 67, p. 3025, 1991.

[101] B.J. van Wees, P. de Vries, P. Magnee, and T.M. Klapwijk, Phys. Rev. Lett., Vol. 69, p. 510, 1992.

[102] V. Apinyan, and R. Mélin, Eur. Phys. J. B, Vol. 25, pp. 373-389, 2002.

[103] R. Mélin, Phys. Rev. B, Vol. 73, p. 174512, 2006.

[104] M.S. Kalenkov, and A.D. Zaikin, Phys. Rev. B, Vol. 75, p. 172503, 2007; and Phys. Rev. B, Vol. 76, p. 224506, 2007.

[105] M.S. Kalenkov, and A.D. Zaikin, Phys. Rev. B, Vol. 82, p. 024522, 2010.

[106] R. Mélin, C. Benjamin, and T. Martin, Phys. Rev. B, Vol. 77, p. 094512, 2008.

[107] M. Flöser, A. Freyn, and R. Mélin, Phys. Rev. B, Vol. 82, p. 014510, 2010.

[108] F.C. Wellstood, C. Urbina, J. Clarke, Appl. Phys. Lett., Vol. 54, p. 2599, 1989.

[109] S. Rajauria, P.S. Luo, T. Fournier, F.W.J. Hekking, H. Courtois, and B. Pannetier, Phys. Rev. Lett., Vol. 99, No. 4, p. 047004, July 2007.

[110] L. DiCarlo, Y. Zhang, D.T. McClure, C.M. Marcus, L.N. Pfeiffer, K.W. West, Rev. Sci. Instr., Vol. 77, No. 7, p. 073906, 2006.

[111] D.C. Glattli, P. Jacques, A. Kumar, P. Pari, and L. Saminadayar, J. Appl. Phys., Vol. 81, p. 7350, 1997.

[112] Datasheet Stanford Research SR552 (source: `http://www.thinksrs.com/products/SR552.htm`).

[113] John Clarke, Alex Braginski (Eds.), *The SQUID Handbook: Vol. II Applications of SQUIDs and SQUID Systems*, Wiley-VCH Verlag GmbH & Co. KGaA, Weinheim 2006.

[114] John Clarke, Alex Braginski (Eds.), *Vol. I The SQUID Handbook: Fundamentals and Technology of SQUIDs and SQUID Systems*, Wiley-VCH Verlag GmbH & Co. KGaA, Weinheim 2004.

[115] Quantum Design, Inc., 6325 Lusk Boulevard, San Diego, CA 92112-3733, USA.

[116] STAR Cryoelectronics, 24-A Brisbee Court, Santa Fe, NM 87508-1412, USA.

[117] STAR Cryoelectronics SQ680 series documentation.

[118] H. Courtois, P. Charlat, Ph. Gandit, D. Mailly, and B. Pannetier, J. Low Temp. Phys., Vol. 116, No. 3/4, pp. 187-213, 1999.

[119] F.W.J. Hekking and Y. Nazarov, Phys. Rev. Lett., Vol. 71, p. 1625, 1993.

[120] W. Belzig, F.K. Wilhelm, Ch. Bruder, G. Schön, A.D. Zaikin, Superlattices and Microstructures, Vol. 25, No. 5/6, pp. 1251-1288, 1990.

[121] V.T. Petrashov, V.N. Antonov, P. Delsing, and T. Cleason, Phys. Rev. Lett., Vol. 70, p. 347, 1993.

[122] S.G. den Hartog, B.J. van Wees, T.M. Klapwijk, Yu.V. Nazarov, and G. Borghs, Phys. Rev. B, Vol. 56, p. 13738, 1997.

[123] V.T. Petrashov, V.N. Antonov, P. Delsing, and T. Cleason, Phys. Rev. Lett., Vol. 74, p. 5268, 1995.

[124] P. Charlat, H. Courtois, Ph. Gandit, D. Mailly, A.F. Volkov, and B. Pannetier, Phys. Rev. Lett., Vol. 77, p. 4950, 1996.

[125] H. Pothier, S. Gu'eron, D. Esteve, and M.H. Devoret, Phys. Rev. Lett., Vol. 73, No. 18, 1994

[126] S. Gu'eron, H. Pothier, N.O. Birge,D. Esteve, and M.H. Devoret, Phys. Rev. Lett., Vol. 77, No. 14, p. 3025, 1996.

[127] D. Est'eve, et al., in *Mesoscopic Electron Transport: NATO ASI series E*, Vol. 345, pp. 375-406 (eds. L.L. Sohn, et al., Kluwer Academic, Dordrecht/Boston/London, 1997).

[128] B.J. Van Wees, H. Takayanagi, in *Mesoscopic Electron transport: NATO ASI series E*, Vol. 345, pp. 469-502 (eds. L.L. Sohn, et al., Kluwer Academic, Dordrecht/Boston/London, 1997).

[129] B. Pannetier and H. J. Courtois, Low Temp. Phys., Vol. 118, p. 599, 2000.

[130] J.J.A. Baselmans, A.F. Morpurgo, B.J. van Wees, and T.M. Klapwijk, Nature, Vol. 397, Issue 6714, pp. 43-45, 1999.

[131] J. Huang et al., Phys. Rev. B, Vol. 66, p. 020507, 2002.

[132] H. Ibach, H. Lüth, *Festkörperphysik: Einführung in die Grundlagen*, Springer-Lehrbuch, 5. Auflage, 1999.

[133] B.L. Altshuler, A.G. Aronov, and D.E. Khmelnitskii, J. Phys. C, Vol. 15, p. 7367, 1982.

[134] N. Vercruyssen, T.G.A. Verhagen, M.G. Flokstra, J.P. Pekola, and T.M. Klapwijk, Phys. Rev. B, Vol. 85, p. 224503, 2012.

[135] Wolfram—Alpha knowledgebase, `http://www.wolframalpha.com/`, 2012

[136] F. Hübler, et al., Phys. Rev. B, Vol. 81, p. 164524, 2010.

[137] M.P. Anantram, and S. Datta, Phys. Rev. B, Vol. 53, No. 24, p. 16390, 1996.

[138] N. Poli, *Spin transport in normal and superconducting nanowires*, PhD dissertation, KTH Stockholm, Sweden, 2007.

[139] E.V. Bezuglyi, and V. Vinokur, Phys. Rev. Lett., Vol. 91, No. 13, p. 137002, 2003.